UCRL-9872
UC-34 Physics
TID-4500 (16th Ed.)

UNIVERSITY OF CALIFORNIA

Lawrence Radiation Laboratory
Berkeley, California

Contract No. W-7405-eng-48

NUCLEAR ALIGNMENT EXPERIMENTS ON CERIUM RADIOISOTOPES

James Norman Haag

(Ph. D. Thesis)

September 29, 1961

Printed in USA. Price $2.25. Available from the
Office of Technical Services
U. S. Department of Commerce
Washington 25, D.C.

DISCLAIMER

Strange, is it not? that of the myriads who
Before us pass'd the door of Darkness through,
No one returns to tell us of the Road,
Which to discover we must travel too.

Omar Khayyám

NUCLEAR ALIGNMENT EXPERIMENTS ON CERIUM RADIOISOTOPES

Contents

NUCLEAR ALIGNMENT EXPERIMENTS ON CERIUM RADIOISOTOPES

James Norman Haag

Department of Chemistry and Lawrence Radiation Laboratory
University of California, Berkeley, California

September 29, 1961

ABSTRACT

Nuclei of Ce^{137m}, Ce^{137}, Ce^{139}, Ce^{141}, and Ce^{143} were aligned in a neodymium ethylsulfate lattice at low temperatures by the magnetic hyperfine-structure method. The angular distribution and the plane polarization of the emitted gamma rays were measured as functions of temperature. The results are as follows.

For the spin sequence $11/2(Ce^{137m}) \xrightarrow[255\ kev]{M4} 3/2(Ce^{137})$, the magnetic moment of Ce^{137m} is $|\mu_N| = 0.96 \pm .09$ nm. The spin of Ce^{137m} is established as $11/2$.

For the spin sequence $3/2(Ce^{137}) \xrightarrow{i_{\beta}=0} 3/2 \xrightarrow[445\ kev]{M1, E2} 5/2$, the magnetic moment of Ce^{137} is $|\mu_N| = 0.95 \pm .20$ nm and $\delta\,(E2/M1) = -0.17 \pm .02$. The beta transition is established as predominantly $i_{\beta} = 0$.

For the spin sequence $3/2(Ce^{139}) \xrightarrow{i_{\beta}=1} 5/2 \xrightarrow[166\ kev]{M1, E2} 7/2(La^{139})$, the magnetic moment of Ce^{139} is $|\mu_N| = 0.95 \pm .20$ nm and $\delta(E2/M1) = +0.034 \pm .034$.

For the spin sequence $7/2(Ce^{141}) \xrightarrow{i_{\beta}=0} 7/2 \xrightarrow[142\ kev]{M1, E2} 5/2(Pr^{141})$, the magnetic moment of Ce^{141} is $|\mu_N| = 1.30 \pm .20$ nm and $\delta(E2/M1) = +0.066 \pm .022$. The spin of the 142-kev level of Pr^{141} is established as $7/2$. The β transition is established as predominantly $i_{\beta} = 0$.

For the spin sequence $7/2(Ce^{143}) \xrightarrow{i_\beta=0,1} 7/2 \xrightarrow[294\ kev]{M1, E2} 7/2$, the magnetic moment of Ce^{143} is $|\mu_N| = 1.00 \pm .30$ for a pure $i_\beta = 0$ transition and $|\mu_N| = 1.20 \pm .30$ for a pure $i_\beta = 1$ transition. In both cases, $\delta(E2/M1) = -0.80 \pm .20$.

Nuclei of Ce^{135} were also aligned. The presence of the 255-kev γ ray of Ce^{137m} together with the 265-kev γ ray from the decay of Ce^{135} prevented an interpretation of the results.

I. INTRODUCTION

The magnetic dipole moments of near-spherical nuclei deviate from the theoretical shell-model values.[1] In order to obtain additional systematic data on this phenomenon, the magnetic moments of five cerium nuclei were measured.

The atomic-beam technique of determining magnetic moments has to date proven unsuccessful for cerium.[2] Paramagnetic resonance methods have been used to determine only the magnetic moment[3] of Ce^{141}. However, by use of the low-temperature magnetic hyperfine-structure method of nuclear alignment, magnetic moments were determined for Ce^{137m}, Ce^{137}, Ce^{139}, Ce^{141}, and Ce^{143}. In addition, information was obtained on the angular momenta and the mixing ratios involved in the decay of these five isotopes. Finally, a measure of the validity of the nuclear alignment results for cerium was obtained by comparing the alignment result for the magnetic moment of Ce^{141} with the result determined from paramagnetic resonance.

The philosophy utilized in the presentation of this thesis was to proceed from the general to the particular. The author, feeling himself incapable of following the narrow verbal path between conciseness and obscurity, consciously chose the path of wordiness.

II. THEORY OF NUCLEAR ORIENTATION

A. General Comments

The term "nuclear orientation" denotes a system whose nuclear spins are oriented along one or several specific directions. Nuclear orientation exists when the thermodynamic condition

$$S < R \ln (2I + 1)$$

is satisfied.

In this inequality, S is the entropy of the nuclear spin system, I is the nuclear spin, and R is the gas constant. This inequality essentially states that when the spatial orientation of the nuclear spins in the system is not random, nuclear orientation exists.

The above inequality applies to all equilibrium methods of nuclear orientation. However, several nonequilibrium or dynamic methods of orienting nuclei have been proposed and carried out.[4-8] These are not discussed here. Nuclear orientation naturally breaks down into two distinct classifications, nuclear polarization and nuclear alignment. When nuclear polarization is achieved, both the directions and the senses of the nuclear spins are identical. When nuclear alignment is achieved, only the directions of the nuclear spins are identical. This may be stated alternatively in terms of the expectation value of M, the component of the nuclear spin I along the axis of orientation. For $\langle M \rangle \neq 0$ polarization exists. For $\langle M^2 \rangle = I(I + 1)/3 \neq 0$ alignment exists.

In practice, nuclear orientation is achieved by situating the nucleus in an electromagnetic environment that removes the degeneracy of the magnetic substates of the nuclear spin system. Then the existence of the nuclear orientation is observed by one or more of several techniques such as observing emitted radiation from the nuclear spin system, observing resonance of the system, and observing the scattering of particles from the system. In Table I are shown the six general methods of equilibrium nuclear orientation.[9-11]

Table I. Methods of nuclear orientation

Method	Axis of orientation	Temperature (°K)	External magnetic field (gauss)	Nuclear environment
1. External field polarization	External magnetic field	0.01	10^5-10^6	Nonmagnetic; In^{115} in In metal.
2. Magnetic hfs polarization	External magnetic field	0.01	10^2-10^3	Paramagnetic crystal with ions exhibiting hfs; Co^{60} in cerium magnesium nitrate.
3. Ferromagnetic polarization	External magnetic field	0.01	10^3	Ferromagnetic solid; Au^{198} in iron.
3. Ferromagnetic alignment	Internal magnetic field	0.01	0	Ferromagnetic crystal; Co^{60} in cobalt single crystal.
4. Electric hfs alignment	Internal electric field	0.1	0	Crystal with large internal electric field and ions with electric quadrupole moment; U^{233} in rubidium uranyl nitrate
5. Magnetic hfs alignment	Internal magnetic field	0.01	0	Crystal with anisotropic internal electric field and ion exhibiting hfs; Ce^{137m} in neodymium ethylsulfate.
6. Antiferro-magnetic alignment	Internal magnetic field	0.1	0	Antiferromagnetic solid; Mn^{54} in manganous chloride.

Method 1 is the direct interaction of a nuclear magnetic moment with a large external magnetic field. Method 2 is the interaction of a nuclear magnetic moment with a large local magnetic field produced by unpaired electron spins and orbits, coupled with the interaction of these electrons with a small external magnetic field. Method 3 is the interaction of a nuclear magnetic moment with an internal magnetic field produced by ferromagnetic electrons which are assumed polarized to saturation by a small external field or, in the alignment method, by the internal magnetization of a single metal crystal. Method 4 is the interaction of a nuclear electric quadrupole moment with the gradient of the internal electric field of the crystal. Method 5, which was used exclusively in this work, is the interaction of a nuclear magnetic moment with a large local magnetic field produced by unpaired electron spins and orbits, coupled with the interaction of these electrons with the anisotropic internal electric field of the crystal. Method 6 is the interaction of a nuclear magnetic moment with an internal magnetic field, coupled with the orientation of the electron spins in some preferred direction which varies from crystal to crystal.

In each specific nuclear orientation experiment, the interaction is ordinarily not one but several of the above interactions. This fact is taken into account when experimental results are being interpreted.

B. Nuclear Parameters

Nuclear orientation is generally detected by measuring the spatial distribution and polarization of emitted nuclear radiation. The following formulae[11] refer to the angular distribution and polarization of γ radiation. Several papers similarly treat α and β radiation.[12]

For a single emission, the angular distribution of particles or quanta having total angular momentum I, with z component m, is

$$I_m(\theta) = \int \left| \overline{\Phi}_I^m (\theta, \phi, \mu) \right|^2 d\mu ,$$

where Φ_I^m is the angular part of the particle or quantum wave function with θ and ϕ its angular coordinates, and the integration is over the spin coordinates of the particle or quantum μ. Therefore $I_m(\theta)$ is the intensity measured with spin-insensitive detectors.

For γ radiation of multipolarity L and z component M, the above equation can be expressed as a sum of even Legendre polynomials to give $I_m^L(\theta)$. These $I_m^L(\theta)$ are first multiplied by the appropriate vector addition coefficients and summed over m to give $I_M^L(\theta)$, then multiplied by the relative population $W(M)$ of each magnetic substate M, and finally summed over M to give

$$I(\theta) = \sum_M W(M) I_M^L(\theta) = \sum_M W(M) \sum_m |C(I_1 L I_0; M\text{-}m\ m)|^2 I_m^L(\theta)$$

$$= \sum_{k=0}^{\lambda} B_k(I_0, T) F_k(L I_1 I_0) P_k(\cos\theta),$$

where I_0 is the angular momentum of the initial state of the nucleus, I_1 is the angular momentum of the final state, λ equals the smaller of $2L$ or $2I_0$, B_k is the orientation parameter (see II.C), T is the temperature of the nuclear spin system, F_k is a function of all the angular momenta involved in the transition, $P_k(\cos\theta)$ is the Legendre polynomial of order k, and k is an even integer.

The treatment can be extended to cover the situation where the observed radiation is a mixed γ transition and is preceded by one or more unobserved pure or mixed α, β, or γ transitions.

For the decay sequence

$$I_0 \xrightarrow{L_1, L_1'} I_1 \longrightarrow \cdots I_{n-1} \xrightarrow{L_n, L_n'} I_n \longrightarrow I_{n+1} \cdots,$$

in which the radiation L_1 and an amplitude δ_1 of admixed component L_1' is unobserved, in which the radiation L_2 and an amplitude δ_2 of admixed component L_2' is unobserved, $\cdots$, and in which the γ

radiation of multipolarity L_n and an amplitude δ_n of admixed component of multipolarity L'_n is observed, we can write

$$I(\theta) = \sum_k B_k(I_0, T)U_k(I_0, L_1, L'_1, I_1 \cdots I_{n-1})F'_k(L_n I_{n+1} I_n)P_k(\cos\theta), \quad \text{(II-1)}$$

where U_k is a function of $\delta_1, \cdots, \delta_{n-1}$ and the angular momentum of all transitions preceding the one observed, F'_k is a function of δ_n, L_n, I_{n+1}, and I_n, and θ is the angle between the axis of orientation and the direction of propagation of the observed quantum. The even integer k is summed from 0 to the least of $2I_0, 2I_1, \cdots, 2I_{n-1}$, $2L'_1, 2L'_2, \cdots, 2L'_n$. For each transition, because of half-life considerations, there are seldom more than two components present, and therefore the above equation treats only pure transitions or mixed transitions of two components. However, for first-forbidden β decay, $L = 0$, 1, and 2 may be present. This is taken into account by using the appropriate U_k.

If the plane polarization of the γ radiation is observed, Eq. (II-1) becomes

$$I(\theta, \phi) = \sum_k B_k U_k \left[F'_k P_k + \cos(2\phi) F''_k P_k^{(2)} \right], \quad \text{(II-2)}$$

where $F''_{k_{L_n}}$ is a function of the electric or magnetic character of the observed 2^{L_n} pole radiation and of δ_n, L_n, I_{n+1}, and I_n; $P_k^{(2)}$ is the associated Legendre polynomial; and ϕ is the angle between the electric field vector of the polarized quantum and the plane containing the axis of orientation and the initial direction of propagation of the observed quantum.

In no experiment to date has it been found necessary to go to terms in k beyond 4 in Eq. (II-1) and (II-2) in order to completely interpret the data. Therefore Eq. (II-1) can be written as

$$I(\theta) = 1 + B_2 U_2 F'_2 P_2 + B_4 U_4 F'_4 P_4 , \quad \text{(II-3)}$$

and Eq. (II-2) for $\theta = 90$ deg (the angle at which the polarization effect is generally largest and the angle that was used for all polarization measurements in this work) gives the ratio defined as p to be

$$p = \frac{I(90^o,\ 0^o)}{I(90o,\ 90o)} = \frac{1 + B_2U_2(-\frac{1}{2}F'_2 + 3F''_2) + B_4U_4(\frac{3}{8}F'_4 - \frac{15}{2}F''_4)}{1 + B_2U_2(-\frac{1}{2}F'_2 - 3F''_2) + B_4U_4(\frac{3}{8}F'_4 + \frac{15}{2}F''_4} . \tag{II-4}$$

In the case of mixed M1 and E2 radiation (the most common case in nuclear orientation work) and for the decay sequence $I_1 \xrightarrow{1,2} I_2$, where the dipole radiation has an amplitude δ of quadrupole radiation, the values are

$$F''_2(1I_2I_1) = \left[\frac{1}{2}F_2(11I_2I_1) + \frac{1}{2}\delta^2 F_2(22I_2I_1) - \frac{1}{3}\delta F_2(12I_2I_1)\right] \Big/ (1+\delta^2), \tag{II-5}$$

$$F''_4(1I_2I_1) = -\frac{1}{12}\left[\frac{\delta^2}{1+\delta^2}\right] F_4(22I_2I_1) . \tag{II-6}$$

The functions $F_k(LL'I_2I_1)$ are conveniently tabulated in the literature[13] for large ranges of L, I_2, and I_1.

In mixed M4 and E5 radiation (the only case measured to date is that of Ce^{137m} in this work) and for the decay sequence $I_1 \xrightarrow{4,5} I_2$, where the 2^4 pole radiation has an amplitude δ of 2^5 pole radiation, one can write

$$F''_2(4I_2I_1) = \left[-\frac{5}{17}F_2(44I_2I_1) + \frac{5}{18}\delta^2 F_2(55I_2I_1) - \frac{5}{6}\delta F_2(45I_2I_1)\right] \Big/ \left[1+\delta^2\right], \tag{II-7}$$

$$F''_4(4I_2I_1) = \left[-\frac{1}{9}F_4(44I_2I_1) + \frac{1}{9}\delta^2 F_4(55I_2I_1) - \frac{1}{18}\delta F_4(45I_2I_1)\right] \Big/ \left[1+\delta^2\right]. \tag{II-8}$$

The theory of gamma radiation from oriented nuclei is essentially completed for the case in which the nuclear states involved in the decay sequence preceding the observed γ radiation all have lifetimes less than about 10^{-10} second. However, for longer lifetimes, complicated solid-state interactions may occur and cause attenuation effects to appear, e.g., K capture may change the electromagnetic environment of the nucleus quickly enough to affect the emission of the quantum. Attenuation effects have been extensively studied in γ-γ correlation work.[14, 15] Attenuation effects have been approached both quantitatively and qualitatively in the case of nuclear orientation.[16-18]

C. Crystal Field Parameters

The orientation parameter B_k, mentioned in II.B, is defined as

$$B_k = \sum_M (2k + 1)^{1/2} C(IkI;MO)\ W(M),$$

where I is the angular momentum of the oriented nucleus, k is an even integer from 0 to $2I$ ($B_k = 0$ for $k > 2I$, therefore for spin 1/2 nuclei, $I(\theta) = 1$ and $p = 1$ at all temperatures), C is a vector addition coefficient, M is the magnetic quantum number of the oriented nucleus and is summed from $-I$ to $+I$, and $W(M)$ is the statistical probability of finding a nucleus in substate M. For an ensemble of nuclei in thermal equilibrium, $W(M)$ is given by the Boltzmann function as

$$W(M) = \exp(-E(M)/kT) \Big/ \sum_M \exp(-E(M)/kT),$$

where $E(M)$ is the energy of the nuclear substate with a magnetic quantum number M, k is Boltzmann's constant, and T is the temperature of the nuclear ensemble.

Consequently, once the $E(M)$ are known, nuclear orientation experiments give results for U_k, F'_k, and F''_k, therefore for the angular momenta involved in a decay sequence. Conversely, once the angular momenta are known, orientation experiments give results for

E(M), which is a function of the electromagnetic interactions of a nucleus with its environment. In these experiments on Ce isotopes, the angular momenta involved in the decay sequence were generally known, so information was obtained on E(M).

The quantities E(M) are most often discussed in terms of the Abragam-Pryce Hamiltonian[19] $\mathcal{H}$, which satisfies the condition

$$\mathcal{H}\,\Psi(M) = E(M)\,\Psi(M)\ ,$$

where $\Psi(M)$ is the wave function of the ion or atom or groups of such that provide the electromagnetic environment of the oriented nuclei. If this environment possesses cylindrical symmetry about the z axis, the axis of orientation (for other cases, the Hamiltonian has been calculated),[20, 21] the Hamiltonian has the form

$$\mathcal{H} = -\frac{\mu_N}{I}\ \vec{H}\cdot\vec{I} + \beta_B\left[g_{\parallel} H_z S_z + g_{\perp}\,(H_x S_x + H_y S_y)\right] + A S_z I_z$$

$$+ B(S_x I_x + S_y I_y) + D\left[S_z^2 - \frac{1}{3}\,S(S+1)\right] + P\left[I_z^2 - \frac{1}{3}\,I(I+1)\right]$$

$$+ \mathrm{NIP} + \mathrm{TDP}\ ,$$

where μ_N is the nuclear magnetic dipole moment, $\vec{H}$ is the applied magnetic field, $\vec{I}$ is the angular momentum of the oriented nucleus, β_B is the Bohr magneton, $g_{\parallel}$ and $g_{\perp}$ are the ionic g factors parallel and perpendicular to the z axis, A and B are the hfs interaction constants, D is the constant for interaction between the ion and the crystalline field, S is defined by setting the multiplicity of the populated electronic levels equal to $2S + 1$, P is the constant for interaction between the nuclear electric quadrupole moment and the crystalline electric field gradient, H_i, S_i, and I_i are the standard operator notations, NIP represents neighboring-ion perturbations that affect E(M), and TDP represents time-dependent perturbations that affect E(M).

In a particular orientation experiment, the relative magnitude of each of these eight terms in the Hamiltonian determines which of the six cases of nuclear orientation will be dominant. In these experiments on Ce nuclei, incorporated into a neodymium ethylsulfate nonahydrate lattice, no external magnetic field was applied, so the first two terms drop out of the Hamiltonian. The fifth term drops out because the ground state of the Ce^{+3} ion in such a lattice is a doublet, therefore $S = 1/2$, and $D = 0$. The seventh term often represents a magnetic dipole-dipole interaction between neighboring ions.[22] For nuclear alignment, this interaction leaves B_k unchanged when the off-diagonal matrix elements are small. The eighth term represents those interactions utilized for the dynamic orientation of nuclei.

Therefore the Hamiltonian for these experiments becomes

$$\mathcal{H} = AS_zI_z + B(S_xI_x + S_yI_y) + P\left[I_z^2 - \frac{1}{3}\ I(I+1)\right].$$

Cerium has no stable isotopes with a nonzero magnetic moment, and no resonance experiments have yet been done to measure A, B, and **P** in the ethylsulfate. However, Elliott and Stevens[23, 24] have successfully calculated these parameters, using experimental results on the crystal structure, the magnetic susceptibility, the Faraday effect, and the absorption spectra of $Ce(C_2H_5SO_4)_3 \cdot 9H_2O$. In addition, they used resonance results on small quantities of cerium in lanthanum ethylsulfate. Their calculated results for rare earth ions (except gadolinium, which is in an S state) in crystals with anisotropic internal electric fields are

$$A = \frac{4\beta_B\beta_N\mu_N}{I}\ \langle r^{-3}\rangle\ \langle +\,|\,N_z\,|\,+\rangle\,,$$

$$B = \frac{4\beta_B\beta_N\mu_N}{I}\ \langle r^{-3}\rangle\ \langle +\,|N_x|\,-\rangle\,,$$

$$P \approx \frac{-9e^2Q}{4I(2I-1)}\ \langle r^{-3}\rangle\ \langle J\|\,\alpha\,\|J\rangle\ \langle +\,|\,J_z^2 - \frac{1}{3}\ J(J+1)\,|\,+\rangle\,,$$

where A, B, and P are given in units of cm^{-1}, β_B and β_N are the Bohr and nuclear magnetons, μ_N, Q, the nuclear electric quadrupole moment, and I refers to the oriented nucleus, $\langle r^{-3} \rangle$ is the expectation value for the 4f electrons of the rare-earth ion, $\langle \, | \, | \, \rangle$ and $\langle \, \| \, \| \, \rangle$ are matrix elements of the vector

$$\vec{N} = \sum_{\substack{\text{elec-} \\ \text{trons}}} \left\{ \vec{l}_i - \vec{s}_i - 3 \, (\vec{r}_i \cdot \vec{s}_i) \, r_i / r_i^2 \right\}$$

between states of total ionic angular momenta characterized by $\pm J_z$.

The value of $\langle r^{-3} \rangle = 24.7 \times 10^{+24}$ cm^{-3} for the Ce^{+3} ion's single 4f electron was taken from the calculations by Judd and Lindgren,[25] and is accurate to at least ± 5% and possibly ±1%. This value is based on spin-orbit coupling data and differs slightly from the Hartree self-consistent field calculations by Ridley,[26] but differs significantly from the hydrogenic wave function calculations by Bleaney.[27]

The matrix elements in the above expression can be evaluated by using the experimentally deduced wave function of Elliott and Stevens for the Ce^{+3} ion. The free ion Ce^{+3} has the configuration $4f^1$ and the ground term $^2F_{5/2}$. In a trigonal crystalline field this term is split into doublets characterized in the first approximation by $\Psi = |\pm J_z \rangle$. Therefore, in the ethylsulfate lattice, at a site of C_{3h} symmetry with a slight deviation from D_{3h} symmetry, this term is split into such doublets.

The lowest-energy Kramer's doublet, the only doublet significantly populated at $T < 1^oK$, is composed mostly of the state $| \pm 5/2 \rangle$ with admixtures from the $^2F_{5/2}$ ground term and the next higher energy term $^2F_{7/2}$, so that one has

$$\Psi = \cos \alpha \, | \pm 5/2 \rangle \mp e^{i\beta} \sin \alpha \, | \mp 1/2 \rangle ,$$

where $\alpha = 8^o \, 50'$, $\beta \approx 90^o$ is a phase factor based on the relative orientation of the surroundings which give rise to the C_{3h} and the C_{3v} terms, and

$$| 5/2 \rangle = p \, | \, l_z = 2, \; s_z = 1/2 \rangle + q \, | \, l_z = 3, \; s_z = -1/2 \rangle + r \, | \, l_z = -3, \; s_z = -\frac{1}{2} \rangle ,$$

with $p = -0.3649$, $q = 0.9154$, $r = -0.1703$, and

$$| -1/2 \rangle = -\cos\theta \, | \, l_z = -1, \; s_z = 1/2 \rangle + \sin\theta \, | \, l_z = 0, \; s_z = -1/2 \rangle ,$$

with $\theta = 49^{\circ}\, 24'$. The $| -5/2 \rangle$ and $| 1/2 \rangle$ are the Kramer's conjugate to the above states.

This wave function of Elliott and Stevens[24] is that for the 4f electron of a Ce^{+3} ion in a lattice site of a $Ce(C_2H_5SO_4)_3 \cdot 9H_2O$ crystal. However, the function has been found appropriate[28, 29] for a Ce^{+3} ion in a lattice site of isomorphic $Nd(C_2H_5SO_4)_3 \cdot 9H_2O$, such as was used in these experiments.

By use of this wave function, the parameter A was calculated (by Haag and co-workers; see Ref. 50) to be

$$A = 0.074 \, \mu_N / I \ \text{cm}^{-1}, \tag{II-9}$$

Since $B << A$, and $P << A$, the wave function with $\alpha = 0^{\circ}$ was used as an adequate approximation to give

$$\left| \frac{B}{A} \right| = \frac{1}{43.5} , \quad \frac{P}{A} \approx \frac{0.22}{2I - 1} \left(\frac{Q}{\mu_N} \right) .$$

The parameter B alters the energy levels of the hyperfine-structure multiplet slightly. However, calculations showed that the small effect of this alteration was within the statistical error of the experimental measurements, so that the B term could be neglected in the Hamiltonian.

Calculations indicated that P also had a negligible effect on nuclear alignment of the Ce nuclei. In fact, these experiments showed no effects due to this P term in the Hamiltonian. Table II shows the shell-model calculations[30] of Q for each of the five isotopes studied.

Table II. Shell-model calculated values of Q

Isotope	I	Neutron configuration	Q (barns)
Ce^{137m}	11/2	$(h_{11/2})^9$	+0.28
Ce^{137}	3/2	$(d_{3/2})^3$	+0.24
Ce^{139}	3/2	$(d_{3/2})^3$	+0.24
Ce^{141}	7/2	$(f_{7/2})^1$	-0.40
Ce^{143}	7/2	$(f_{7/2})^1$	-0.40

The neutron configurations were based on spectroscopic results and on the results of this work. These calculated Q, together with our experimental μ_N, indicate that P is always less than 4% of A. Thus, the lack of experimental effects due to P appears quite reasonable.

In summary, the Hamiltonian used in interpreting these experimental results was

$$\mathcal{H} = AS_zI_z$$

Consequently, the hfs interaction lifts the degeneracy of the nuclear magnetic substates M into 2I + 1 doublets, $|\pm I_z\rangle$, separated by $A/2\ cm^{-1}$.

All experimental values of μ_N were obtained by utilizing equation I-9 in the convenient form

$$|\mu_N| = 18.8\, I\, \beta\, T \qquad \text{(II-10)}$$

where $\beta = A/(2kT)$ and T is the measured temperature of the nuclear spin system. The parameter β has been tabulated[31] as a function of B_k for each value of I. Therefore, experimentally measured B_k were used to find β and thus μ_N. The sign of μ_N cannot be determined in nuclear alignment experiments, thus these experiments give only the magnitude of μ_N.

D. Computational Procedure

The corrections made to the raw data taken in these experiments are given below. Data were taken on temperature, γ-ray intensity as a function of temperature, and γ-ray plane polarization as a function of temperature. In addition, the procedure given below was used in proceeding from these corrected data to values for the nuclear magnetic moment, the multipolarity of the observed γ rays, and the angular momenta involved in the decay sequences.

1. Corrections to temperature data

At the beginning of each experiment on one of the Ce isotopes, a calibration was made of the change in magnetic susceptibility with temperature of the neodymium ethylsulfate crystal containing the Ce isotope. In other words, Curie's Law, $\chi = C/T$, was measured. (See III.B and V.)

The susceptibility of neodymium ethylsulfate follows Curie's Law down to about 0.5°K. At lower temperature, a "temperature," T^*, is defined so that the susceptibility obeys the equation $\chi = C/T^*$. The constant C was determined from the measured straight-line slope of χ versus $1/T$ from 4.2°K to 1.2°K.

The relation between T^* and T from $0.02^\circ K$ to $1.2^\circ K$ is known from the heat-capacity measurements by Meyer[32]. Figure 1 is a curve of this relationship, based on Meyer's data. The $T_\perp^*$ corresponds to measuring the susceptibility of the crystal perpendicular to its axis of symmetry, the c axis. As is expected, the curve illustrates the greatest divergence of T^* and T at the lowest temperatures.

Following an adiabatic demagnetization, the temperature of the ensemble of Ce nuclei was determined from the equation

$$(1/T^*)_f = 1/C\,(\chi_f - \chi_i) + (1/T^*)_i\,, \qquad \text{(II-11)}$$

where $(1/T^*)_i$ refers to the temperature (corresponding to that of the liquid helium bath) of the ensemble immediately prior to the time of demagnetization, χ_i is the corresponding susceptibility of the neodymium ethylsulfate crystal, and $(1/T^*)_f$ and χ_f (measured with the mutual-inductance bridge) are the values following the demagnetization.

The measured quantity χ_f was, before being substituted into Eq. (II-11), corrected for the perturbing influence of the γ-ray counters (located about 10 cm from the crystal) or the polarimeter (located about 4 cm from the crystal) on the susceptibility measurements. This influence was measured at $4.2^\circ K$ and at $1.2^\circ K$ by taking susceptibility readings both with the counters in place and at a distance of 3 feet. The difference (the same at both temperatures) in the readings was taken as a constant for lower temperatures. The magnitude of the correction, which was subtracted from the measured χ_f, amounted to a 0.5% correction at $1/T = 50$ and a 2% correction at $1/T = 10$.

Next, the values of $(1/T^*)_f$, calculated with a corrected χ_f from Eq. (II-11), were corrected for the nonellipsoidal shape of the crystal. Immediately prior to each demagnetization, the values of T_i and the applied magnetic field H_i were recorded. The ratio H_i/T_i has been measured by Meyer as a function of T_f^* for an ellipsoidal crystal of neodymium ethylsulfate. The difference between Meyer's

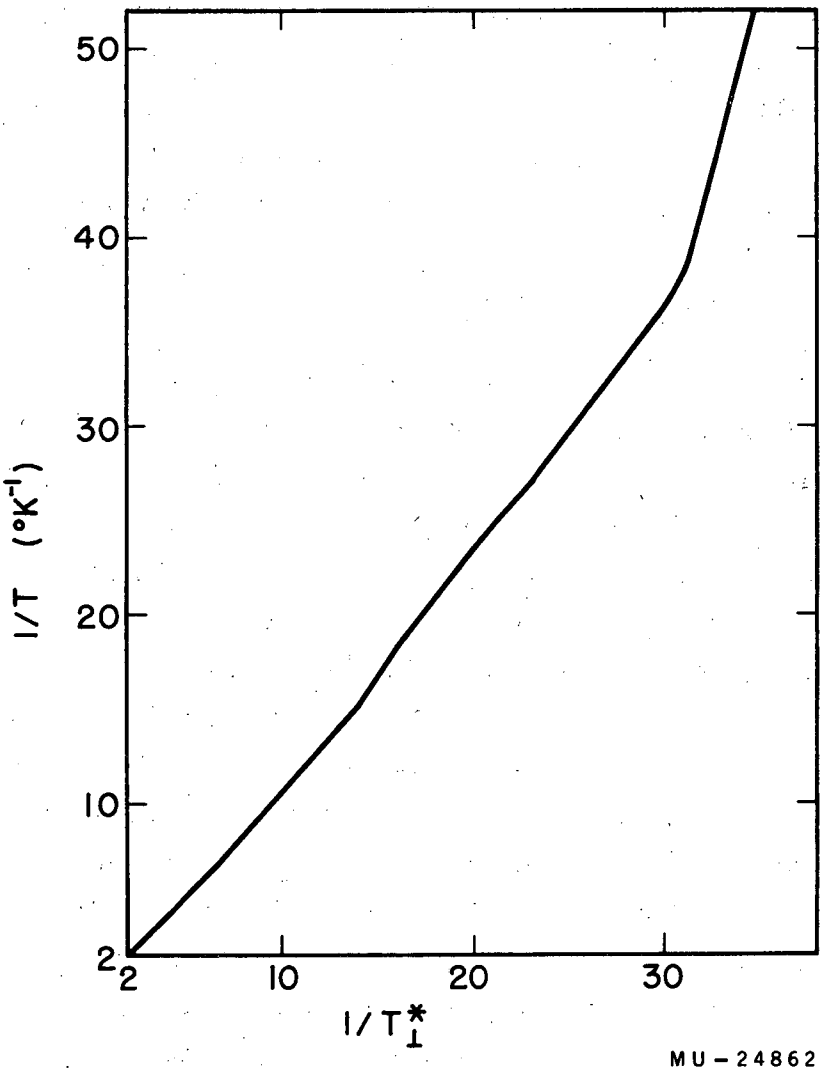

Fig. 1. 1/T versus $1/T^*$ relationship for neodymium ethylsulfate.

T_f^* and our calculated T_f^* was a constant at all temperatures. The magnitude of this correction, which was added to the T_f^* calculated in Eq. (II-11), amounted to a 10% correction at $1/T = 50$ and a 3% correction at $1/T = 10$.

2. Corrections to intensity data

Each intensity measurement, consisting of the ratio of a low-temperature γ-ray count to a $1.2^{\circ}K$ γ-ray count, was corrected for

a. background,

b. Compton distribution due to other γ-ray peaks,

c. electronic "dead time" of the pulse-height analyzer,

d. geometry of the counter,

e. shifts in the gain of the counters, and

f. half life of the isotope which was oriented.

a. At the end of each experiment, the Ce activity was removed from the counting room and a background count taken for at least ten times the length of each previous γ-ray count. The background correction was from 1 to 5%, depending on the amount of Ce activity.

b. With the exception of Ce^{143}, each Ce isotope aligned had only one γ ray. Each γ-ray peak counted in the Ce^{143} experiment was corrected for the background due to Compton scattering from higher-energy γ rays. This was done by using sources of Na^{22}, Cs^{137}, Mn^{54}, and Co^{60} and measuring the Compton distribution of each of their γ rays. Furthermore, care was taken in these measurements to place these sources inside a cylinder which had the same scattering properties as our orientation apparatus. This was done because during an experiment, before reaching the counter, the γ radiation passed through about 1 cm of glass and 10 mils of Cu. This scattered several percent of the γ rays to lower energies which were then recorded in the counters. The cylinder duplicated this effect when making measurements on the sources.

c. The 100-channel "Penco" pulse-height analyzer (see III.C) visually indicated with a gauge the amount of electronic dead time during

a count. If this reading was different for the low-temperature count and for the 1.2°K geometric normalization count, the appropriate correction was made. The 256-channel "TMC" analyzer (see III. C) automatically corrected itself by means of a timing unit so that the electronic counting time was constant regardless of counting rate.

d. Equation (II-1) refers to the intensity of a γ ray as measured by point counters. For finite-size counters, this equation becomes

$$\overline{I(\theta)} = \sum_k Q_k B_k U_k F_k P_k ,$$

where $\overline{I(\theta)}$ is the observed intensity in the finite-size counters and Q_k is a function of the absorption coefficient of the observed γ quantum, the dimensions of the counter, the dimensions of the source, and the distance from the counter to the source. This function may be calculated.[33] In each experiment, the source-counter distance was measured and Q_k found from graphs of Q_k versus the energy of the observed quantum for a 3-by-3-in. NaI(Tl) crystal.

e. Occasionally, during the period of time between a low temperature count and the corresponding 1.2°K count, the over-all gain of the counter would shift, even though regulated voltage supplies were being used. This shift was always less than 0.5 volt, as indicated by the pulse-height spectrum. This shift was cyclical, with a period varying erratically from 2 to 15 minutes. Therefore, by using the data from one of several successive 1.2°K counts, the gain setting of the low-temperature count could quite satisfactorily be reproduced.

f. The decrease in the Ce activity between the average time for the low-temperature count and the average time of the following 1.2°K count was corrected by means of the standard half life formula. The largest correction was 0.3%.

3. Corrections to polarization data

Equation (II-2) refers to the intensity of plane polarized γ rays as measured with a point source, a point scatterer, and a point counter. For finite-size dimensions, a correction is conveniently made to the experimental data in such a manner that the result is a ratio of intensities defined as p in Eq. (II-4). Below is given the theory for making this correction, and Part III. D gives the experimental work done to measure this correction.

A plane polarized quantum has associated with it an electric field vector perpendicular to its direction of propagation and in the plane of vibration which is constant in space. This quantum inelastically interacts with an electron so that the quantum is preferentially scattered into a plane perpendicular to its electric field vector. An analogous situation is a dipole antenna which radiates preferentially in a plane perpendicular to its length. A comprehensive review article on γ-ray polarization and its detection is that by Fagg and Hanna.[34]

The Compton scattering of γ rays is therefore a polarization-sensitive process. A polarimeter for this purpose was built based on the one built by Metzger and Deutsch in 1950.[35] This is described in Part III. D. It consisted basically of an anthracene crystal to scatter the incident quanta, and two NaI crystals, at 90 deg to each other, to record the ratio of the intensities of the scattered quanta.

Measured experimentally were the quantities $N_{\parallel}$, the intensity of quanta scattered in the plane containing the axis of orientation and the initial direction of propagation of the quanta, and $N_{\perp}$, the intensity of quanta scattered perpendicular to this plane. The ratio of these measured intensities may be expressed as

$$N = \frac{N_{\parallel}}{N_{\perp}} = \frac{I(90^{\circ}, 0^{\circ}) \times d\sigma(0^{\circ}) + I(90^{\circ}, 90^{\circ}) \times d\sigma(90^{\circ})}{I(90^{\circ}, 0^{\circ}) \times d\sigma(90^{\circ}) + I(90^{\circ}, 90^{\circ}) \times d\sigma(0^{\circ})} \quad , \quad \text{(II-12)}$$

where $I(\theta, \phi)$ corresponds to Eq. (II-2) and $d\sigma(\eta)$ is the Klein-Nishina[36] differential cross section for Compton scattering, averaged over all polarizations of the scattered quanta.[37] The quanta emitted at $\theta = 90$ deg (the angle used in our experiments, as it gave the largest difference between $N_{\parallel}$ and $N_{\perp}$) to the axis of orientation (the c axis of the neodymium ethylsulfate crystal) may be plane polarized in only two planes, i.e., with $\phi = 0$ deg and $\phi = 90$ deg. Consequently, $N_{\parallel}$ and $N_{\perp}$ each have only two terms in the expression above.

The $d\sigma(N)$ is given by

$$d\sigma(\eta) = \frac{r_0^2}{2} \, d\Omega \, \frac{a^2}{a_0^2} \left(\frac{a}{a_0} + \frac{a_0}{a} - 2 \sin^2 \delta \cos^2 \eta \right), \qquad \text{(II-13)}$$

where $r_0 = e^2/mc^2$ is the classical radius of the electron of mass m and charge e, c is the velocity of light, $d\Omega$ is the element of solid angle, the energy of the scattered quantum in units of mc^2 is

$$a = a_0 / [1 + a_0(1 - \cos \delta)] ,$$

where a_0 is the initial energy of the quantum in units of mc^2, δ is the angle of scattering, and η is the angle between the direction of polarization (electric field vector direction) of the incident quantum and the plane of scattering. The η dependence of the Klein-Nishina cross section, Eq. (II-13), shows a maximum at $\eta = 90$ deg and a minimum at $\eta = 0$ deg. It was for this reason that the two NaI crystals of the polarimeter were mounted at 90 deg to each other.

It should be noted that the angle η is represented by the symbol ϕ in some publications.[38] This is a somewhat confusing terminology, since the symbol ϕ is also widely used to denote the angle defined in Eq. (II-2).

Rewriting Eq. (II-12) gives

$$p = \frac{I(90^\circ, 0^\circ)}{I(90^\circ, 90^\circ)} = \frac{N - R}{1 - NR} , \qquad \text{(II-14)}$$

where $N = N_{\parallel}/N_{\perp}$ and R is the ratio of two differential cross sections. In the case of ideal geometry, $R = d\sigma(90^\circ)/d\sigma(0^\circ)$. In the case of real geometry, i.e., finite-size source, scatterer, and counter, R is the ratio of two differential cross sections each of which has been integrated over appropriate angles δ and η. This value of R for the geometry of our polarimeter was measured experimentally as described in Part III. D.

In summary, the only correction necessary to the γ-ray plane-polarization measurements made in these experiments was the geometry correction R. For each Ce isotope studied, the value of $N = N_{\parallel}/N_{\perp}$ as a function of T was measured, and then corrected with R by means of Eq. (II-14) to give the desired function p.

4. Use of corrected data for final calculations

After $I(\theta)$ and p had been determined experimentally as functions of $1/T$ for an observed γ ray, the following general technique was used to set limits on δ, the amplitude of 2^{L+1} pole radiation admixed with the 2^L radiation, for the observed γ ray. The $I(\theta)$ and p deviated most from a value of 1 at the largest $1/T$ achieved in these experiments, i.e., at $1/T = 50$. Consequently, the values measured at this temperature were used in evaluating the following equations.

If the measured $I(0^\circ)$ was greater than 1, Eq. (II-3) gave

$$B_2U_2F_2' + B_4U_4F_4' > 0;$$

therefore

$$F_2' > -\left(\frac{B_4U_4}{B_2U_2}\right) F_4' .$$

Similarly, for $I(90^\circ) < 1$,

$$F_2' > 3/4 \left(\frac{B_4U_4}{B_2U_2}\right) F_4' ,$$

and for $p > 1$, Eq. (II-4) gave

$$F_2'' > 5/2 \frac{B_4U_4}{B_2U_2} F_4'' .$$

Extending this technique to all possible combinations of $I(0^\circ)$, $I(90^\circ)$, and p gives Table III.

Table III. Boundary conditions on δ

	$I(0^\circ)>1, I(90^\circ)<1$	$I(0^\circ)<1, I(90^\circ)>1$	$I(0^\circ)>1, I(90^\circ)>1$	$I(0^\circ)<1, I(90^\circ)<1$
	$F_2' > A'_{min}$	$F_2' < A'_{max}$	$F_2' > A'_{min}$	$F_2' < A'_{max}$
$p > 1$	$F_2'' > B'_{min}$	$F_2'' < B'_{max}$	$F_2'' < B'_{max}$	$F_2'' > B'_{min}$
	$F_2'' > C'_{min}$	$F_2'' > C'_{min}$	$F_2'' > C'_{min}$	$F_2'' > C'_{min}$
	$F_2' > A'_{min}$	$F_2' < A'_{max}$	$F_2' > A'_{min}$	$F_2' < A'_{max}$
$p < 1$	$F_2' > B'_{min}$	$F_2' < B'_{max}$	$F_2' < B'_{max}$	$F_2' > B'_{min}$
	$F_2'' < C'_{max}$	$F_2'' < C'_{max}$	$F_2'' < C'_{max}$	$F_2'' < C'_{max}$

In Table III,

$A' = - \left(\frac{B_4U_4}{B_2U_2}\right) F_4' (LI_2I_1)$, $B' = 3/4 \left(\frac{B_4U_4}{B_2U_2}\right) F_4' (LI_2I_1)$,

$C' = 5/2 \left(\frac{B_4U_4}{B_2U_2}\right) F_4'' (LI_2I_1)$ and the subscript "min" or "max" indicates that A', B', and C' are to be evaluated at either their algebraic

minimum or maximum. The limits calculated for δ by this technique are those that insure the correct algebraic sign for the quantities $I(90^{\circ})$, $I(0^{\circ})$, and p. The technique has been found in this work to succeed over "trial-and-error" methods, as it reveals all possible δ that may satisfy the experimental results.

For each Ce isotope aligned, the over-all sequence of computations performed to determine a μ_N, a δ for the observed γ ray, and the angular momenta involved in the decay scheme is:

(a) Select a reasonable decay scheme based on spectroscopic results obtained by other workers for the isotope and its daughter. Consequently, all angular momenta I_0, I_1, $\cdots$, I_n involved in the decay are assigned fixed values.

(b) Using these values, calculate U_2, U_4, and the four functions of δ, F_2', F_2'', F_4', and F_4'', in terms of δ.

(c) Using the values I_0, $1/T = 50$, and, depending on which limit, "min" or "max", is used for A', B', and C', $\mu_N = 0$ or $\mu_N = \infty$, calculate the ratio B_4/B_2. (for nuclei that approximate shell-model nuclei, as the Ce nuclei were found to, the Schmidt limit[39] may be used instead of $\mu_N = \infty$. All such nuclei, to date, possess a magnetic moment less than the Schmidt limit.)

(d) Evaluate A, B, and C and find the limitations F_2' and F_2''. Using a graph of these two functions versus δ (see Part VI), determine the boundary conditions on δ.

(e) Choose a reasonable μ_N for the isotope and calculate $I(\theta)$ and p as a function of $1/T$ for various δ within these boundary conditions. Compare these results with the experimental $I(\theta)$ and p.

(f) Using several other values of μ_N, repeat calculation (e) until the calculated $I(\theta)$ and p correspond to the experimental $I(\theta)$ and p.

This sequence of calculations will yield a final, although not necessarily unique, value for μ_N and δ, with limits derived from both calculation (f) and such experimental factors as counting statistics. This calculation sequence may yield two or three discrete values for μ_N and

δ because of the experimental uncertainty in the measured $I(\theta)$ and p. Often, all but one value for μ_N and δ may be discarded if enough spectroscopic work has been done on the isotope. For example, internal-conversion coefficients or angular correlation measurements may show that a dipole-quadrupole transition is predominantly dipole, thereby limiting $|\delta|$ to a value less than 1.

For isotopes for which the angular momenta involved in the decay are not well known, several different decay sequences must be postulated and this entire calculation carried out again. In some cases, however, unique decay schemes may be assigned to the isotope, for example, when only one of two decay schemes gives the correct sign for $I(\theta)$ and p.

The mixing amplitude δ may occur with a value of either algebraic sign such that in general, $\infty > \delta > 0$ or $0 > \delta > -\infty$. Care was taken in interpreting these experimental results to arrive at the correct algebraic sign for δ.

III. EXPERIMENTAL APPARATUS

A. Nuclear Orientation System

Our nuclear orientation system consisted basically of three parts: a vacuum system for thermally isolating the crystal containing the oriented nuclei, a heat sink at a temperature of 1.2°K, and a magnet for demagnetizing the crystal to temperatures below 1.2°K.

1. Vacuum system

The vacuum system, shown in Fig. 2 (a), served to thermally isolate the crystal from its surroundings. In addition, the system provided a means of bringing the crystal into thermal equilibrium with these surroundings when desired.

In all the experiments in this work, a neodymium ethylsulfate nonahydrate single crystal was used to cool the nuclei of interest down to 0.02°K. This crystal was mounted with Duco cement in the plane framework A of Fig. 2(a). This framework, and the 30-cm-long rod from which it was suspended, was constructed of 2-mm-diameter glass rod. (In later experiments, the crystal was secured to a hod-shaped glass piece with an ordinary rubber band and then suspended on a 30-cm-long glass tubing of 2-mm diameter. This technique provided even better thermal isolation for the crystal.)

The 5-gram compressed salt pill B of $MnSO_4 \cdot (NH_4)_2SO_4 \cdot 24H_2O$ with a 2-mm hole (lubricated with vacuum grease as a heat-conducting agent) was mounted with Duco cement above the crystal. This pill served as a thermal shield for the crystal.

The 30-cm glass rod was joined to a 60-mil-diameter tungsten wire, which in turn was hard-soldered to the brass cap D. Then a glass tube of 3 cm diameter with a copper-glass seal C was placed around the crystal and soft-soldered to the brass cap. The glass portions of this assembly had the advantage of causing negligible interference to our ac susceptibility measurements. (see III. B) These were made with the primary and two secondary coils shown in place around the crystal in Fig. 2(a).

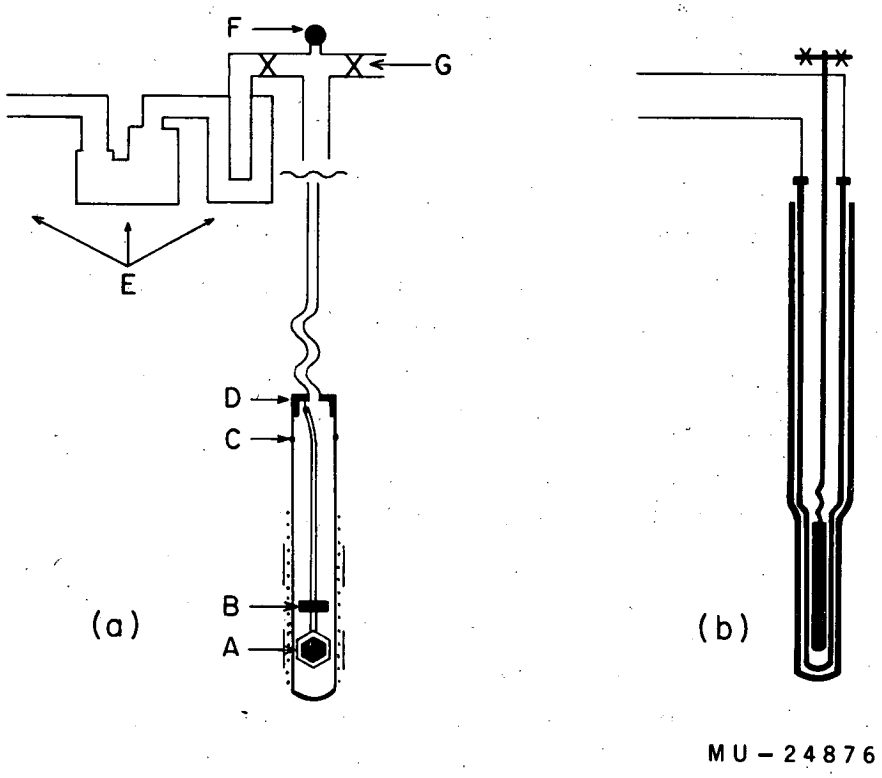

Fig. 2. Nuclear orientation system. The crystal mounting and vacuum system are shown in (a). The Dewars and liquid helium-4 pumping system are shown in (b).

The brass cap was hard-soldered to a 25-cm-long helix made of 3/8-in.-diameter copper tubing. This helix acted as a radiation trap, thus protecting the crystal from direct radiation from above. This helix was hard-soldered to a 70-cm stainless steel tube with 10-mil walls and a diameter of 3/8 in. This tube served as a low heat-conducting mechanical support for the crystal assembly. Finally, the stainless steel tube was connected to the conventional liquid nitrogen trap, oil diffusion pump, and rotary forepump system E.

Pressure readings were taken with the "Philips" electron vacuum gauge F mounted at the upper end of the stainless steel tube. These readings were a measure of the pressure inside the crystal chamber. At G a line for introducing helium gas into the crystal chamber was connected. The helium gas was used to bring the crystal into thermal equilibrium with the liquid helium heat sink surrounding the crystal assembly.

2. Heat sink

The heat sink system, shown in Fig. 2(b), consisted of a glass Dewar containing liquid nitrogen and surrounding a glass Dewar containing liquid helium, a pumping system for the liquid helium, and mercury and oil dibutyl pthalate (density of 1.0465 g/ml) manometers to record the vapor pressure of the liquid helium.

Each Dewar was constructed with internally silvered walls except for two 1-in.-wide vertical strips, 180 deg apart, running the full lengh of each Dewar. This permitted the visual determination of both the liquid nitrogen and liquid helium levels.

The helium Dewar was held in place by a metal collar which bolted onto the overhead liquid helium pumping line of 4-in. diameter. A rubber O ring provided a vacuum seal between the glass helium Dewar and the metal flange of the pumping line. The nitrogen Dewar was held in place by suspending it from the pumping line with three cushioned wires.

The pump used for lowering the vapor pressure of the liquid helium was a two-stage Kinney vacuum pump. This consisted of a Kinney

KMB-230 Mechnical Booster (speed of 230 cfm), backed by a Kinney KD-30 pump (speed of 30 cfm).

The helium Dewar held about 2 liters of liquid helium. Reducing the helium vapor pressure from 760 mm Hg to 1 mm Hg evaporated from 0.5 to 1.0 liter of helium. However, once a pressure of 1 mm Hg (our usual lowest operating pressure) was reached, our cryostat evaporated only 1 liter of liquid helium per 15 to 20 hours.

The outer diameter of the nitrogen Dewar was 15 cm in its upper portion and 7.5 cm in the portion surrounding the crystal chamber.

3. Magnet

The magnet was a General Electric 2-ton 100-kw water-cooled adjustable-height iron-core electromagnet. The pole tips were rectangular in cross section, 4 in. high by 2.5 in. wide. The air gap was adjustable from 1 in. to 4 in. At an air gap of 3 in., our standard operating condition, we achieved fields up to 17 kilogauss.

The magnet was mounted on wheels, which rested on two iron rails laid in the floor of the laboratory. This permitted moving the magnet more or less easily, depending on the potential energy of the mover, up to the cryostat for a magnetization. Upon demagnetization, within 5 seconds, the magnet was rolled about 3 feet away from the cryostat, so that the γ-ray counters could be rolled into place.

The effectiveness of a nuclear orientation system can be judged by the length of time a demagnetized crystal takes to warm up to the temperature of the surrounding liquid helium bath. In several published experiments on nuclear orientation results, this warm-up time has been given in units of seconds, i.e., the warm-up time has been short. In almost all published work, however, the warm-up time has been about from 20 to 60 minutes for the crystal to warm from its lowest temperature to 0.1°K. Therefore our orientation system, as judged by one of our better (though not atypical) warm-up curves of T versus time shown in Fig. 3, compares quite favorably with other orientation systems. In

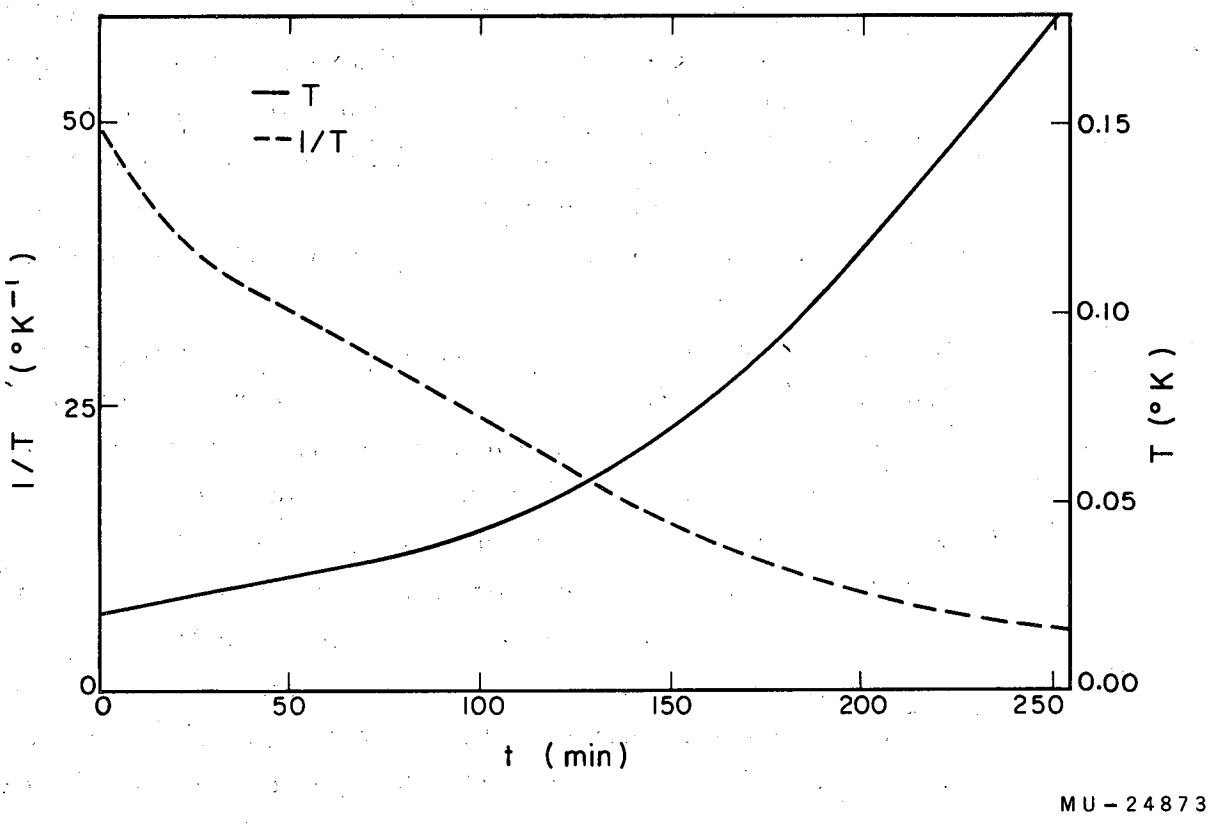

Fig. 3. Experimental curve of T (solid line) and 1/T (dashed line) versus time for a 15-gram neodymium ethylsulfate crystal.

this experiment, a 15-gram neodymium ethyl sulfate crystal, containing Ce^{137}, Ce^{137m}, and Ce^{139}, was used. A γ-ray count of 5 minutes was taken. The curve in Fig. 3 shows that the change in T over this interval is small, therefore the results should be meaningful.

B. Mutual-Inductance System

The absolute temperature of the demagnetized crystal was measured with a 20-cycle/second ac variable mutual-inductance bridge.[40] This consisted, as shown in Fig. 4, of a primary coil driven by an audio signal generator A, two secondary coils wound in opposition, a variable mutual-inductance bridge B, a frequency-selective amplifier C (similar to one manufactured by Sierra Co., Palo Alto, Calif.), and a cathode-ray oscilloscope D.

The neodymium ethylsulfate crystal formed a partial core for one of the two secondary coils. Its paramagnetic susceptibility, a function of temperature, unbalanced the signal from the two previously nulled secondaries. This imbalance produced a visual signal, in the form of an elliptical trace, on the oscilloscope. The bridge was used to add the appropriate amount of mutual inductance to the circuit so that the secondaries would be nulled. The secondaries were nulled both as to mutual inductance and as to loss component. The loss component was due to electrical losses in the coils, i.e., the voltage at the secondary coils was never exactly 90 deg out of phase with the primary current. This was caused, e.g., by energy absorbtion in the crystal. Therefore, this loss component was nulled by introducing a resistive voltage component in the secondary circuit with the bridge.

The primary coil was 24 cm. long and 3 cm.in. diam. It consisted of one layer of 250 turns/inch of No. 40 (B and S gauge) Formvar-insulated copper wire. The wire had a diameter of 3.24 mils, including the 0.05-mil layer of insulation. The coil was wound on a wooden cylinder mounted in a lathe and then covered with a thin layer of varnish to make it rigid.

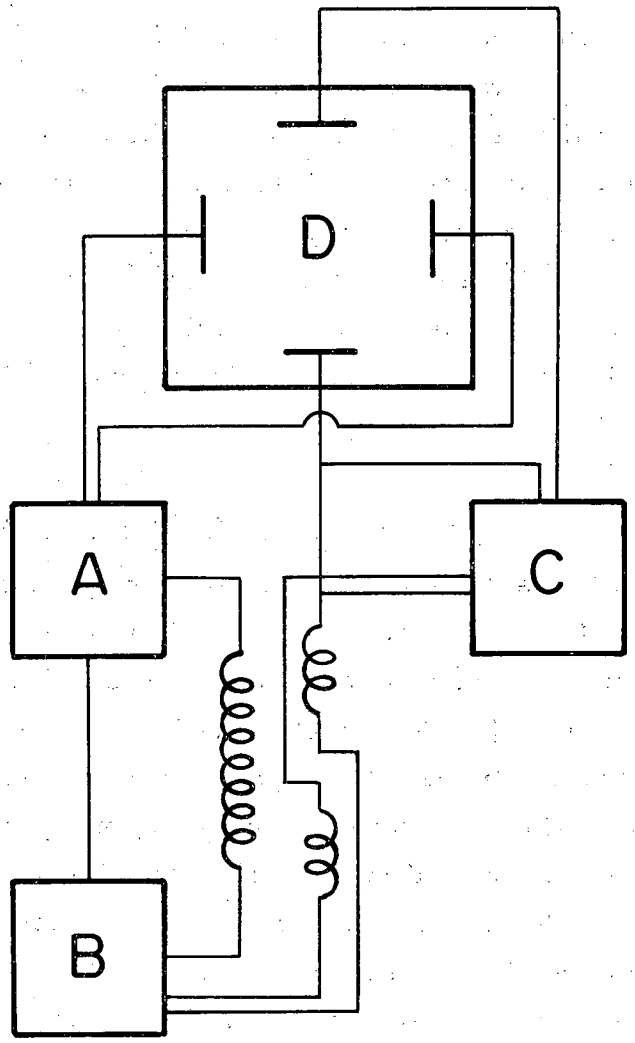

Fig. 4. Mutual inductance system schematic.

The two physically identical, but magnetically opposing, secondary coils were wound directly onto the primary coil using the same No. 40 wire. They were each 6 cm long and their geometric centers were symmetrically located 16 cm apart on the primary. Depending on the bulk susceptibility of the crystal used for the experiment, the number of layers of each secondary coil was from one to six layers.

The stability and reproducibility of this mutual-inductance system was quite satisfactory. In two series of measurements, separated by one month, on the same neodymium ethylsulfate crystal, the two measured curves for susceptibility versus 1/T had slopes within 0.5% of each other.

C. Gamma-Ray Counting System

In these experiments, 3x3-in. cylindrical NaI(Tl) scintillation crystals (Harshaw Chemical Co., Cleveland, Ohio) were used for γ-ray detection. They were optically mounted with white "Vaseline" petroleum jelly (Chesebrough-Pond's Inc., New York) to Dumont 6363 photomultiplier tubes. The applied high voltage was 1 kilovolt. The signal from the tubes was fed directly into a cathode-follower circuit. This circuit drove the pulse through 50 feet of cable to a DD2 linear amplifier. The amplified signal was analyzed by either a 100-channel "Penco" pulse-height analyzer (Pacific Electro-Nuclear Co., Culver City, Calif.) or a 256-channel "TMC" pulse-height analyzer (Technical Measurements Corp., North Haven, Conn.). The net resolution of this scintillation circuit was about 10% for the γ ray of Cs^{137}.

The NaI crystal, the photomultiplier tube, and the cathode-follower circuit were housed in a cylindrical mu-metal magnetic shield which was, in turn, encased in a 1/2-in. soft iron magnetic shield. This entire assembly was mounted on a laboratory jack which could be adjusted to the desired counting height. This jack rested on a table which could be rolled on the magnet tracks into place around the cryostat within 10 seconds after a demagnetization.

Two counters were used simultaneously, with one ordinarily at 0 deg and the other at 90 deg to the axis of orientation. In addition, the counters were placed at intervals of 15 deg around the crystal by sliding the base of their supporting jacks along a shallow circular trough built onto the surface of the movable table. It was estimated that the counters could be placed with an angular accuracy of ±2 deg.

D. Gamma-Ray Polarimeter System and Its Calibration

The gamma-ray polarimeter apparatus, shown in Fig. 5, consisted of three scintillation detectors mounted in a framework, lead shielding, and a "fast-slow" coincidence circuit. The rule in Fig. 5 is 6 in. long.

A polarimeter has not been described (to my knowledge) in publications since the ones of Metzger and Deutsch[35] in 1950 and of Bishop and Perez y Jorba[38] in 1955. Therefore, this one, especially newer features of it, are here described somewhat fully.

1. Scintillation detectors

Two standard 1×1.5-in. cylindrical NaI(Tl) crystals were used for γ-ray detection. A 1.5×1.5-in. cylindrical anthracene crystal was used for Compton electron detection. This crystal was rubbed free of its powdery surface layer, enclosed in 5-mil bright Al foil (except for one end), and covered with thin black adhesive tape.

All three crystals were optically mounted with resin[41] on RCA 6810A photomultiplier tubes, which were selected from 30 6810A tubes for their low-noise characteristics. An optical resin mounting was used as it provided a rigid mounting (the polarimeter was often moved about the laboratory) while simultaneously providing the optical advantages of mineral oil or petroleum jelly mountings. The 6810A tubes were used because of their fast rise times and high gains, thus utilizing the coincidence circuit to its full potential.

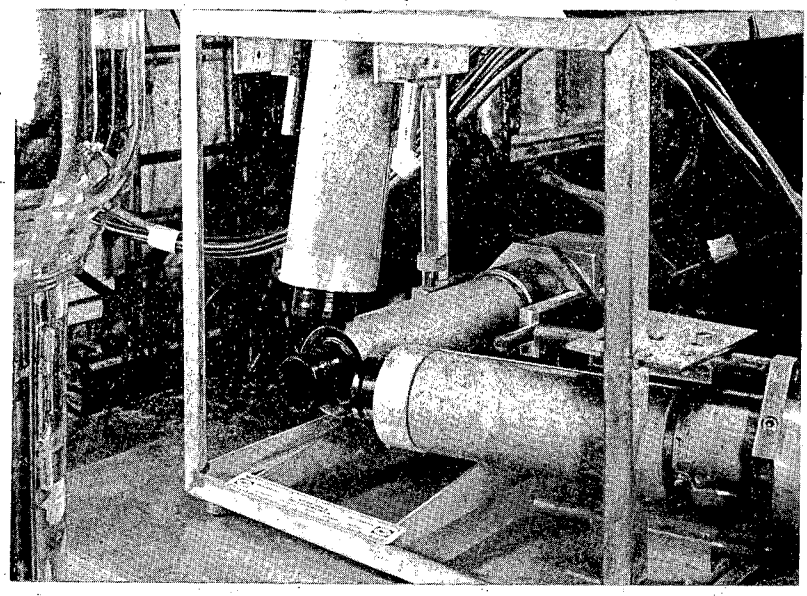

(a)

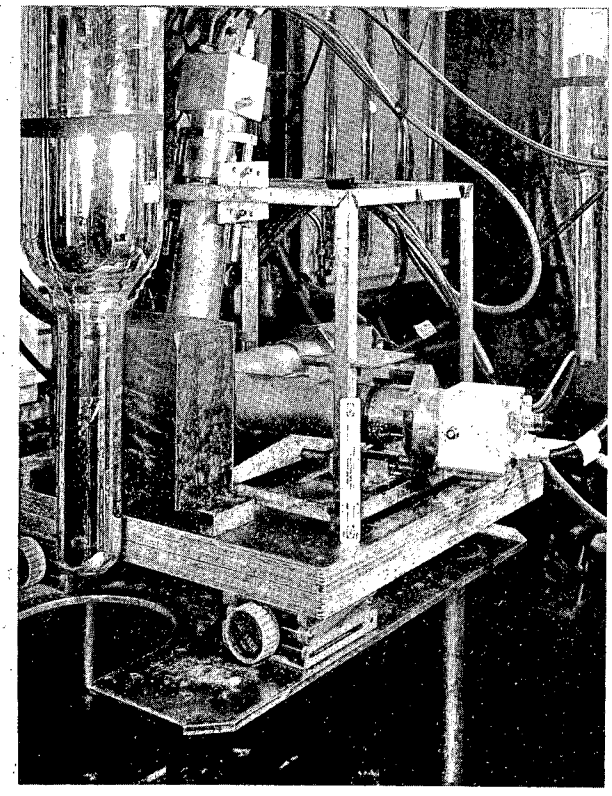

(b)

ZN-2945

Fig. 5. Gamma-ray polarimeter apparatus. The three detectors are shown in (a). The polarimeter in place next to the lead shield and the Dewars is shown in (b).

Each photomultiplier tube, shielded with a mu-metal magnetic shield, was inserted in a brass base, 3x3x3 in. These bases housed a pulse-shaping circuit and were mounted in an 18x18x18-in. open boxlike framework so that the two NaI crystals, mounted at 90 deg to each other, had a projected intersection with the geometric center of the anthracene crystal.

Figure 6 is a diagram of this arrangement. The source, a neodymium ethylsulfate crystal containing the Ce nuclei to be studied, was located inside the crystal chamber and the two Dewars of the orientation system. The polarimeter, mounted on the movable table (see III. C), was rolled up to the Dewars within 15 seconds after a demagnetization so that the 4-in.-thick lead shield just touched the nitrogen Dewar.

The lead shield was bored with a conical hole with dimensions such that a 0.6-in.-diameter source would subtend 1.5 in. at the anthracene-photomultiplier tube interface. The lead served as a shield for direct radiation from the source reaching the NaI crystals. A lead x-ray shield, consisting of 60 mils tin overlaid with 10 mils copper, was secured to the polarimeter side of the lead brick.

The polarimeter could be geometrically adjusted in two ways to give the largest anisotropy in the measurement of the γ rays scattered from the anthracene crystal into the two NaI crystals. The first adjustment possible was the angle δ between the NaI crystal and the direction of propagation of the γ radiation from the source. (The two NaI crystals were always at 90 deg to each other and at the same δ.) For a 0-Mev γ ray, a δ = 90 deg gives the most anisotropic scattering position. For a 1.5-Mev γ ray, a δ = 76 deg gives the most anisotropic scattering position. This is because the cross section for Compton scattering is a function of δ, the angle of scattering.[35] Our polarimeter could be adjusted to an angle of 75, 80, or 85 deg. Since the γ rays studied were all between 0.1 and 1.0 Mev, a setting of δ = 80 deg was used in these experiments.

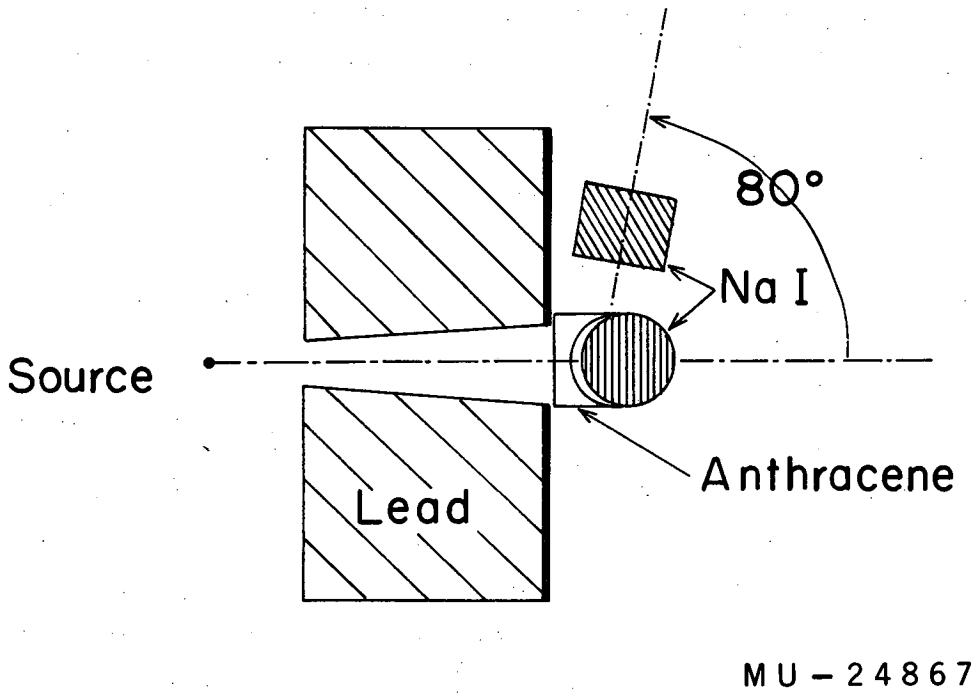

Fig. 6. Diagram of the polarimeter components.

The second adjustment possible was the distance between the front face of each NaI crystal and the geometric center of the anthracene crystal. (This distance was the same for each NaI crystal.) This could be set at increments of 0.25-in. from 1.25 to 2.75 in. The largest distance gives the greatest measured anisotropy and the smallest coincidence counting rate. The optimum of these two opposing conditions was found experimentally to be 1.75 in. for the activities used in these experiments.

The three scintillation detectors, their framework, and the lead shield were mounted on a 24x24x3-in. wooden plane placed on three laboratory jacks. These jacks were adjusted to the appropriate counting height.

The use of the wooden plane, the movable aluminum table on which it rested, the open framework for mounting the three detectors, and only one lead shield proved worth while in that Compton scattering outside the anthracene crystal was held to a minimu, thereby reducing undesirable coincidence counts.

2. "Fast-slow" coincidence circuit

This coincidence circuit[42] performed the coincidence selection in a "fast" circuit with a resolving time of 2×10^{-9} second and the pulse height selection in a "slow" circuit with a resolving time of about 10^{-6} sec. Consequently, the net resolving time was 2×10^{-9} sec. This dual circuit has a decided advantage over those which perform both selections in a single circuit. For, in this case, the variable delay in the output of the pulse-height analyzer limits the resolving time to about 10^{-7} sec.[43]

Figure 7 is a block diagram of the "fast-slow" coincidence circuit used in these experiments. In this diagram, the two NaI circuits are identical, so that only the coincidences between one NaI crystal and the anthracene crystal need be discussed.

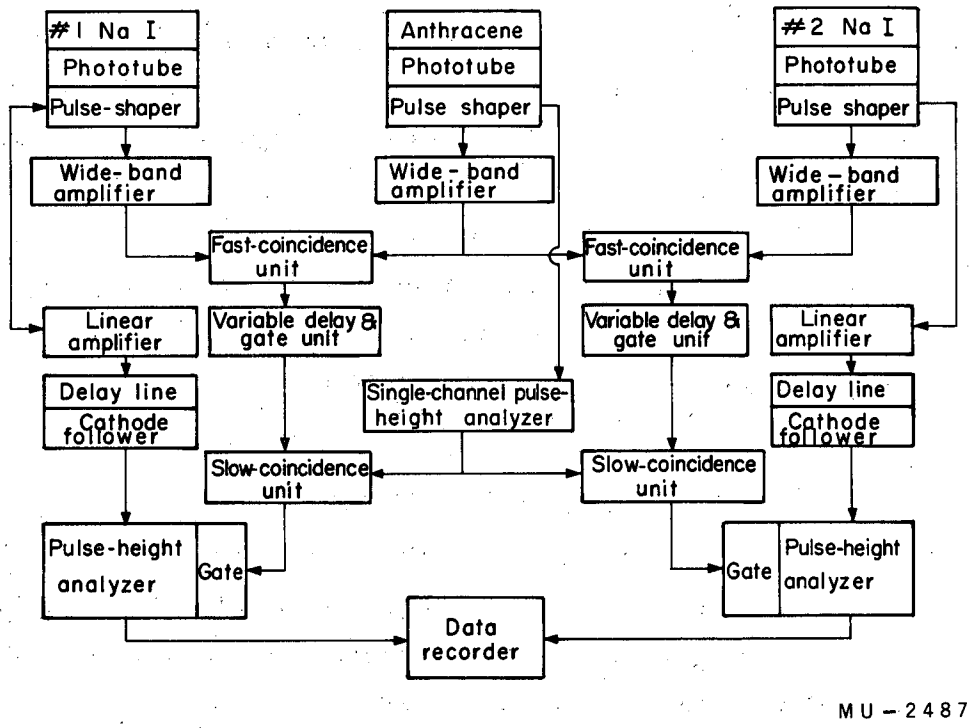

Fig. 7. Diagram of the "fast-slow" coincidence circuit of the polarimeter.

For a coincidence event to be recorded, two conditions had to be met. An event had to occur within the resolving time of the circuit in both the NaI crystal and the anthracene crystal and, in addition, deposit a predetermined amount of energy in the anthracene crystal. All such events were recorded by the data recorder, which was the tape printout of either a 100-channel Penco or a 256-channel TMC pulse-height analyzer.

The third condition for an acceptable event was that the appropriate amount of energy had been deposited in the NaI crystal. The tape printout contained the number of coincidence events as a function of the energy deposited in the NaI crystal. Consequently, only data contained in those channels corresponding to the appropriate energy deposit in the NaI crystal were used in these calculations. The data contained in the other channels corresponded to such events as Compton electron—x-ray coincidences and Compton electron—background—γ-ray coincidences.

The sequence occurring when a desirable coincidence event was achieved is given below. The various electronic units of the circuit, when not identified by the manufacturer's name, are equivalent to units described elsewhere.[44] The coaxial cables used, when not identified by the manufacturer's name, are identified by the United States military specification number.

A γ-ray from the source interacted with the anthrancene crystal and scattered at an angle of 80 deg into the NaI crystal.

a. The pulse produced by the Compton electron in the anthrancene crystal was taken from the 14th dynode of the photomultiplier tube, passed through 50 ft of 125-ohm cable (RG 63/U), amplified by a fast wideband amplifier (Hewlett-Packard Co., Palo Alto, Calif.), and passed through 2 feet of 200-ohm cable (C3T, Transradio Ltd., London) into a two-pentode fast coincidence unit, arriving simultaneously with a similar pulse caused by the scattered γ ray interacting with the NaI crystal. The high voltage for the photomultiplier tubes had previously been set (from 1.7 to 2.0 kv) so that these input pulses were between

3 and 6 volts at this point. Furthermore, a delay curve had been run, and sufficient 125-ohm cable inserted into either the NaI or the anthracene circuit so that the two pulses arrived simultaneously, i.e., within the resolving time of the circuit. The width of this delay curve at half-maximum was twice the resolving time.

The resolving time of our circuit was fixed by inserting a 125-ohm clipping line into the fast-coincidence unit circuit. Although our circuit was capable of a resolving time of 2×10^{-9} sec, a time of 10^{-8} sec was used in this work. This increased the coincidence counting rate by 30% while keeping the chance coincidence events to less than 1% of the true coincidence events.

b. The output of the fast coincidence circuit was put through a variable delay and gate unit where it was delayed about 1μsec until the pulse-height-analyzed pulse from the anthrancene crystal arrived. The variable delay and gate unit consisted of one monostable multivibrator used to delay the input pulse from 0.1 to 10μsec, followed by another multivibrator used to determine the width of the output pulse. This width was set equal to the width at half-maximum of the pulse-height-analyzed pulse.

c. The pulse-height-analyzed pulse was taken from the 10th dynode of the photomultiplier tube. This dynode delivered a pulse proportional to the energy deposited in the anthracene crystal. This pulse was shaped in the photomultiplier tube base to make it acceptable for a DD2 linear amplifier. It was then passed through 10 ft of 125-ohm cable to a Victoreen DD2 linear amplifier and single-channel pulse-height analyzer (Victoreen Instrument Co., Cleveland, Ohio). A Victoreen was selected from among several analyzers as giving the least time "jitter" in its output pulse, i.e., the least variation in the time required for pulse-height analysis. The analyzer then passed only those amplified pulses which were within a preset 10-volt range to a transistorized Rossi-type slow-coincidence circuit.

Here, the pulse-height-analyzed pulse and the variable-delay and gate output pulse produced a coincidence signal which passed through 50 ft of 52-ohm cable (RG 58/U) to the gate of either a Penco or a TMC analyzer.

d. This gate opened the analyzer for several microseconds to receive any pulse from the 10th dynode of the NaI photomultiplier tube. This pulse had been shaped, linearly amplified (but not pulse-height analyzed) by the Victoreen, delayed for 1.2μsec with 14 ft of 2000-ohm cable (RG 176/U), and driven by a cathode-follower circuit through 50 ft of 93-ohm cable (RG 62/U) to the signal input of either a Penco or a TMC analyzer. Then the analyzer recorded the over-all coincidence event in the channel corresponding to the energy of the NaI pulse. The results were calculated from this final record.

Throughout the coincidence circuit, all coaxial cables were properly terminated with resistors so that pulse reflections, of especial importance in the 50-ft cables, were essentially eliminated. All power supplies, the high-voltage supply, and the ac line voltage were regulated.

The gain of the linear amplifier in the NaI circuit was set so that those pulses corresponding to the absorbtion in the NaI crystal of an 80-deg-scattered γ ray were recorded in the center channel of the final pulse-height analyzer. The gain of the linear amplifier in the anthracene circuit was set so that those pulses passed through the 10-volt window width produced a maximum coincidence rate in the center channels mentioned above.

The over-all performance of this "fast-slow" coincidence circuit is indicated by the spectra in Fig. 8. With the use of a point source of Ce^{141} with its single γ ray of 142 kev, the anthracene pulse-height-analyzed spectrum in (a) was recorded. The high-intensity portion of the curve corresponds to Compton electrons produced by the high-probability forward scattering of γ rays in the anthracene crystal. The low-intensity portion of the curve is due to low-probability backward scattering of γ rays. Between the dashed lines is the 10-volt range

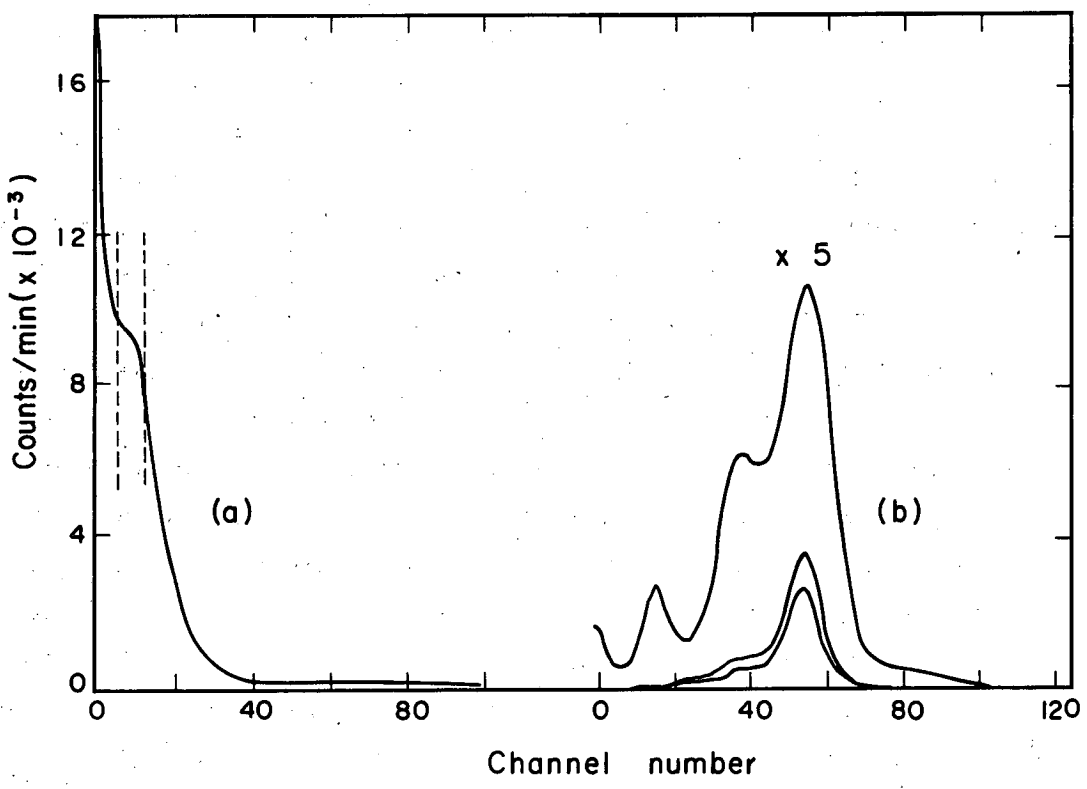

Fig. 8. Pulse-height spectra for Ce^{141}. The β spectrum recorded by the anthracene crystal is shown in (a). The γ-ray spectra recorded by one NaI crystal are shown in (b).

corresponding to Compton electrons with an average energy of 25 kev. These were produced by 80-deg scattering of the 142-kev γ ray in the antracene crystal.

The three curves in (b) are the final recorded coincidence events as a function of energy deposited in one of the two NaI crystal. Each curve, the intensity of which is multiplied by 5, represents a different resolving time. The upper curve corresponds to a resolving time of 10^{-6} sec. The main peak is 117 kev and corresponds to an 80-deg scattered γ ray. The shoulder of this peak represents some undesirable coincidence events, such as between a Compton electron and a lead x ray. The low-intensity peak represents events such as between a Compton electron and an iodine x-ray.

The lowest curve in (b) corresponds to a resolving time of 2×10^{-9} sec. Only the 117-kev peak and its Compton distribution are now present. The center curve corresponds to a resolving time of 10^{-8} sec. This setting was used in these experiments as it gave a higher coincidence rate and the same spectrum as with the shortest resolving time. These three curves are uncorrected for random coincidence counts.

In each experiment, the number of random coincidence events was measured by inserting a delay line corresponding to 2×10^{-7} sec in the anthracene side of the "fast" coincidence circuit. In all cases, the random events were less than 1% of the true events, therefore no correction was necessary, as this 1% was well within the statistical error of the measurements.

3. Calibration of the polarimeter

The geometry correction factor R, a function of the energy of the quanta impinging on the anthracene crystal, was measured for our polarimeter at one energy by using a 0.5-curie source of Co^{60}.

The Co^{60} source was collimated with uranium shielding to a beam of 1-in. diameter. A 1×1×1-in. lead cube was placed, in relation

to the polarimeter, where the neodymium ethylsulfate crystal containing the Ce activity was located in an experiment. The 1.1728- and 1.3325-Mev γ rays of Co^{60} traveled 16 in. to the lead cube, where a certain percentage scattered at 90 deg and traveled 5.5 in. to the anthracene crystal of the polarimeter. These 90-deg-scattered quanta with an average energy of 0.363 Mev were thus plane-polarized owing to the scattering and had a calculated average p for the two γ rays of

$$\overline{p} = \frac{2.06 + 2.25}{2} = 2.15.$$

Four 1-hour-duration measurements of $N = N_{\parallel}/N_{\perp}$ gave $N = 1.43$, 1.38, 1.38, and 1.47 (assuming that the scattered quanta from each of the two γ rays were counted with the same efficiency), for an average N of

$$\overline{N} = 1.42 \pm .05.$$

Two of the four measurements were made with the polarimeter in a normal position, and two were made with the entire polarimeter physically rotated 90 deg around the axis of the anthracene crystal. This was necessary to normalize out the slight difference in overall coincidence counting efficiency of the two NaI counters and coincidence circuits.

Substituting $\overline{p}$ and $\overline{N}$ in Eq. (II-14) gave the value

$$R = 2.8^{+0.4}_{-0.3}$$

for an average a_0 of

$$\overline{a}_0 = \frac{0.697 + 0.723}{2} = 0.710.$$

Now, by use of this value of R for $a_0 = 0.710$, the angular spread of our polarimeter was calculated. Then, R for all other values of a_0 was calculated. This was done by using the following procedure.

The Klein-Nishina Compton-scattering cross section may be written in terms of a to give

$$\frac{d\sigma(\eta)}{da} = \frac{\pi r_0^2}{a_0^2}\left(\frac{2}{a_0} - \frac{2}{a} + \frac{1}{a_0^2} + \frac{1}{a^2} - \frac{2}{a_0 a} + \frac{a_0}{a} + \frac{a}{a_0}\right),$$

where the symbols are defined in Part II. D. The integral equation from this is

$$\sigma = \frac{2\pi r_0^2}{a_0^2}\left\{\left[\Delta a\left(\frac{2a_0+1}{a_0^2} + \frac{1}{a_i a_f}\right) - \frac{2(1+a_0)}{a_0}\ln\frac{a_f}{a_i}\right]\left[\frac{1}{2}\Delta\eta + \frac{1}{2}\cos(\eta_i+\eta_f)\sin(\eta_f-\eta_i)\right] + \Delta\eta\left[\frac{a_0}{2}\ln\frac{a_f}{a_i} + \frac{1}{4a_0}\left(a_f^2 - a_i^2\right)\right]\right\},$$

where $\Delta a = a_f - a_i$, $\Delta\eta = \eta_f - \eta_i$, a_f and η_f are the upper limits of integration and a_i and η_i are the lower limits of integration.

R may then be expressed as

$$R = \int_{a_i}^{a_f}\int_{\eta_i + 90^\circ}^{\eta_f + 90^\circ} d\sigma(\eta) \Big/ \int_{a_i}^{a_f}\int_{\eta_i}^{\eta_f} d\sigma(\eta).$$

With the values R = 2.5, 2.8, and 3.2, this equation was solved, yielding $\Delta\delta = \Delta\eta = 70 \pm 7$ deg.

This result compared quite well to one geometrically calculated from the dimensions of our polarimeter, assuming that all scattered quanta interacted with the geometric center of the anthracene crystal. This gave $\Delta\delta = \Delta\eta = 66$ deg.

With the value $\Delta\delta = \Delta N = 70 \pm 7$ deg, the three curves in Fig. 9 (a) were calculated. R is plotted as a function of the energy, before scattering, of the initial quantum. The solid line of (a) is for $\delta = 80$ deg, $\Delta\delta = \Delta N = 70$ deg. The two dashed lines are for $\delta = 80$ deg, $\Delta\delta = \Delta N = 63$ deg and $\Delta\delta = \Delta N = 77$ deg.

Curve (b) represents $\delta = 80$ deg and $\Delta\delta = \Delta N = 0$ deg, i.e., a point source, scatterer, and counter.

Figure 10 is a plotted coincidence spectrum at $1.2^{\circ}K$ for one of the alignment experiments on the 0.166-Mev γ ray of Ce^{139}. The coincidences were between the $N_{\parallel}$ NaI counter and the anthracene counter. The counting rate shown was typical for these experiments. The energy of the scattered quanta as recorded in the NaI counter is given as E. The dashed lines are equivalent to $\delta = 45$ deg and $\delta = 115$ deg, the two limits between which the recorded coincidence events were set equal to $N_{\parallel}$. The value for $N_{\perp}$ was obtained from the coincidence events for the $N_{\perp}$ NaI counter. Then the experimentally deduced value of R was taken from Fig. 9(a) and used with $N = N_{\parallel}/N_{\perp}$ to calculate p from Eq. (II-14).

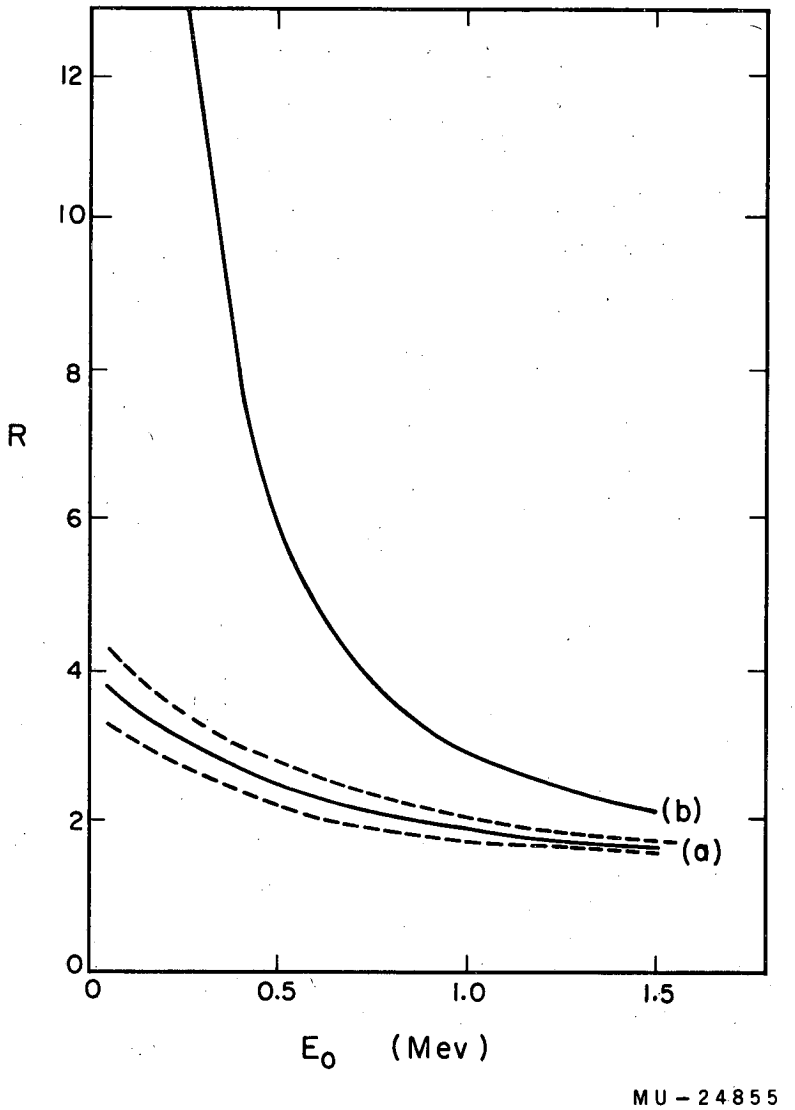

Fig. 9. R versus the initial energy of the γ ray. The solid line of (a) is for δ = 80 deg, $\Delta\delta$ = ΔN = 70 deg. The dashed lines are for δ = 80 deg, $\Delta\delta$ = ΔN = 63 deg, and $\Delta\delta$ = ΔN = 77 deg. The solid line of (b) is for δ = 80 deg, $\Delta\delta$ = ΔN = 0 deg.

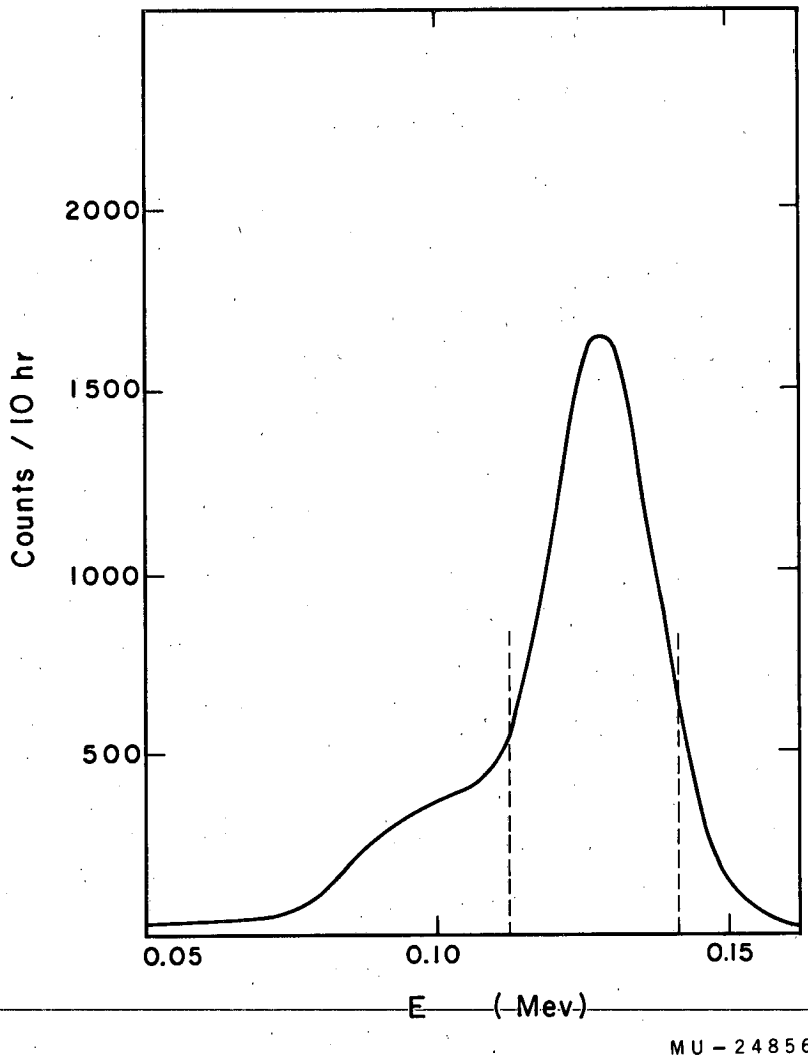

Fig. 10. Gamma-ray pulse-height coincidence spectrum for 166-kev γ ray of Ce^{139}.

IV. SPECIMEN PREPARATION

The nuclear reactions used to produce the various Ce radioisotopes studied in these experiments are given in Table IV.

Table IV. Nuclear reactions for producing Ce radioisotopes

Isotope	Reaction	Target	Target thickness	Bombardment conditions
Ce^{137}	$La^{139}(p, 3n)Ce^{137}$	La metal (natural)	3 mils	Oak Ridge National Laboratory 88-inch cyclotron, 8 hr of 21-Mev protons at 200 μa/hr
Ce^{137m}	$La^{139}(p, 3n)Ce^{137m}$	La metal (natural)	3 mils	
Ce^{139}	$La^{139}(p, n)Ce^{139}$	La metal (natural)	3 mils	
Ce^{141}	$Ce^{140}(n, \gamma)Ce^{141}$	Ce_2O_3 powder (natural)	100 mils	Lawrence Radiation Laboratory, Livermore pool-type reactor, 16 hr of thermal neutrons at 5×10^{13} n/cm^2/sec
Ce^{143}	$Ce^{142}(n, \gamma)Ce^{143}$	CeO_2 powder (90% Ce^{142})	100 mils	

After the target material had been irradiated, it was dissolved in either distilled water or concentrated HNO_3 and the solution was made up to 9 M HNO_3. Then a solvent extraction was performed to obtain the Ce activity.

This extraction consisted of oxidizing the cerium ions to Ce^{+4} with $NaBrO_3$ and then extracting them from the acid solution with methyl isobutyl ketone. Then the Ce^{+4} was reduced to Ce^{+3} with H_2O_2 and extracted from the ketone with H_2O. This final solution was evaporated to dryness, leaving a solid residue of $Ce(NO_3)_3$ and $NaNO_3$. Any rare earths other than Ce present in the original acid solution would be reduced in concentration by a factor of 1000 in this extraction.[45]

This was checked by observing the γ-ray spectra of all the isotopes studied and following their half-lives. No unidentified peaks were observed.

The solid residue of $Ce(NO_3)_3$ and $NaNO_3$ was dissolved in 15 ml of saturated water solution of neodymium ethylsulfate. Previous to the extraction, a neodymium ethylsulfate single crystal of from 8 to 15 g was grown. This was done by dissolving stoichiometric amounts of $Nd_2(SO_4)_3$ and $Ba(C_2H_5SO_4)_2$ in water, filtering out the $BaSO_4$ precipitate, and evaporating the water at room temperature to give a residue of neodymium ethylsulfate crystals. These crystals were redissolved and reprecipitated twice and then used for growing the single crystal used for each experiment.

This single crystal was then placed in the neodymium ethylsulfate solution containing the Ce activity as Ce^{+3} ions. A jet of air was used to slowly evaporate the solution at room temperature. After from 6 to 24 hr, sufficient activity for an experiment (approximately 10^6 to 10^7 disintegrations per minute) would be incorporated into the crystal as $Ce(C_2H_5SO_4)_3 \cdot 9H_2O$. The upper limit on the activity grown into the crystal was that its radioactive self-heating would not warm up the demagnetized crystal from $0.02^{\circ}K$ to $0.05^{\circ}K$ within 1 hour. The lower limit was that the γ-ray counting rate would have a statistical error significantly less than the observed anisotropy.

After the activity was incorporated into the crystal, it was removed from the active solution and dried with absorbent paper towels. It was then placed in an additional 15 ml of saturated neodymium ethylsulfate solution for about 12 hr, and a layer of neodymium ethylsulfate was grown onto it under the conditions mentioned above. This layer was grown so that the Ce nuclei would be located somewhat on the interior of the crystal and not in the surface layer with its consequent higher temperatures following a demagnetization.

The net yield of this process was from 10 to 50% of the Ce activity incorporated into the crystal. In addition, measurements

showed that the ratio of Ce to Nd ions in the active portion of the crystal was less than 1 per 1000. This insured that the Ce ions would not interact with one another and thereby introduce another factor into the interpretation of the experimental results.

V. EXPERIMENTAL PROCEDURE

After the specimen was prepared as described in Part IV, the crystal was mounted in its glass framework and attached below the salt pill on the apparatus. The glass crystal chamber was then placed around the crystal and soft-soldered into place. Then a colloidal dispersion of graphite in water was painted on the exterior of the chamber. When dry, this left a thin, even layer of graphite which served as a blackbody absorber for radiation impinging on the crystal chamber.

Next, the mutual inductance coils were placed around the crystal chamber and held in place by a strip of 1-mil Mylar tape. Care was taken to place the coils so that the salt pill was exactly the same distance from each of the two secondary coils. This was done so that the salt pill's susceptibility would not contribute to the readings taken of the neodymium ethylsulfate's susceptibility. (Susceptibility measurements taken with only the salt pill in place proved this to be the case.)

The liquid nitrogen Dewar was next placed around the crystal chamber, which was then pumped for about 12 hr. This length of time permitted the surfaces of the crystal chamber to degas to a considerable extent and insured a constant vacuum of about 5×10^{-6} mm Hg (as indicated by gauge F in Fig. 2(a)).

After the 12 hr had elapsed, the nitrogen Dewar was removed and the helium Dewar (precooled with liquid nitrogen) bolted into place. Before each experiment, the vacuum space of the helium Dewar was re-evacuated, as liquid helium during previous experiments would slowly diffuse through the glass walls into the vacuum space.

The nitrogen Dewar was then put up around the helium Dewar. Helium exchange gas was introduced into the crystal chamber at a pressure of about 5×10^{-2} mm Hg (as indicated by gauge F). Then liquid helium was transferred into the helium Dewar, through a double-walled (evaculated) stainless steel transfer tube, from a 25-liter storage Dewar. It took from 15 to 30 min to fill the Dewar with 2 liters of helium.

Susceptibility readings were taken until a constant value as a function of time was measured, i.e., until the crystal had equilibrated with the liquid helium at 4.2°K. This took from 15 to 30 min. The liquid helium system was then closed off from the atmosphere and slowly pumped down to about 1 mm Hg. From 10 to 20 susceptibility readings were taken at various pressures (as indicated by a Hg manometer from 760 mm Hg down to 60 mm Hg, and by an oil manometer from 60 mm Hg down to 1 mm Hg) as the temperature of the helium bath was slowly lowered. A straight-line Curie plot of χ versus $1/T$ was obtained in every experiment done. The 1958 He^4 scale of vapor pressure versus temperature[46] was used in making this plot. This calibration took from 1 to 2 hr.

After the lowest temperature possible with our liquid helium pumping system (1.1 to 1.3°K) had been reached, the magnet was rolled into place around the crystal chamber and the crystal was magnetized with the desired field. The crystal chamber was now opened to its vacuum system and pumped down to 5×10^{-6} mm Hg, thus thermally isolating the crystal. This took from 15 to 30 min.

Next, the crystal was demagnetized by slowly turning the magnet field current off over a period of 100 sec in order to achieve a reversible process. The magnet was then rolled away, the γ-ray counters (or the polarimeter) were rolled into place, and a "cold" count was started. Susceptibility readings were taken throughout the counting period, which varied from 1 to 10 min (depending on the activity of the Ce) for the NaI(Tl) counters and from 10 to 20 min for the polarimeter.

After the count at the low temperature was taken, helium exchange gas was introduced into the crystal chamber at a pressure of 5×10^{-2} mm Hg. The crystal, as indicated by the susceptibility readings, warmed up to the helium-bath temperature in from 10 to 60 sec. Then, without moving the counters, a "warm" count at 1.2°K was taken for the same duration as the cold count.

For each of the 5 Ce isotopes studied, approximately 40 pairs of cold and warm counts were taken with the γ-ray counters and the polarimeter at temperatures ranging from 1^{o}K to 0.02^{o}K (none of the isotopes studied had a γ-ray anisotropy that could be detected at 1^{o}K) and with the γ-ray counters at angles in intervals of 15 deg from 0 to 120 deg at a temperature of 0.02^{o}K.

Ordinarily, for each pair of warm and cold counts, a separate demagnetization was performed. In some cases, where the warmup rate was considerably slower, the crystal was demagnetized to its lowest temperature of about 0.02^{o}K and consecutive 1- to 20-min counts (depending on the activity of the Ce) were taken as the crystal slowly warmed up over a period of hours. Then, several warm counts at 1.2^{o}K were taken for the same counting interval. These data always yielded the same results as the data from demagnetizations in which only one pair of counts was taken. This is to be expected where the T change as a function of time is small.

VI. EXPERIMENTAL RESULTS

A. General Comments

For each Ce isotope aligned, a figure is given showing the following.

1. The decay scheme used in interpreting the experimental results,
2. γ-ray pulse-height spectra at $1/T = 50$ and $1/T = 1$,
3. Experimental values of $I(0^\circ)$ versus $1/T$,
4. Experimental values of $I(\theta)$ versus θ at $1/T = 50$,
5. Experimental values of p versus $1/T$,
6. Experimentally derived value of δ versus F'_2 and F''_2.

These sets of six figures for each of the five Ce isotopes have some factors in common, therefore comments on these factors are given here rather than being repeated five times.

1. Decay scheme. This was based, when possible, directly on published spectroscopic results such as summarized in the 1958 Table of Isotopes.[47] When no data were available in the literature, the decay scheme was assigned by using published spectroscopic results on the appropriate neighboring nuclei. Nuclear systematics in this region of nuclei indicate that this method is particularly useful in assigning ground-state angular momenta.

2. Gamma-ray spectra. The solid line refers to the spectrum recorded at $1/T = 1$. The dashed line refers to the spectrum at $1/T = 50$. These spectra were usually taken with the 3x3-in. NaI crystal at a distance of 10 cm from the source.

3. $I(0^\circ)$ vs $1/T$ values. The statistical counting error in the measurement of $I(0^\circ)$ includes both warm and cold counting errors. It is indicated by the vertical line, and was approximately the same for all points on a particular isotope. When no vertical line is shown, the counting error is less than the diameter of the plotted point.

4. $I(\theta)$ vs θ values. These values were all measured at $1/T = 50$. The values are represented by a circle for the first quadrant (with respect to the c-axis, $\theta = 0^{\circ}$ counter), by a square for the second quadrant, and by a triangle for the fourth quadrant. The vertical line indicates the statistical counting error. The horizontal line indicates the geometrical error in placing the γ-ray counters. This is estimated as ± 2 deg. Except for the Ce^{137m} results, for which an appreciable amount of $P_4(\cos\theta)$ was present in $I(\theta)$, the results were plotted as a function of $P_2(\cos\theta)$. This yields directly a slope equal to $B_2U_2F'_2$, except for a small $P_4(\cos\theta)$ correction when needed.

5. p vs $1/T$ values. Each rectangle represents the average of several measurements, with exceptions mentioned later in this section. The vertical dimension of these rectangles indicates the uncertainty in the measured value of R, the geometry correction factor. The more N deviates from 1, the larger the uncertainty in R. (See II. D and III.D) The horizontal dimension of these rectangles indicates the change in $1/T$ of the aligned Ce nuclei while the 10- to 20-min-long measurement was made.

6. Curves of δ vs F'_2 and F''_2. The solid lines refer to the calculated F'_2 as a function of δ. The dashed lines refer to the calculated F''_2 as a function of δ. In each graph, the upper solid line refers to a $\delta > 0$, and the upper dashed line refers to a $\delta < 0$, with the reverse being true for the lower lines. The two rectangles represent in the horizontal direction the calculated range of δ, based on the experimentally determined ranges of F'_2 and F''_2, indicated by the vertical dimension of the two rectangles. In this graph for Ce^{141} the two rectangles overlap to form a single rectangle.

B. Ce^{137m}

Cerium-137 is one of a large group of nuclides which has an $h_{11/2}$ isomeric state that decays by emission of M4 radiation to a $d_{3/2}$ ground state. Brosi and Ketelle[48] have studied this isomeric transition and the electron-capture decay of the ground state of La^{137} by γ-ray, coincidence, and conversion-electron spectroscopic techniques. Their results lead to the energy-level scheme shown in Fig. 11.

The energy level at 255-kev is in agreement with the systematics of energy-level spacings for M4 transitions. The K-conversion coefficient and the K/L conversion ratio also indicate M4 transition. A $g_{7/2}$ orbital was assigned to the ground state of La^{137} from its observed second-forbidden β decay to Ba^{137} (spin 3/2), and a $d_{5/2}$ state to the first excited state from the M1 character of the 10-kev γ ray. The conversion-electron measurements by Dzhelepov et al.[49] are not in conflict with these assignments. The shell model is in good agreement with these assignments, and further predicts that the 455-kev level is in either a $s_{1/2}$ or a $d_{3/2}$ state.

The γ-ray pulse-height spectrum obtained in this experiment is shown in Fig. 12. The peaks are due to the 255-kev isomeric transition of Ce^{137m}, the 445-kev γ ray of La^{137}, and the 166-kev γ ray of La^{139} (from the decay of Ce^{139}, which was present as an impurity). The peaks are clearly resolved and no other peaks were observed.

The anisotropy $\epsilon = 1 - I(0^\circ)/I(90^\circ)$, calculated from the experimental $I(0^\circ)$, of the 255-kev γ ray of Ce^{137m} as a function of $1/T$ is shown in Fig. 13. The intensity $I(\theta)$ as a function of θ at $1/T = 50$ is shown in Fig. 14. This angular distribution, expressed in Legendre polynomials, was found to be

$$I(\theta) = 1 - (0.70\pm0.06)P_2(\cos\theta) + (0.05\pm0.01)P_4(\cos\theta). \qquad \text{(VI-1)}$$

For the 255-kev isomeric transition in Ce^{137m}, there are no unobserved preceding transitions, and $U_2 = U_4 = 1$. Assuming for the moment $\delta = 0$, i.e., that the transition is pure M4, Eq. (II-3) becomes,

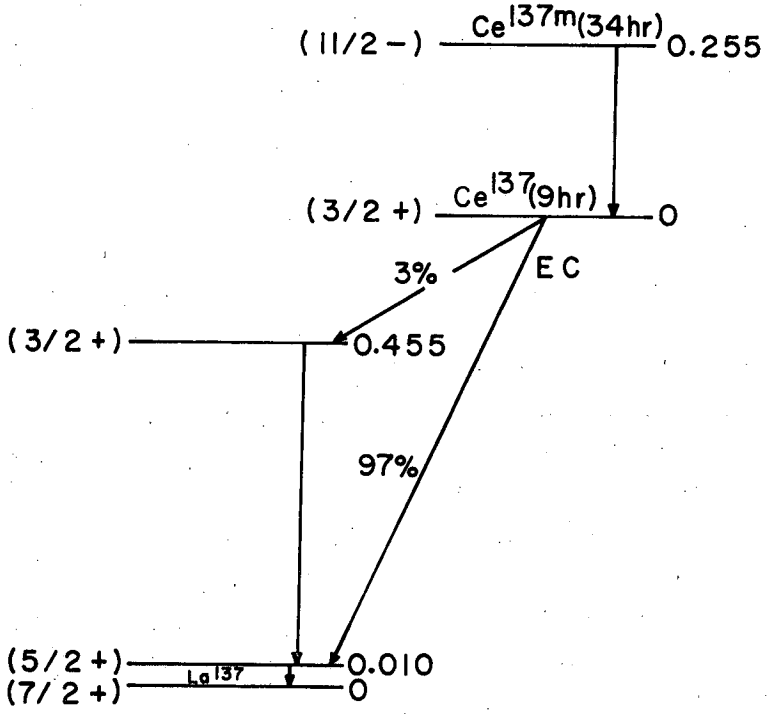

Fig. 11. Energy-level scheme.

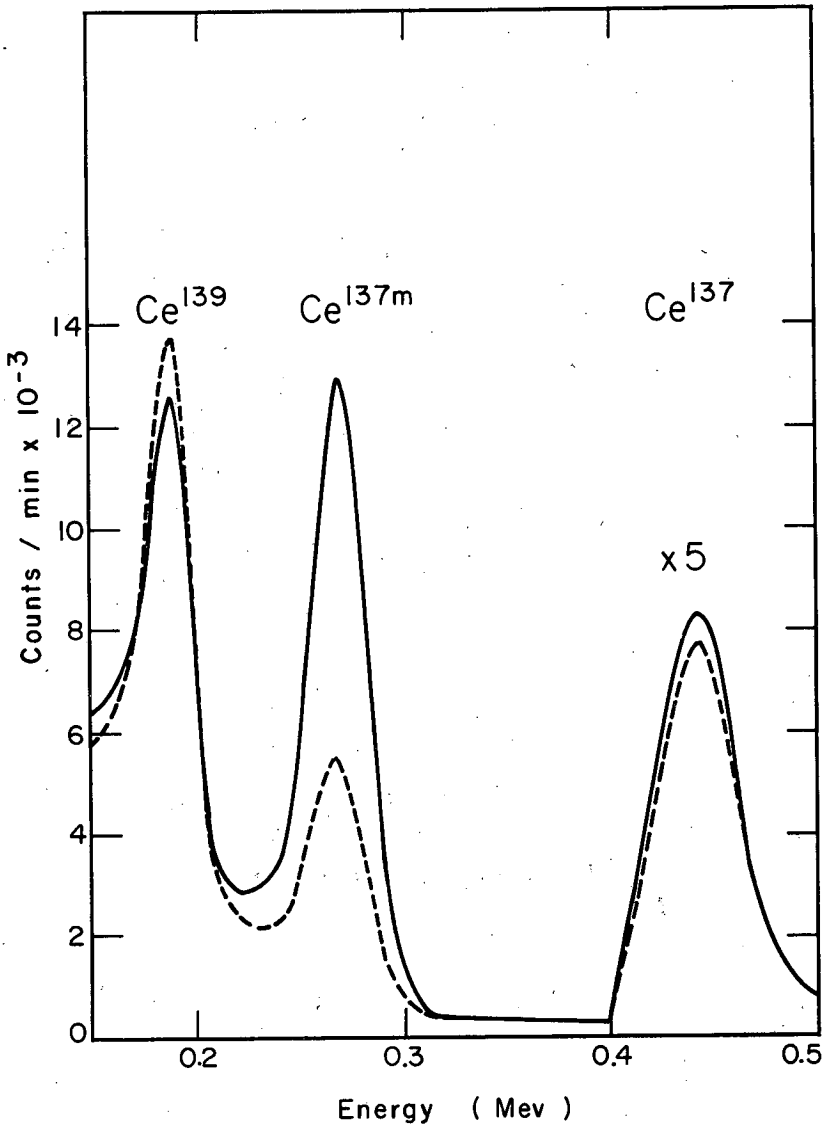

Fig. 12. Gamma-ray pulse-height spectrum at 1.1°K (solid line) and at 0.02°K (dashed line). Measurement made at θ = 0 deg.

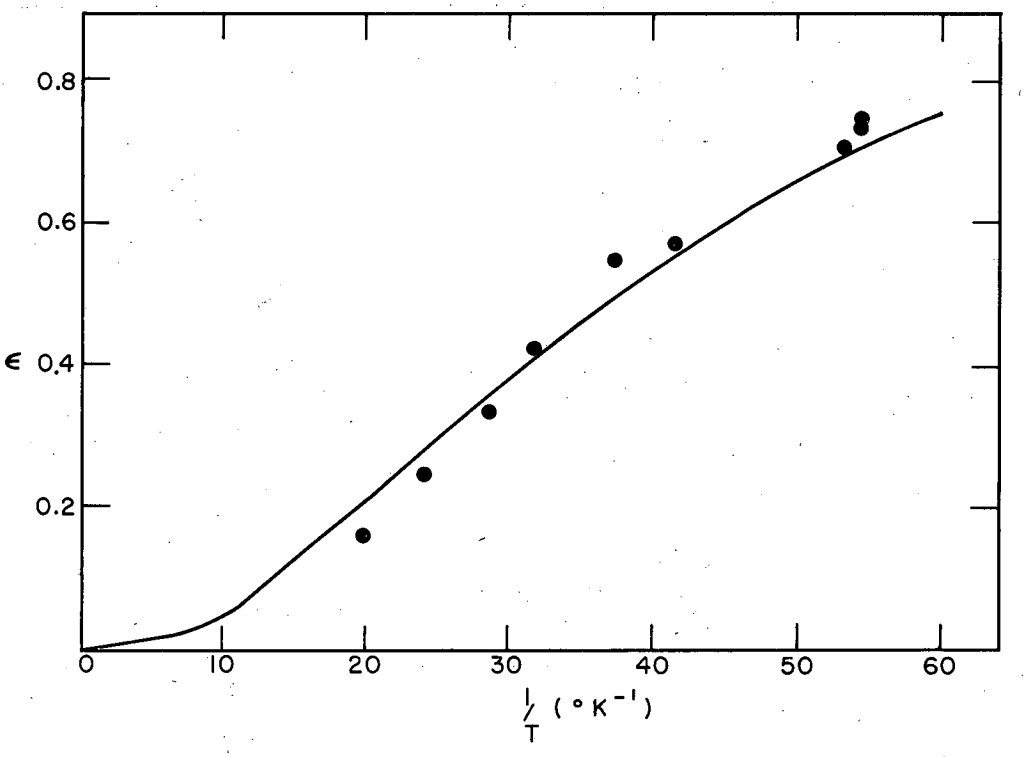

Fig. 13. Experimental values of ϵ and the corresponding theoretical fit for $|\mu_N| = 0.96$ nm.

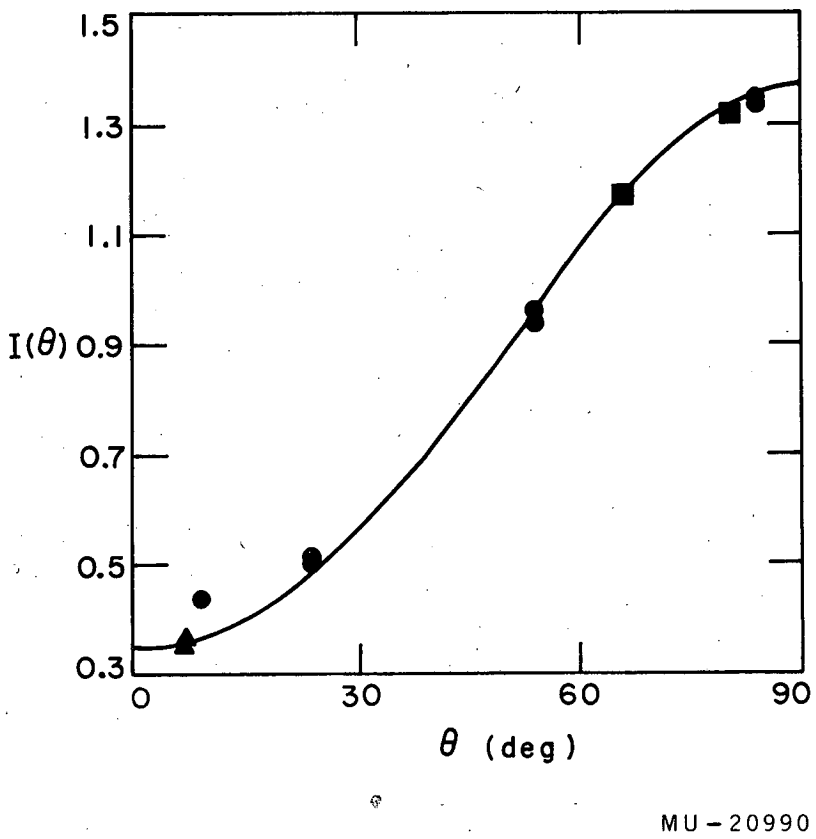

Fig. 14. Angular distribution of the 255-kev γ ray at 0.02°K. The line corresponds to $I(\theta) = 1 - 0.70\ P_2(\cos\theta) + 0.05\ P_4(\cos\theta)$.

for the spin sequence $11/2 \xrightarrow{M4} 3/2$,

$$I(\theta) = 1 - 0.8890\, B_2 P_2(\cos\theta) + 0.4434 B_4 P_4(\cos\theta),$$

and, for the spin sequence $9/2 \xrightarrow{M4} 3/2$,

$$I(\theta) = 1 - 0.7444 B_2 P_2(\cos\theta) + 0.1693 B_4 P_4(\cos\theta).$$

The functions B_2 and B_4 depend on the single parameter $\beta = A/(2kT)$, and by varying A it is possible to fit the temperature dependence of the anisotropy for either spin sequence. Using the value of A which best fits the temperature dependence, we have calculated the angular distribution of the 255-kev γ ray at $1/T = 50$ from each of the above expressions. The results are

$$I(\theta) = 1 - 0.65 P_2(\cos\theta) + 0.04 P_4(\cos\theta) \qquad \text{(VI-2)}$$

for $I = 11/2$, and

$$I(\theta) = 1 - 0.60 P_2(\cos\theta) + 0.02 P_4(\cos\theta) \qquad \text{(VI-3)}$$

for $I = 9/2$.

Comparison with Eq. (VI-1) shows that (VI-3) is in disagreement with it. Thus the spin possibility of $9/2$ is eliminated for Ce^{137m}. We are not aware of any direct measurements of the spin of $11/2$ for the $h_{11/2} - d_{3/2}$ isomers. The spin $3/2$ has been measured for the ground state of the $Ba^{135m} - Ba^{135}$ isomer. However, it has not previously been shown that the isomeric state could not be a $h_{9/2}$ orbital or a $(h_{11/2})^3_{9/2}$ configuration. Therefore this measurement on Ce^{137m} offers the most direct evidence available for the spin assignment of $11/2$ to the isomeric state.

The value of B_2 and B_4 obtained from Eq. (VI-2) gives a value $\beta T = |A|/(2k) = 0.00927\ ^{\circ}K$. Substituting this value into Eq. (II-10) gives

$$|\mu_N| = 0.96 \pm 0.09 \text{ nm}.$$

The limits of error were obtained from the scatter of the experimental points.

After the above results for $|\mu_N|$ had been published,[50] it was felt worth while to check the reasonable assumption that the 255-kev γ ray of Ce^{137m} was a pure M4 transition. The polarimeter described in Part III. D was built and calibrated, and then used to measure the plane polarization of the 255-kev gamma ray.

For the spin sequence $11/2 \xrightarrow{M4} 3/2$, $\delta = 0$, therefore $F_2''(4, 3/2, 11/2) = -(5/17)F_2(4, 4, 3/2, 11/2) = -(5/17)(-0.8890)$ and $F_4''(4, 3/2, 11/2) = -(1/9)F_4(4, 4, 3/2, 11/2) = -(1/9)\,0.4434$. As a result, Eq. (II-4) becomes

$$p = \frac{1 - 1.229B_2 - 0.5358B_4}{1 - 0.3399B_2 - 0.2032B_4}$$

Figure 15 shows 29 experimental values of p plotted as a function of their average $1/T$. (The change in $1/T$ during each measurement was approximately 5 $^{o}K^{-1}$.) The scatter of the values is consistent with the statistical uncertainty of the counting rates involved in the measurements. The two curves were calculated by using the previously determined limits, $|\mu_N| = (0.96 \pm .09)$ and $|\mu_N| = (0.96 - 0.09)$nm to determine B_2 and B_4 as a function of $1/T$.

Figure 16 shows the six values of p obtained by averaging the experimental values of N in each of six temperature ranges. All experimental values of N (which were averaged to give a value for p) were measured over approximately the same temperature range. These results then establish that the 255-kev transition is indeed an M4 transition. Table V shows calculated values of p versus δ(E5/M4) at $1/T = 50$ with $|\mu_N| = 0.96$. A comparison of this table with the experimental values of p in Fig. 16 shows $|\delta|(E5/M4) < 0.7$. This is consistent with photon transition probability calculations[51] for $h_{11/2} - d_{3/2}$ isomers in that these calculation predict $\delta(E5/M4) \approx 0$.

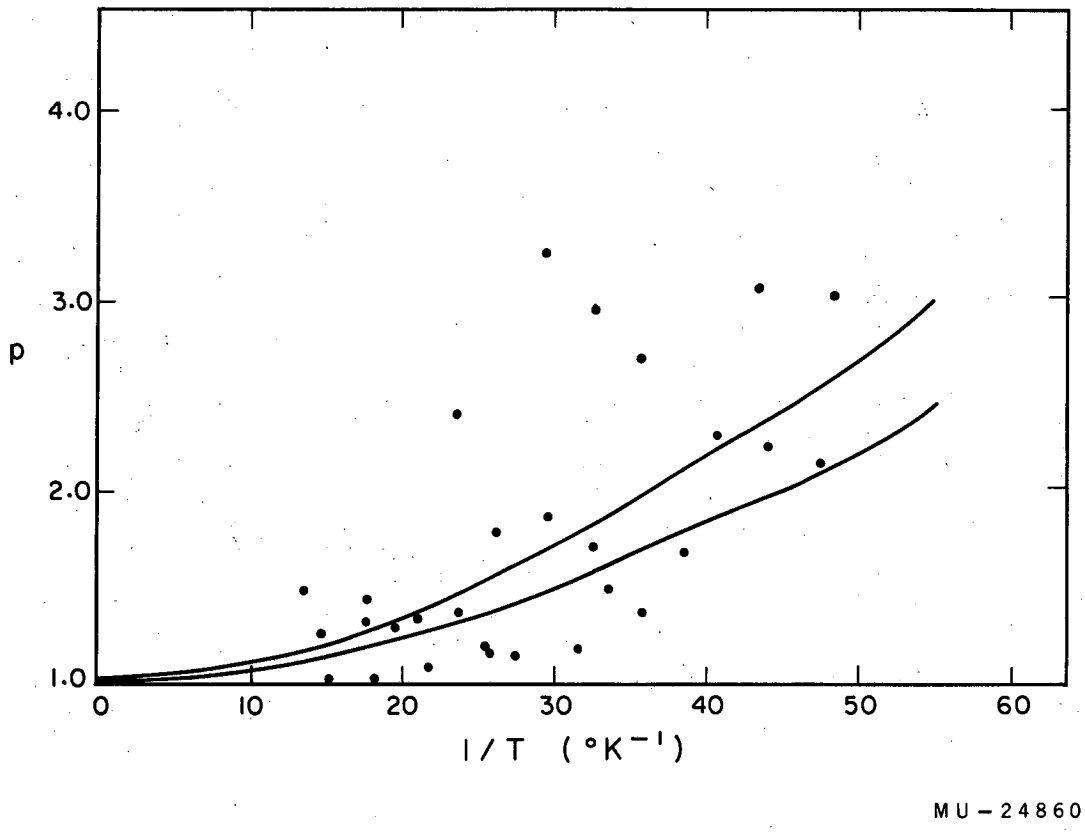

Fig. 15. Experimental values of p before averaging and the corresponding theoretical fits for $\delta = 0$ and $1.05 > |\mu_N| > 0.87$ nm.

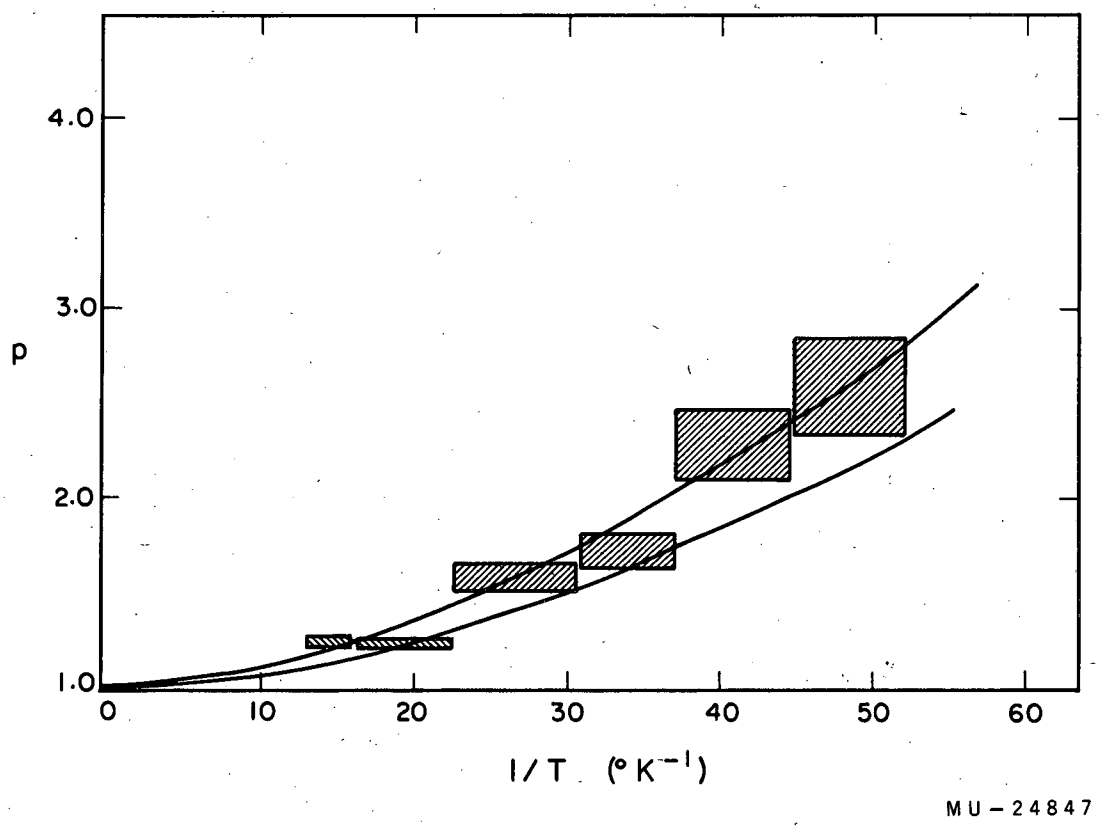

Fig. 16. Experimental values of p after averaging and the corresponding theoretical fits for $\delta = 0$ and $1.05 > |\mu_N| > 0.87$ nm.

Table V. Calculated p vs δ(E5/M4) values at $1/T = 50$ and $|\mu_N| = 0.96$

δ(E5/M4)	p	δ(E5/M4)	p
0.01	2.4	-0.01	2.4
0.02	2.5	-0.02	2.4
0.04	2.5	-0.04	2.4
0.07	2.5	-0.07	2.3
0.10	2.5	-0.10	2.3
0.20	2.5	-0.20	2.1
0.40	2.3	-0.40	1.6
0.70	1.7		

C. Ce^{137}

Since the half life of Ce^{137} (9 hr) is long compared with the nuclear spin-lattice relaxation time, the anisotropy of its γ radiation does not depend on the preceding isomeric transition of Ce^{137m}. A source was prepared with five times the activity of the source used in the Ce^{137m} experiment. The 166-kev γ ray of La^{139} and the 255-kev γ ray of Ce^{137m} were discriminated off the pulse-height analyzer so that only the 445-kev γ ray of La^{137} was counted. This was done to eliminate electronic dead-time changes in the pulse-height analyzer due to the large change in intensity at $\theta = 0$ deg of the 255-kev γ ray between $1/T = 1$ and $1/T = 50$. The experiment was not started until 200 hr after the bombardment to insure that transient equilibrium was present between Ce^{137m} and its Ce^{137} daughter. Therefore, corrections made for decay between the time of making the cold measurement and the time of making the warm measurement (about 8 min) were based on the transient equilibrium half life of 34 hr, the half life of Ce^{137m}.

The intensity $I(0^{\circ})$ of the 445-kev γ ray of La^{137} as a function of $1/T$ is shown in Fig. 17. The intensity $I(\theta)$ as a function of $P_2(\cos\theta)$ at $1/T = 50$ is shown in Fig. 18. This angular distribution was found to be

$$I(\theta) = 1 - (0.060 \pm .010)P_2(\cos\theta) . \qquad \text{(VI-4)}$$

A $P_4(\cos\theta)$ term was not indicated by the data. This term theoretically vanishes if the ground-state spin of Ce^{137} is 3/2.

For the 445-kev transition of La^{137}, the unobserved preceding β transition gives, for the sequence $3/2 \xrightarrow{^1\beta} 3/2$, $U_2 = 1.000$ for a pure $i_\beta = 0$ transition and $U_2 = 0.2000$ for a pure $i_\beta = 1$ β transition. Assuming for the moment $U_2 = 1.000$, one finds that Eq. (II-3) becomes, for the spin sequence $3/2 \xrightarrow{0} 3/2 \xrightarrow{M1, E2} 5/2$,

$$I(\theta) = 1 + F'_2(1, 5/2, 3/2)B_2P_2(\cos\theta) , \qquad \text{(VI-5)}$$

and Eq. (II-4) becomes

$$p = \frac{1 + B_2\left[(-1/2)F'_2(1, 5/2, 3/2) + 3F''_2(1, 5/2, 3/2)\right]}{1 + B_2\left[(-1/2)F'_2(1, 5/2, 3/2) - 3F''_2(1, 5/2, 3/2)\right]} . \qquad \text{(VI-6)}$$

The value of p as a function of $1/T$ is shown in Fig. 19. Although 23 experimental values of N were used in determining p as a function of $1/T$, the statistical uncertainty was such as to give the scatter shown. Even though a large amount of Ce^{137m} was present in the source, only 3% of the resulting Ce^{137} nuclei decayed to the 455-kev level of La^{137}, therefore giving a somewhat low coincidence counting rate. It was not possible to use a much larger amount of Ce^{137}, as it would have too rapidly warmed up the demagnetized neodymium ethylsulfate crystal by radioactive self-heating.

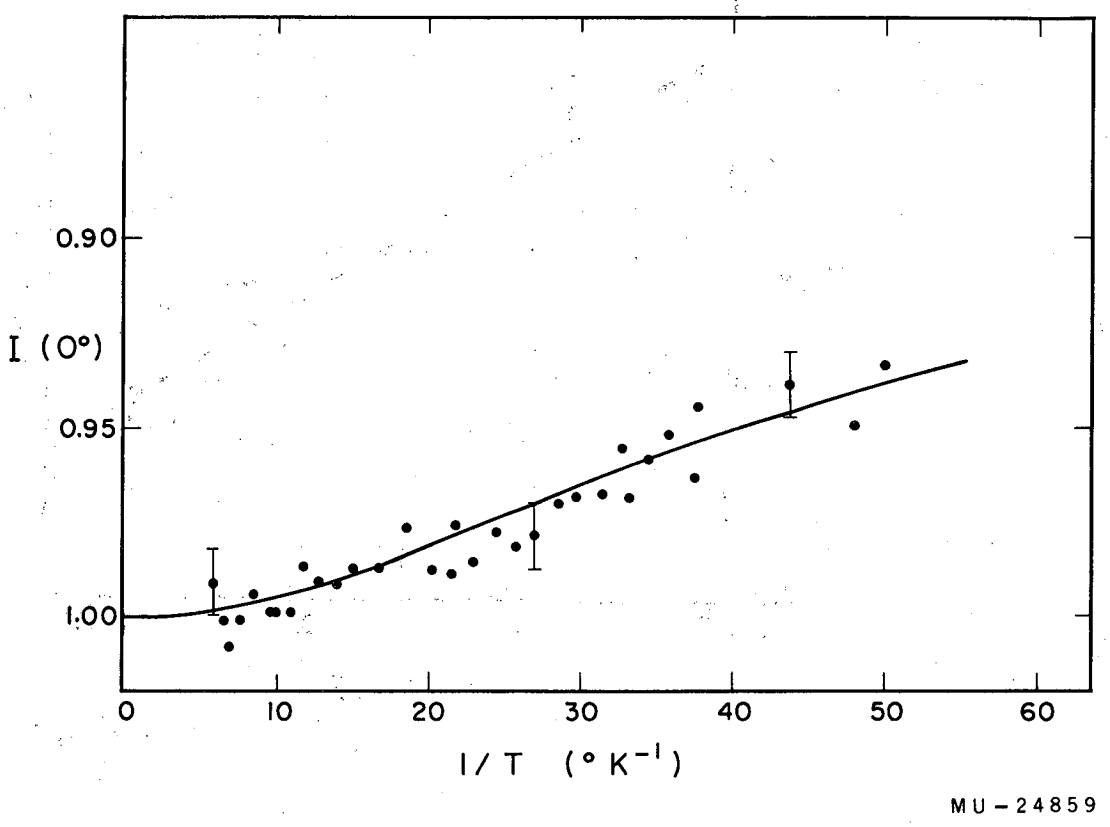

Fig. 17. Experimental values of $I(0^{\circ})$ and the corresponding theoretical fit for $|\mu_N| = 0.95$ nm.

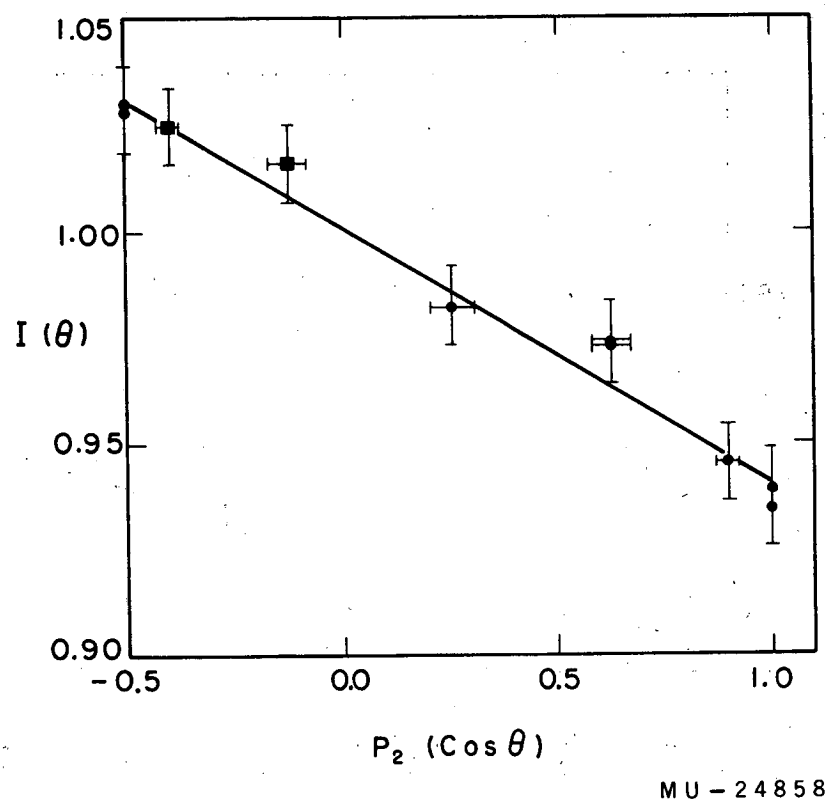

Fig. 18. Angular distribution of the 445-kev γ ray at 0.02°K. The line corresponds to $I(\theta) = 1 - 0.060\ P_2(\cos\theta)$.

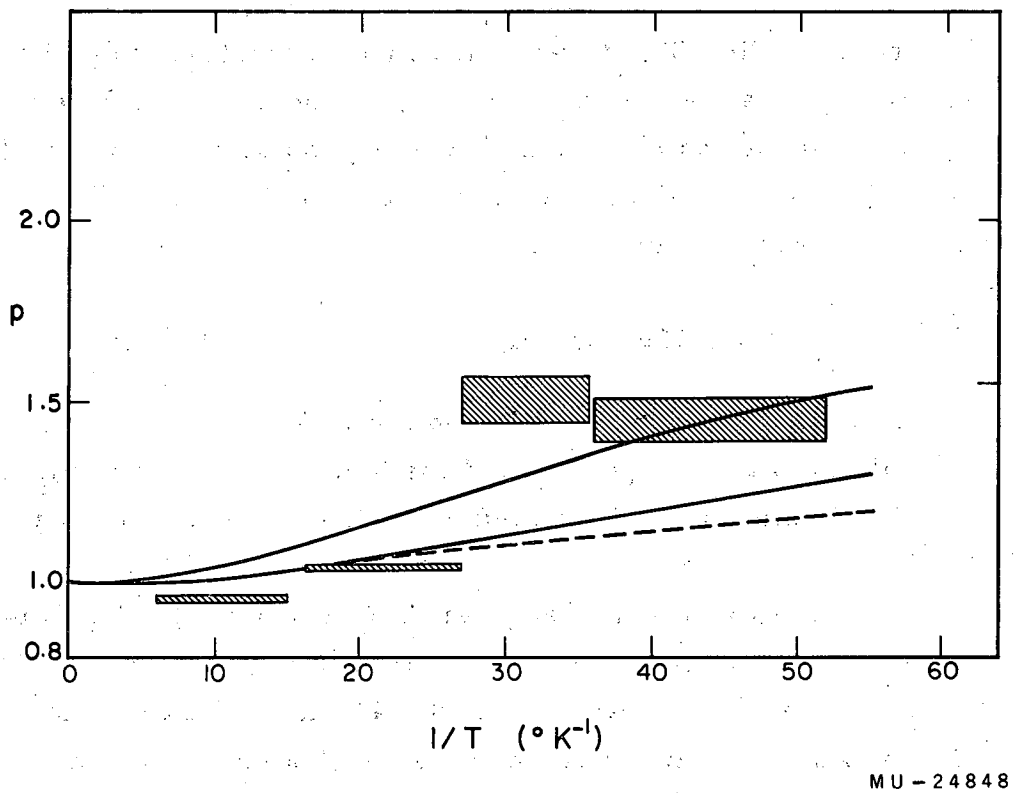

Fig. 19. Experimental values of p and the corresponding theoretical fits for $\delta = -0.17 \pm .02$ and $1.15 > |\mu_N| > 0.75$ nm (solid lines) and for $\delta = -0.7$ and $|\mu_N| = 1.15$ nm (dashed line).

The boundary conditions on δ were found by the technique described in Part II. D. Since at $1/T = 50$ one finds the experimental $I(0^\circ) < 1$, $I(90^\circ) > 1$, and $p > 1$, the A' and B' were evaluated at their algebraic maximum and C' at its minimum to trivially give (since $B_4 = 0$)

$$F_2' < 0 \qquad \text{and} \qquad F_2'' > 0 .$$

By utilizing Fig. 20, it was found that no solution existed for $\delta \geq 0$, and that the range $-0.08 > \delta > -3.5$ included all possible values of δ.

The values of B_2, F_2', and F_2'' obtained from Eq. (VI-5) and (VI-6) which reproduced both the experimental $I(0^\circ)$-vs-$1/T$ and p-vs-$1/T$ curves gave

$$|\mu_N| = 0.95 \pm 0.20 \text{ nm}, \qquad \delta = -0.17 \pm .02 .$$

The limits of error were obtained from both the scatter of the experimental $I(0^\circ)$ and p points and the range over which $|\mu_N|$ and δ could be simultaneously varied and still reproduce the experimental $I(0^\circ)$ and p curves.

The experimental angular distribution $I(\theta)$, Eq. (VI-4), is in complete agreement with these values of $|\mu_N|$ and δ. Furthermore, the measured M1 character of the 445-kev γ ray of La^{137} is consistent with similar transitions for neighboring odd-A near-spherical nuclei.

The above results are based on the assumption that the β transition is pure $i_\beta = 0$. For a pure $i_\beta = 1$ transition, Eq. (VI-5) becomes

$$I(\theta) = 1 + 0.2000 F_2' (1, 5/2, 3/2) B_2 P_2(\cos\theta) ,$$

and Eq. (VI-6) contains $0.2000\, B_2$ in place of B_2. The values of B_2, F_2', and F_2'' obtained then from these two equations could be used to reproduce the experimental $I(0^\circ)$-vs-$1/T$ curve, but consistently

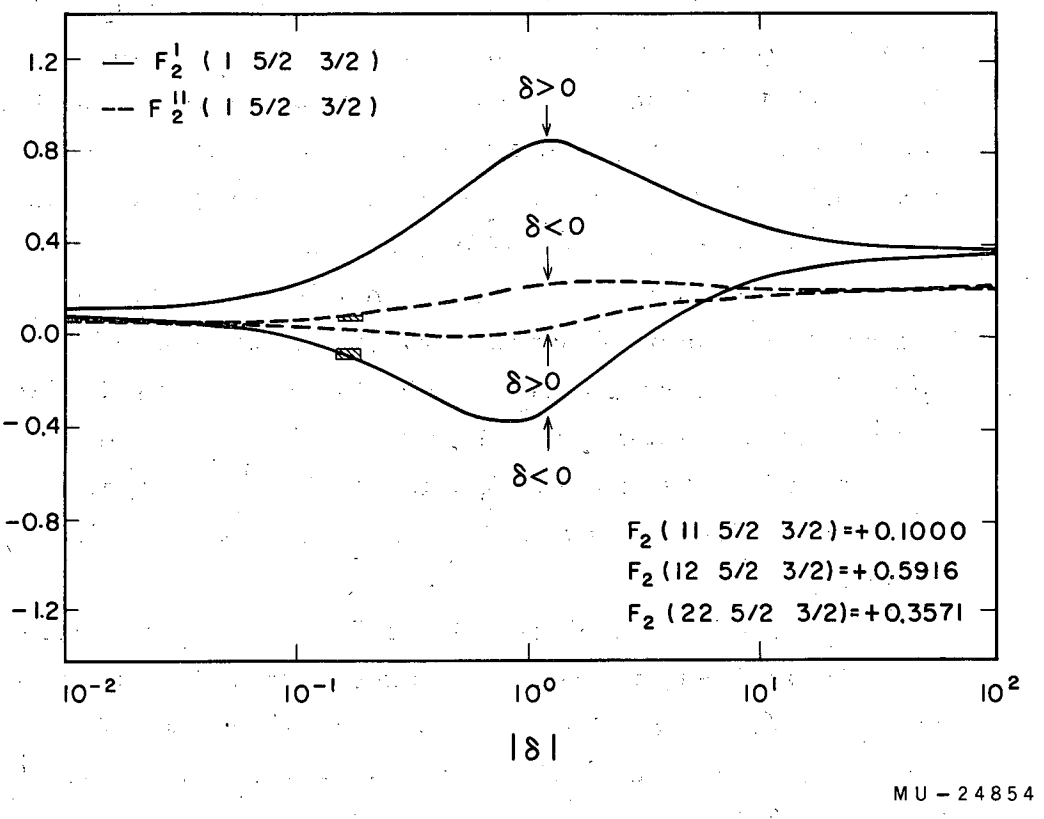

Fig. 20. Calculated F_2^I versus δ curves (solid lines) and F_2^{II} versus δ curves (dashed lines), with the corresponding experimental fit for $-0.15 > \delta > -0.19$.

gave too low a value for the p-vs-1/T curve. The best possible solution for $|\mu_N| \leq$ Schmidt limit (a reasonable assumption for Ce nuclei) gave

$$|\mu_N| = 1.15, \qquad \delta = -0.7 .$$

The theoretical fit for these values is shown in Fig. 19. Even considering the scatter of the experimental p values, the theoretical curve lies well below the low-temperature experimental p values. Consequently, the β transition must be predominantly $i_\beta = 0$ with the possibility of some admixture of $i_\beta = 1$, if the spin sequence $3/2 \xrightarrow{i_\beta} 3/2 \xrightarrow{M1, E2} 5/2$ is correct.

Spin sequences other than the above appear unlikely. Brosi and Ketelle[48] pointed out that the ground state of Ce^{137} might be spin 1/2 (as measured for the M4 isomeric ground state of Xe^{129} and spectroscopically inferred for Ba^{133}). In addition, they indicated the possibility that the 445-kev level of La^{137} might be 1/2. Both these possibilities are definitely ruled out, as the 445-kev γ ray was anisotropic.

The 97% EC decay of Ce^{137} to the first excited state of La^{137} and only 3% decay to the second excited state indicates that the two states probably, although not necessarily, have different spins. Thus, the spin sequences $3/2 \xrightarrow{i_\beta} 3/2 \longrightarrow 3/2$ and $3/2 \xrightarrow{i_\beta} 5/2 \longrightarrow 5/2$ appear unlikely. Furthermore, a $3/2 \xrightarrow{i_\beta} 5/2 \longrightarrow 3/2$ sequence seems improbable for three reasons. Shell-model calculations show that in this region the $d_{5/2}$ orbital should be energetically lower than the $d_{3/2}$ orbital. Secondly, the 455-kev γ ray from the 5/2 second excited state to 7/2 ground state of La^{137} which this spin sequence should exhibit has not been observed. Finally, spectroscopic data on several analogous neighboring nuclei agree with a spin of 5/2 for the first excited state of the daughter of the M4 isomeric ground-state parent.

D. Ce^{139}

The decay schemes of Ce^{139m} and Ce^{139} have been studied by Ketelle, Thomas, and Brosi[52] utilizing γ-ray, coincidence, and conversion-electron spectroscopic techniques. Their results indicate the energy-level scheme shown in Fig. 21.

The energy level at 740-kev agrees with the systematics of energy-level spacings for the $h_{11/2} - d_{3/2}$ M4 transitions.[53] The experimental conversion coefficients for this transition also indicate an M4 transition. The 740-kev γ ray could not be observed with our nuclear orientation system (unless we had assembled it at the beam exit of the Oak Ridge cyclotron) owing to its 55±3-sec half life.

A $g_{7/2}$ orbital was assigned to the ground state of La^{137} on the basis of its measured spin[54] of 7/2. The 166-kev level was assigned a $d_{5/2}$ orbital from the M1 character of its γ ray and from its measured lifetime[55] of $1.5 \pm .1 \times 10^{-9}$ sec. The conversion-electron measurements by Dzhelepov et al.,[49] the Ce^{139m} half-life and energy measurements by Kotajima and Morinaga[56] and the Ba^{139}-to-La^{139} β-transition measurements by Kelly[57] are all consistent with these assignments. The shell model is in complete agreement with these assignments, which are analogous to those for Ce^{137m}, Ce^{137}, and La^{137}.

The source used for this experiment was the same as that for the Ce^{137} experiment. After the source had decayed for 30 days, neither the 255-kev Ce^{137m} activity nor the 445-kev Ce^{137} activity was observable. The resulting γ-ray pulse-height spectrum obtained in this experiment is shown in Fig. 22. Only the 166-kev γ ray of La^{139} was present. The intensity $I(0^\circ)$ of this spectrum has opposite signs for the 166-kev peak and for the Compton distribution around 125 kev. This effect is due to preferential Compton scattering of the plane polarized 166-kev γ ray from the source crystal and the cryostat walls. More is said about this effect in Part VI. E.

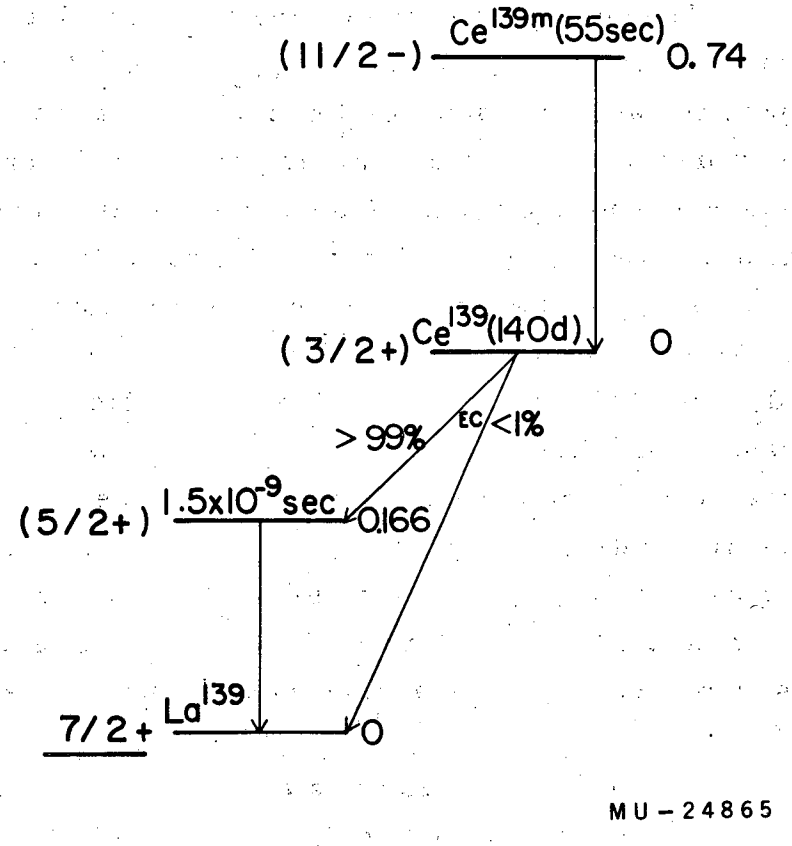

Fig. 21. Energy-level scheme.

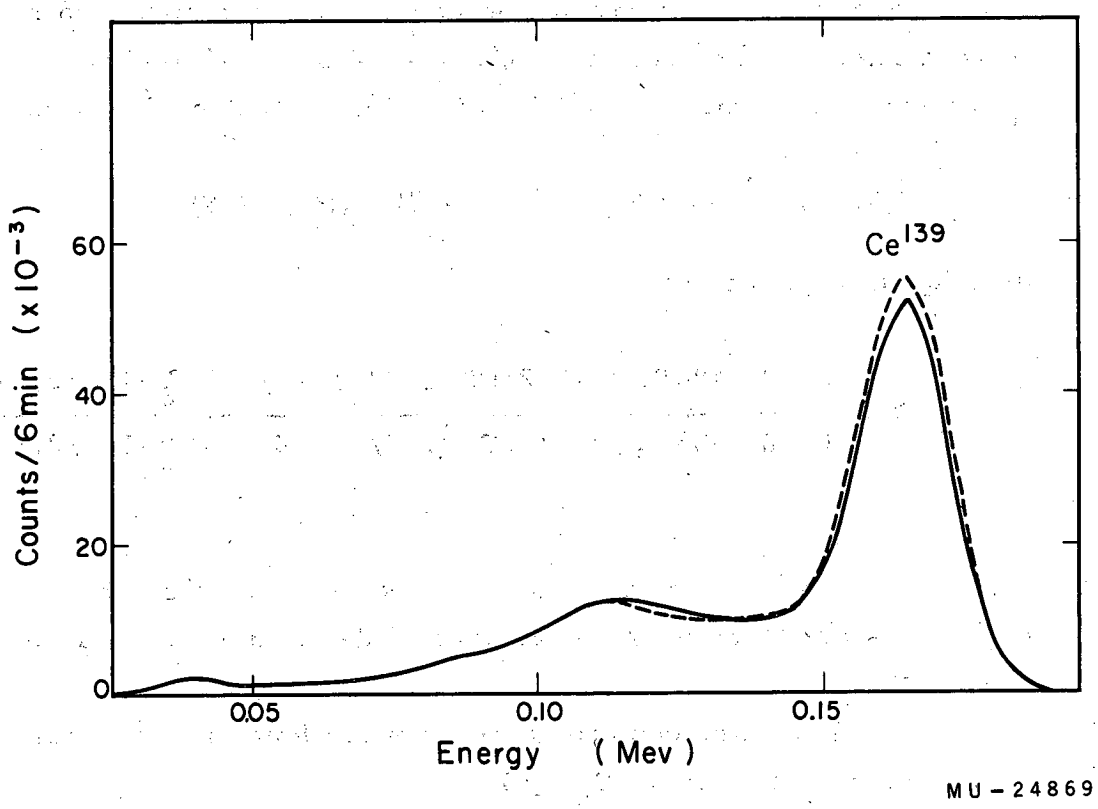

Fig. 22. Gamma-ray pulse-height spectrum at 1.3°K (solid line) and at 0.02°K (dashed line). Measurement at $\theta = 0^{\circ}$.

The intensity $I(0^{\circ})$ of the 166-kev γ ray of La^{139} as a function of $1/T$ is shown in Fig. 23. The intensity $I(\theta)$ as a function of $P_2(\cos\theta)$ at $1/T = 50$ is shown in Fig. 24. This angular distribution was found to be

$$I(\theta) = 1 + (0.080 \pm 0.008)\, P_2(\cos\theta)\,. \qquad \text{(VI-7)}$$

A $P_4(\cos\theta)$ term was not indicated by the data. This term should equal zero if the ground-state spin of Ce^{139} is $3/2$.

For the 166-kev transition of La^{139}, the unobserved preceding β transition for the sequence $3/2 \xrightarrow{i\beta} 5/2 \xrightarrow{M1, E2} 7/2$ cannot be $i_\beta = 0$, therefore for $i_\beta = 1$, $U_2 = 0.7486$. Thus Eq. (II-3) becomes

$$I(\theta) = 1 + 0.7486 F'_2(1, 7/2, 5/2)\, B_2 P_2(\cos\theta)\,, \qquad \text{(VI-8)}$$

and Eq. (II-4) becomes

$$p = \frac{1 + 0.7486 B_2 \left[(-1/2)F''_2(1, 7/2, 5/2) + 3F''_2(1, 7/2, 5/2)\right]}{1 + 0.7486 B_2 \left[(-1/2)F''_2(1, 7/2, 5/2) - 3F''_2(1, 7/2, 5/2)\right]}\,. \qquad \text{(VI-9)}$$

The value of p as a function of $1/T$ is shown in Fig. 25. Nineteen experimental values of N were used to determine p as a function of $1/T$.

The boundary conditions on δ were found as described in part II. D, which gives (since $B_4 = 0$)

$$F''_2 > 0 \qquad \text{and} \qquad F''_2 > 0\,.$$

Utilizing Fig. 26, four ranges for δ were found: $-4 > \delta > -\infty$, $0 > \delta > -0.1$, $0.7 > \delta > 0$, and $\infty > \delta > 1$.

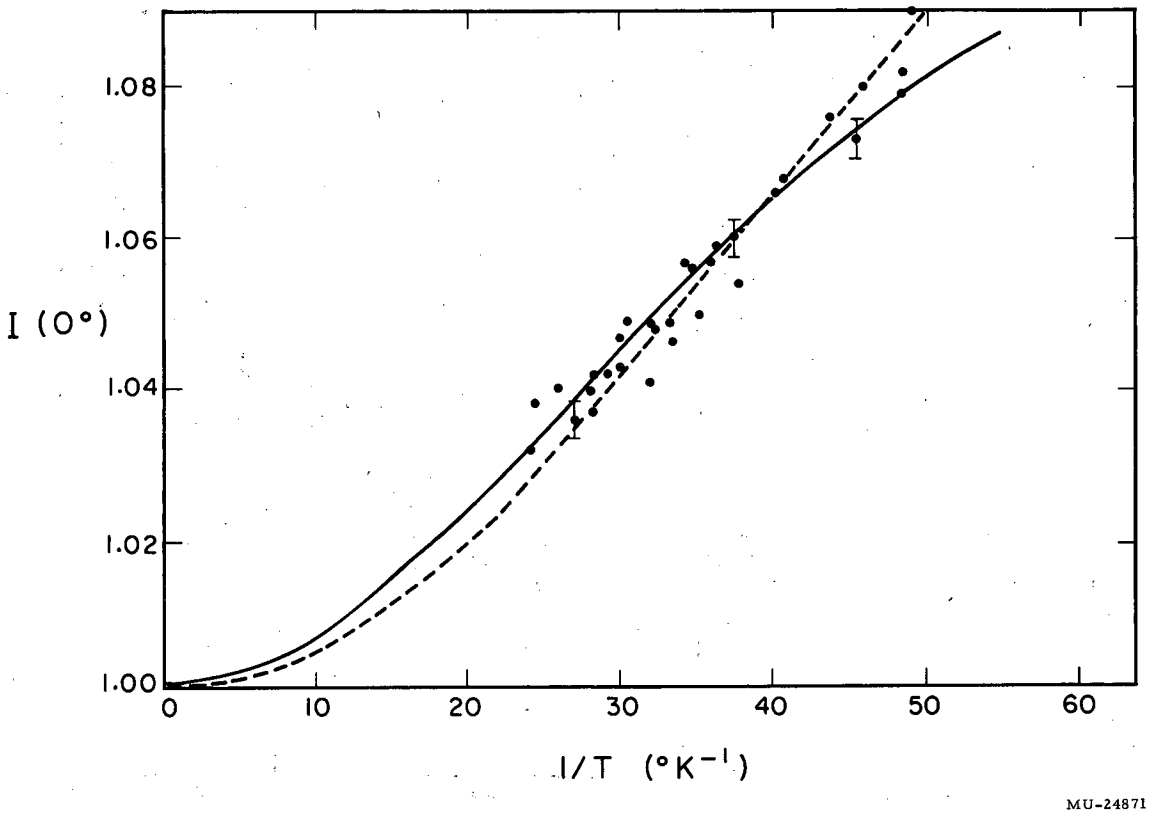

Fig. 23. Experimental values of $I(0^{\circ})$ and the corresponding theoretical fits for $|\mu_N| = 0.95$ nm (solid line) and $|\mu_N| = 0.60$ nm (dashed line).

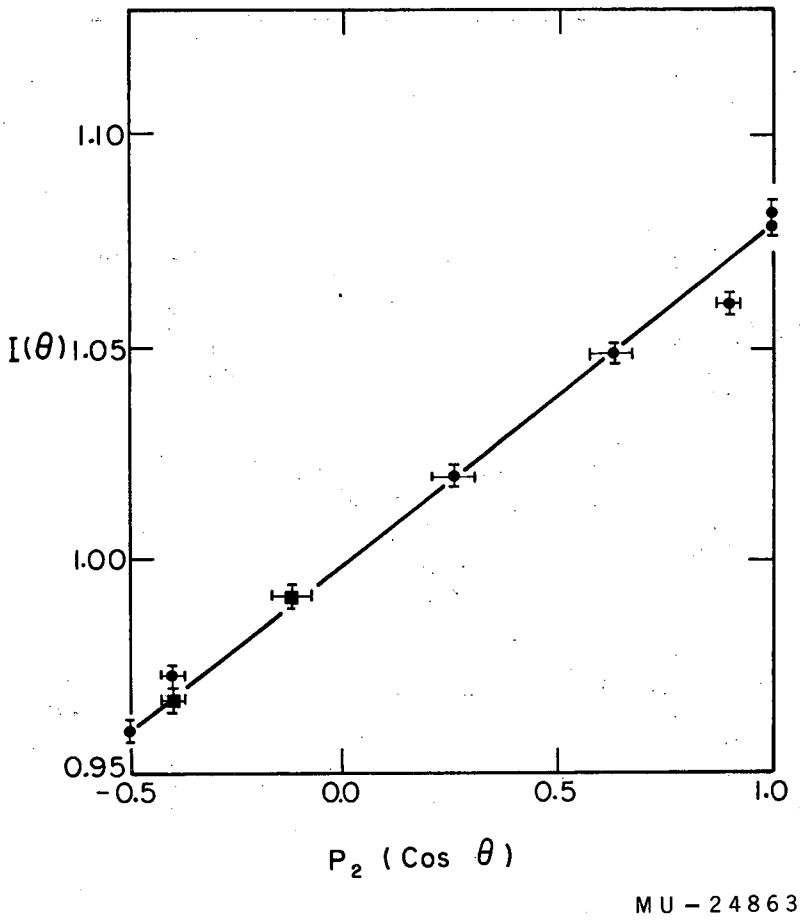

Fig. 24. Angular distribution of the 166-kev γ ray at 0.02°K. The line corresponds to $I(\theta) = 1 + 0.080\ P_2(\cos\theta)$.

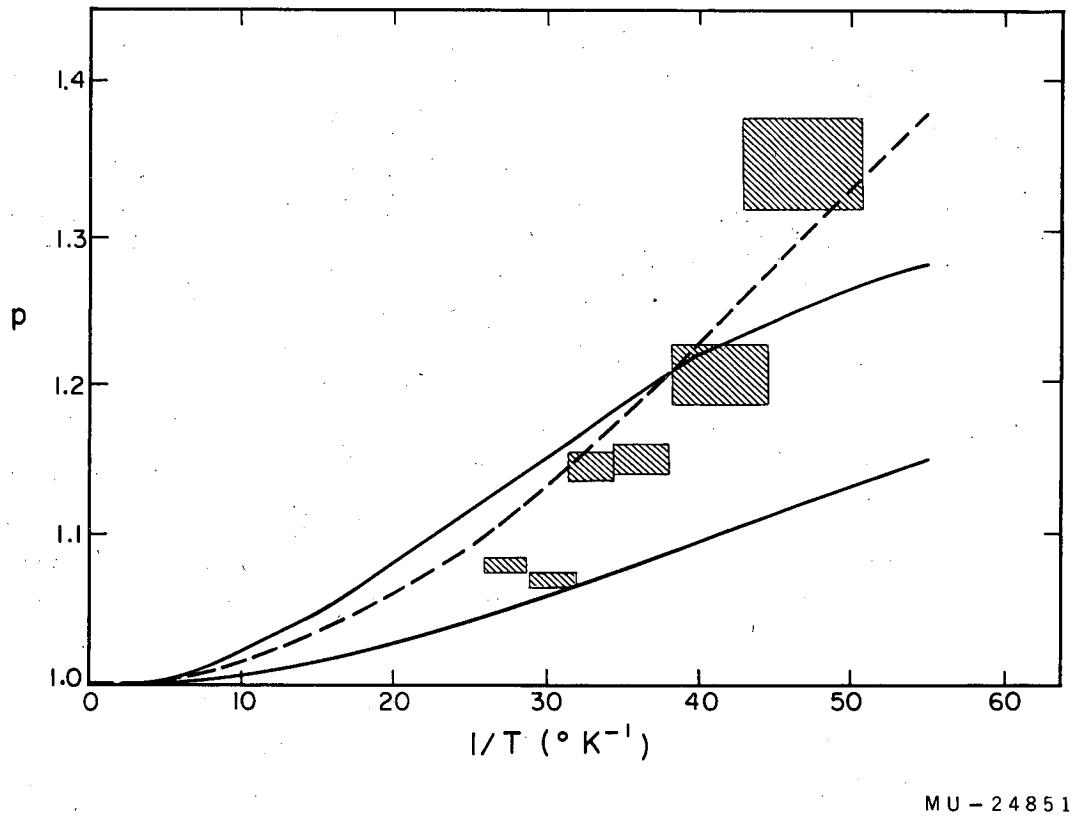

Fig. 25. Experimental values of p and the corresponding theoretical fits for $\delta = 0.034 \pm .034$ and $1.15 > |\mu_N| > 0.75$ nm (solid lines) and for $\delta = \infty$ and $|\mu_N| = 0.60$ nm (dashed line).

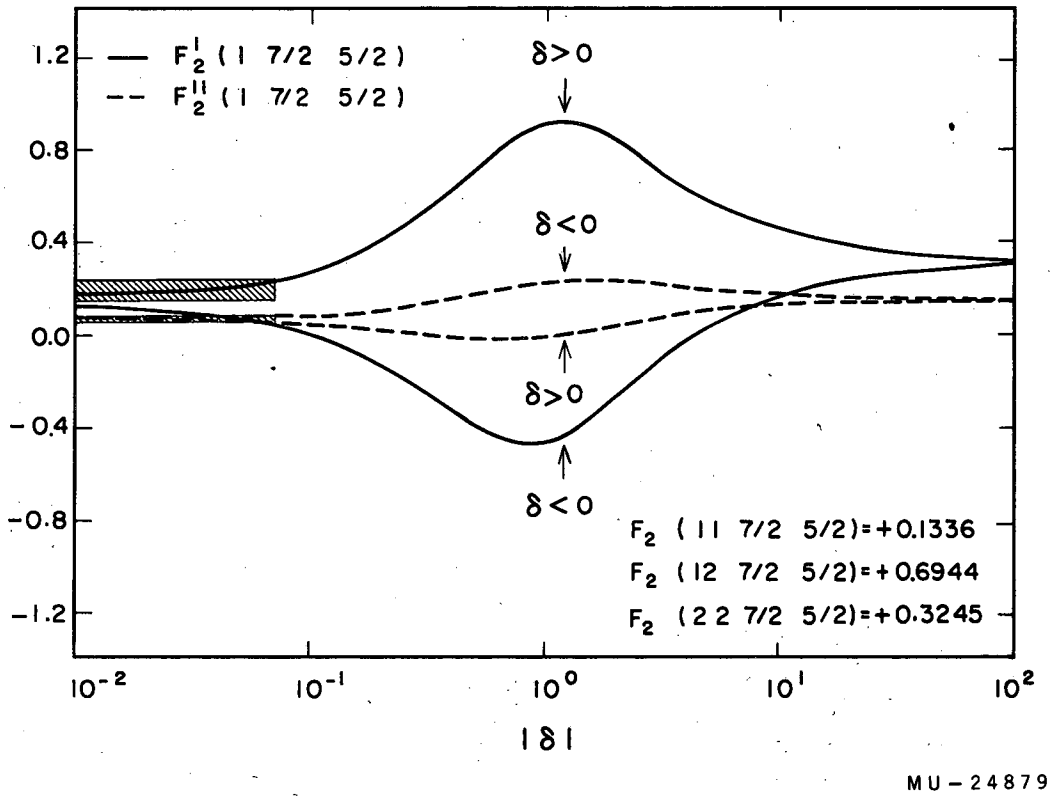

Fig. 26. Calculated F_2^I-vs-δ curves (solid lines) and F_2^{II}-vs-δ curves (dashed lines), with the corresponding experimental fit for $0.068 > \delta > 0$.

Performing the calculations with Eq. (VI-8) and (VI-9), one could use the values of δ in the range -4 to $-\infty$ with various values for $|\mu_N|$ to reproduce the $I(0^o)$-vs-1/T curve. However, the resulting p-vs-1/T curve was consistently below the experimental curve. The values of δ in the range 0 to -0.1 could not be used to reproduce either the $I(0^o)$-vs-1/T nor the p-vs-1/T curves. The required large values for B_2 (a function of 1/T) were such that the experimental $I(0^o)$ curve could be reproduced only for low 1/T values or for high 1/T values. The calculated p curve was too low in all cases.

The values of δ in the range 0.7 to 0 led to B_2, F_2', and F_2'' which reproduced both the experimental $I(0^o)$ curve and, except for one value, the p curve. The results are

$$|\mu_N| = 0.95 \pm .20 \text{ nm}, \qquad \delta = 0.034 \pm .034.$$

The limits of error were obtained as mentioned in Part VI. C. Eq. (VI-7), the experimental angular distribution, is in agreement with these values.

The lowest-temperature value of p, Fig. 25, does not fall within the calculated limits. This experimental value for p, statistically speaking, can assume a broader range of values than any value for p at a lower 1/T. This is because the statistical counting error involved in measuring N has a greater effect on the statistical error of p (not shown in Fig. 25) as N deviates further from unity. (See Part II. D.) In fact, the statistical error of this highest-1/T experimental value for p does include the upper theoretical curve (solid line) of Fig. 25.

For the range $\infty > \delta > 1$, the results obtained are

$$|\mu_N| = 0.60 \pm .10, \qquad \infty > \delta > 40.$$

Figure 23 shows the resulting $I(0^o)$-vs-1/T curve for $|\mu_N| = 0.60$ and $\delta = \infty$. Figure 24 shows the corresponding p-vs-1/T curve.

This result, a pure E2 transition, is probably coincidental, rather than real. La^{139} has a small quadrupole moment,[58] $Q = 0.21 \pm .04$ bar, therefore little nuclear deformation. Nuclear systematics indicate that M1 transitions ordinarily predominate in this case. Furthermore, as mentioned previously, the lifetime of the 166-kev level and the conversion coefficients of its γ ray suggest, although not conclusively, that the transition is mostly M1. Both Ce^{137} and Ce^{141} (see Part VI. E) have predominantly M1 transitions, and one would expect the same to occur for Ce^{139}. Finally, Heydenberg and Temmer[59] found no 166-kev γ ray in their Coulomb excitation work on La^{139}. This definitely suggests that there is little admixture of E2.

A more accurate nuclear orientation experiment would probably not be able to distinguish between these two possible solutions, which give $|\mu_N| = 0.95$, $\delta = 0.034$ and $|\mu_N| = 0.60$, $\delta = \infty$. Figure 23 shows that the two theoretical curves coincide within the statistical error of the experimental points, even though the counting rate was 10^5 count/min for the 166-kev γ ray. The same considerations apply to the coincidence of the two theoretical curves in Fig. 24. Permanent-magnet conversion-electron spectra, which sometimes just reveal enough resolving power for the rare-earth elements' L_I/L_{III} conversion ratios, would definitely decide which of the two sets of results is correct. Nevertheless, present data strongly indicate that the M1 result is the more resonable one.

Spin sequences other than $3/2 \xrightarrow{i\beta} 5/2 \xrightarrow{M1, E2} 7/2$ appear unlikely. The anisotropy of the 166-kev γ ray excludes a spin 1/2 for either the Ce^{139} ground state or the 166-kev level of La^{139}. The sign of the observed anisotropy excludes the sequence $3/2 \xrightarrow{i\beta} 3/2 \xrightarrow{E2} 7/2$ as $F_2(2, 2, 7/2, 3/2) = -0.1429$ and $U_2 > 0$. The log ft value for EC decay of Ce^{139} is not consistent with the sequence $3/2 \xrightarrow{i\beta} 7/2 \xrightarrow{M1, E2} 7/2$.

Grace et al.[60] have found a value $|\mu_N| = 1.1$ (corrected to Judd and Lindgren's value for $\langle r^{-3} \rangle$) for Ce^{139} from nuclear alignment experiments interpreted with the spin sequence $3/2 \xrightarrow{i\beta} 5/2 \xrightarrow{M1, E2} 7/2$.

This value is in agreement with our results. For, if the $5/2 \longrightarrow 7/2$ transition is pure M1, our results give $|\mu_N| = 1.15$, which is the Schmidt limit for Ce^{139}. Our results do not agree with those of Ambler et al.,[18] who oriented Ce^{139} in a crystal of cerium magnesium nitrate. They point out, however, that their results represent an attenuated anisotropy for the 166-kev γ ray owing to dipole-dipole interactions which greatly affect the planar, as opposed to axial, nuclear orientation that occurs in cerium magnesium nitrate.

E. Ce^{141}

The decay scheme of Ce^{141} has been extensively studied by many authors. The results published prior to February, 1958 are summarized in the "Table of Isotopes".[47] More recent results, cited below, are consistent with previous ones and lead to the energy-level scheme shown in Fig. 27.

An $f_{7/2}$ orbital was assigned to the ground state of Ce^{141} on the basis of its measured spin of 7/2. The measured spin of 5/2 for the ground state of Pr^{141} lead to the assignment of a $d_{5/2}$ orbital to this state. The M1 character of the γ ray from the 142-kev level of Pr^{141} led to the assignment of a $g_{7/2}$ orbital to this level. The Nd^{141} to Pr^{141} β-decay measurements by Polak et al.[61] are consistent with these spin assignments. The K-conversion coefficients of Joshi et al.[62] and the $1.9 \pm .2 \times 10^{-9}$-sec lifetime of the 142-kev level of Pr^{141}, as determined by DeWaard and Gerholm,[63] indicate an M1 character for this γ ray. That Heydenberg and Temmer[59] did not observe a 142-kev γ ray in their Coulomb excitation work on Pr^{141} strongly indicates that the E2 admixture in this transition is small. The outstanding exception to all these conclusions on the M1 character of the 142-kev γ ray is the work of Cook.[64] He finds $\alpha_K = 0.405 \pm .01$ from his internal-conversion-electron measurements. This was interpreted as evidence of predominantly an E2 transition on the basis of his extrapolated curves for α_2 and β_1, based on the English edition of

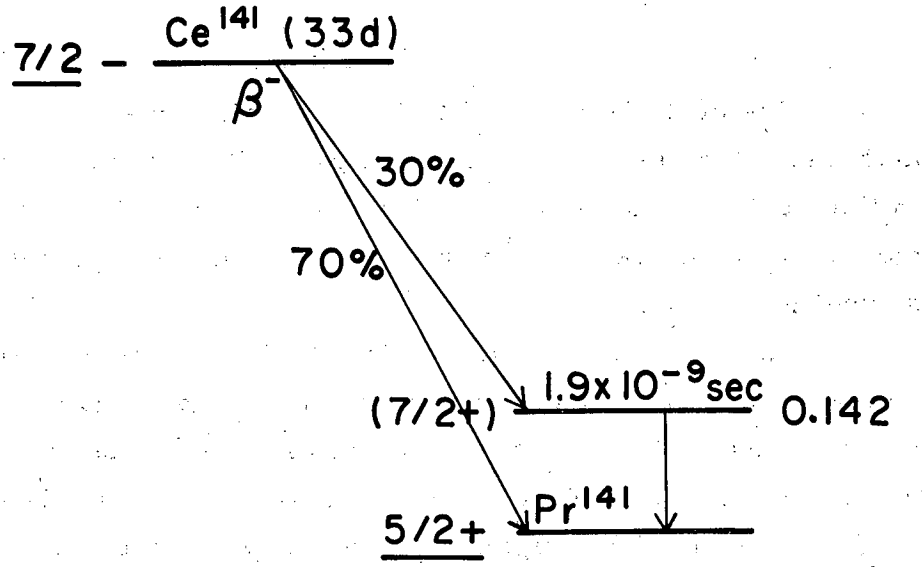

Fig. 27. Energy-level scheme.

Sliv and Band's values.[65] Cook quotes his extrapolations as giving $a_2 = 0.42$ and $\beta_1 = 0.435$. However this author, using published extrapolated curves[66] based on the same source as Cook used, finds $a_2 = 0.43 \pm .005$ and $\beta_1 = 0.41 \pm .005$. Comparing these values with Cook's experimental value for a_K gives the expected predominance of M1, not E2, character for the 142-kev γ ray.

The Ce^{141} source used for these experiments was permitted to decay for 30 days, so that the Ce^{143} activity would be absent from the γ-ray spectrum. The resulting γ-ray pulse-height spectrum obtained then showed only the 142-kev activity. This spectrum is shown in Fig. 28 for $I(0^\circ)$ and in Fig. 29 for $I(90^\circ)$. In both figures, the intensity has opposite signs for the 142-kev peak and for the Compton distribution around 100 kev. This effect is due to the plane polarized γ ray's being scattered preferentially from the source crystal (15 grams of neodymium ethylsulfate) and from the glass walls of the nuclear orientation apparatus. This phenomenon may prove to be a more accurate means of determining the plane polarization of γ rays than the conventional polarimeter for energies less than about 500 kev. This is because the counting rates are greater by an order or two of magnitude than with a polarimeter, since no coincidence circuit is required. A quantitative expression for dealing with this effect is currently under preparation. The phenomenon holds promise for both nuclear alignment experiments and angular correlation experiments.

The intensity $I(0^\circ)$ of the 142-kev γ ray of Pr^{141} as a function of $1/T$ is shown in Fig. 30. The intensity $I(\theta)$ as a function of $P_2(\cos\theta)$ at $1/T = 50$ is shown in Fig. 31. This angular distribution was found to be

$$I(\theta) = 1 + (0.170 \pm .006) P_2(\cos\theta) \,. \qquad \text{(VI-10)}$$

A $P_4(\cos\theta)$ term was not indicated by the data. Nevertheless, since the ground-state spin of Ce^{141} is 7/2, this term theoretically may exist.

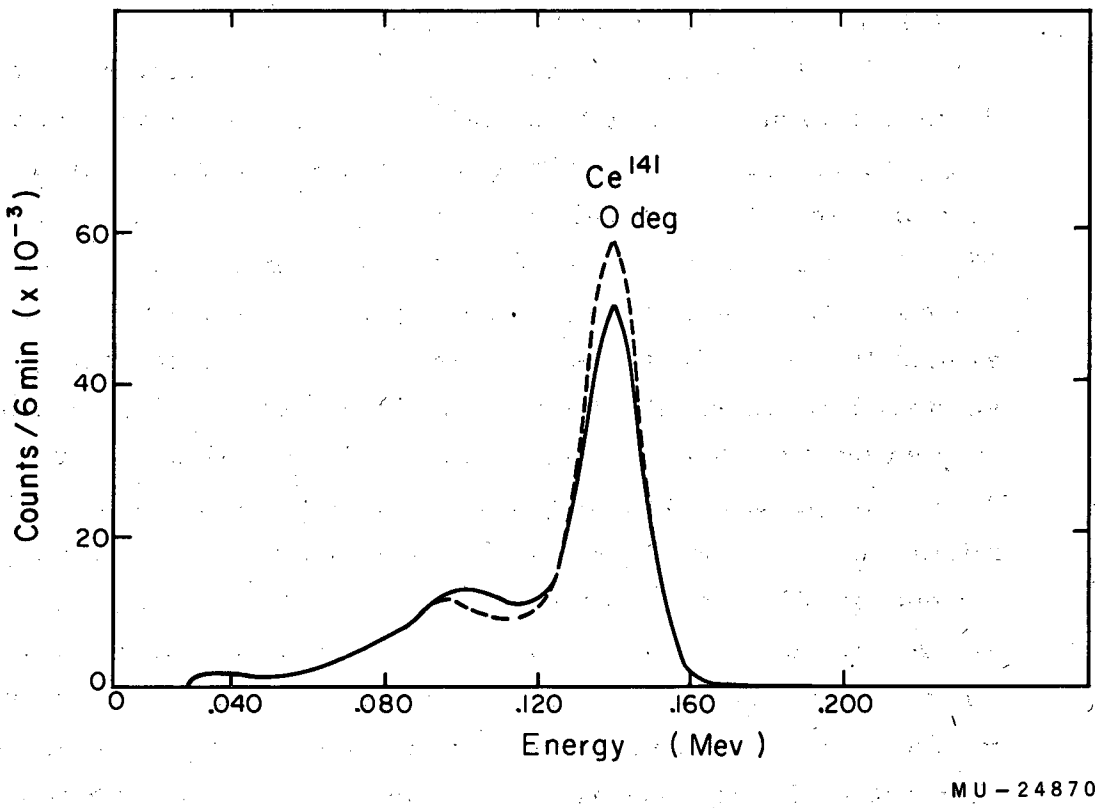

Fig. 28. Gamma-ray pulse-height spectrum at 1.2°K (solid line) and at 0.02°K (dashed line). Measurement made at $\theta = 0^{\circ}$.

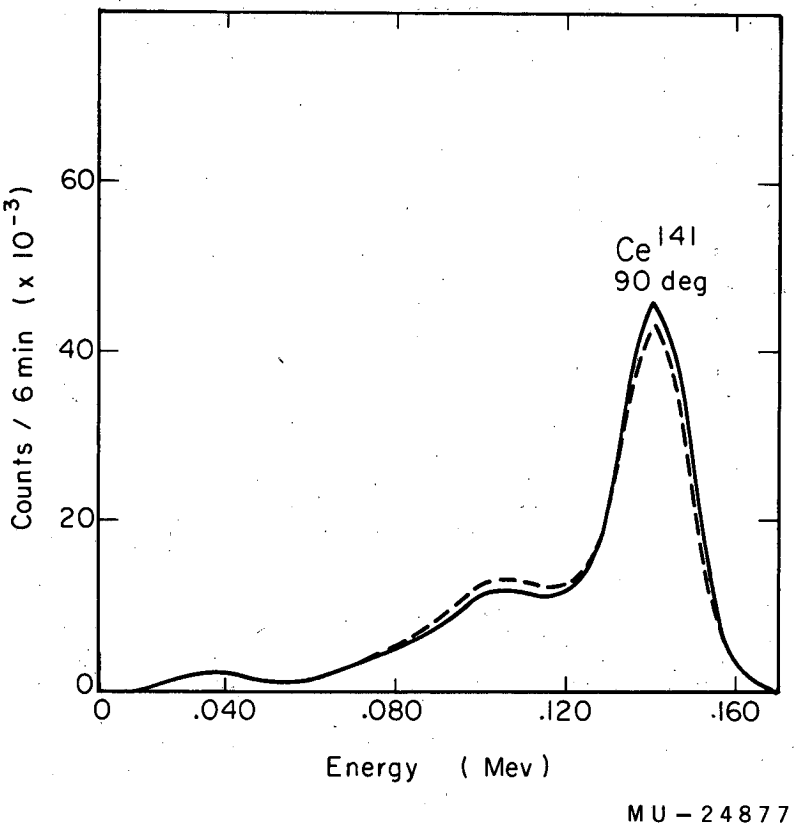

Fig. 29. Gamma-ray pulse-height spectrum at 1.2°K (solid line) and at 0.02°K (dashed line). Measurement made at $\theta = 90°$.

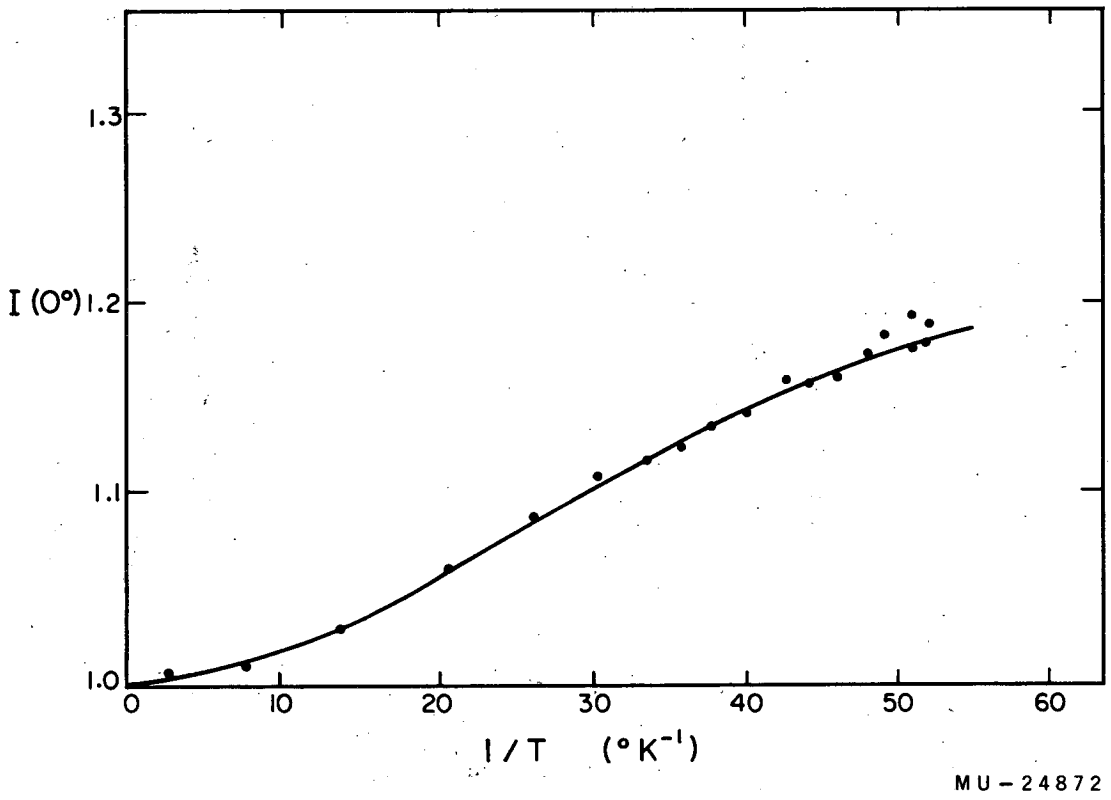

Fig. 30. Experimental values of $I(0^{o})$ and the corresponding theoretical fit for $|\mu_N| = 1.30$ nm.

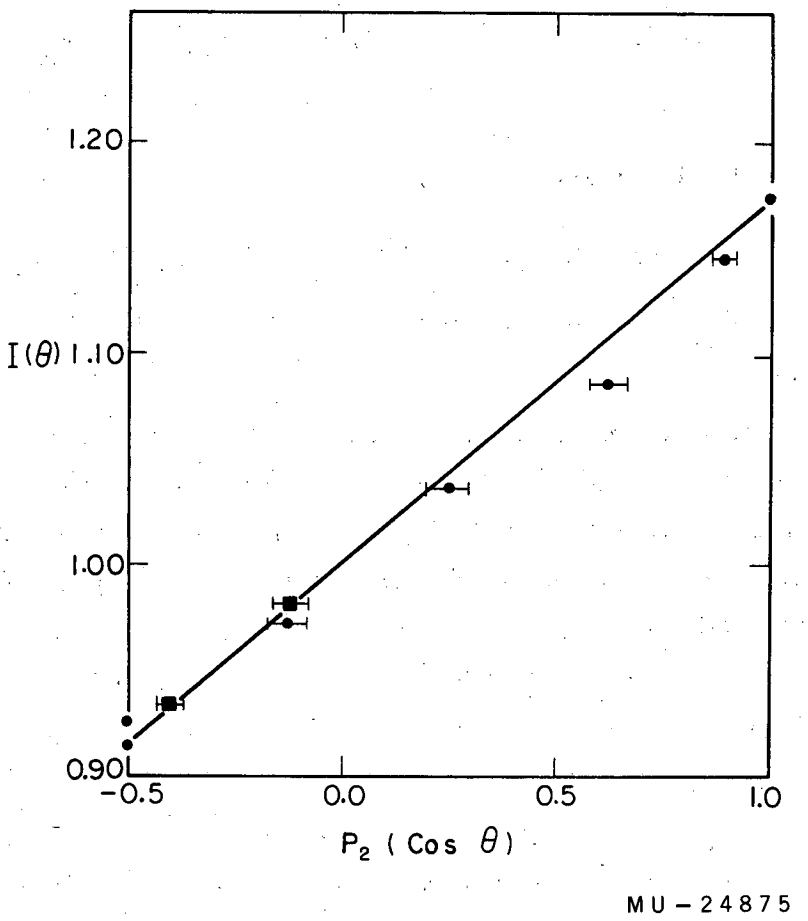

Fig. 31. Angular distribution of the 142-kev γ ray at 0.02°K. The line corresponds to $I(\theta) = 1 + 0.170\ P_2 (\cos \theta)$.

For the 142-kev transition of Pr^{141}, the unobserved preceding β transition for the sequence $7/2 \xrightarrow{1\beta} 7/2$ gives $U_2 = 1.000$ and $U_4 = 1.000$ for a pure $i_\beta = 0$ transition; for a pure $i_\beta = 1$ transition, $U_2 = 0.8096$ and $U_4 = 0.365$. On the assumption for the moment that $i_\beta = 0$, Eq. II-3 becomes, for the spin sequence $7/2 \xrightarrow{0} 7/2 \xrightarrow{M1, E2} 5/2$,

$$I(\theta) = 1 + F_2' (1, 5/2, 7/2)B_2P_2(\cos\theta) + F_4' (1, 5/2, 7/2)B_4P_4(\cos\theta), \tag{VI-11}$$

and Eq. (II-4) becomes

$$p = \frac{1 + B_2 [(-1/2)F_2' + 3F_2''] + B_4 [(3/8F_4' - (15/2)F_4'']}{1 + B_2 [(-1/2)F_2' - 3F_2''] + B_4 [(3/8)F_4' + (15/2)F_4'']} . \tag{VI-12}$$

The value of p as a function of $1/T$ is shown in Fig. 32. Six measurements were made of N and used individually to calculate p vs $1/T$. Owing to the large counting rate and the large anisotropic effects, the agreement between theory and experiment in both Figs. 29 and 31 is truly excellent.

The boundary conditions on δ were found by utilizing Part II-D. This gives

$$F_2' > 0 \qquad \text{and} \qquad F_2'' > -0.039$$

for $|\mu_N| \leq 1.91$, the Schmidt limit.

By using Fig. 33, two ranges for δ were found: $0 > \delta > -0.7$ and $0.2 > \delta > 0$. No solution could be found for the first range. The small value for $|\mu_N|$ required for δ in this region gave a B_2 such that the $I(0^\circ)$-vs-$1/T$ curve of Fig. 30 could not be reproduced with regard to curvature as a function of $1/T$. In addition, the corresponding p-vs-$1/T$ curve always fell below the experimental curve.

The values of δ in the second range, using Eq. (VI-11) and (VI-12), which satisfied both the experimental $I(0^\circ)$ and p curves, gave

$$|\mu_N| = 1.30 \pm .20, \qquad \delta = 0.066 \pm .022 .$$

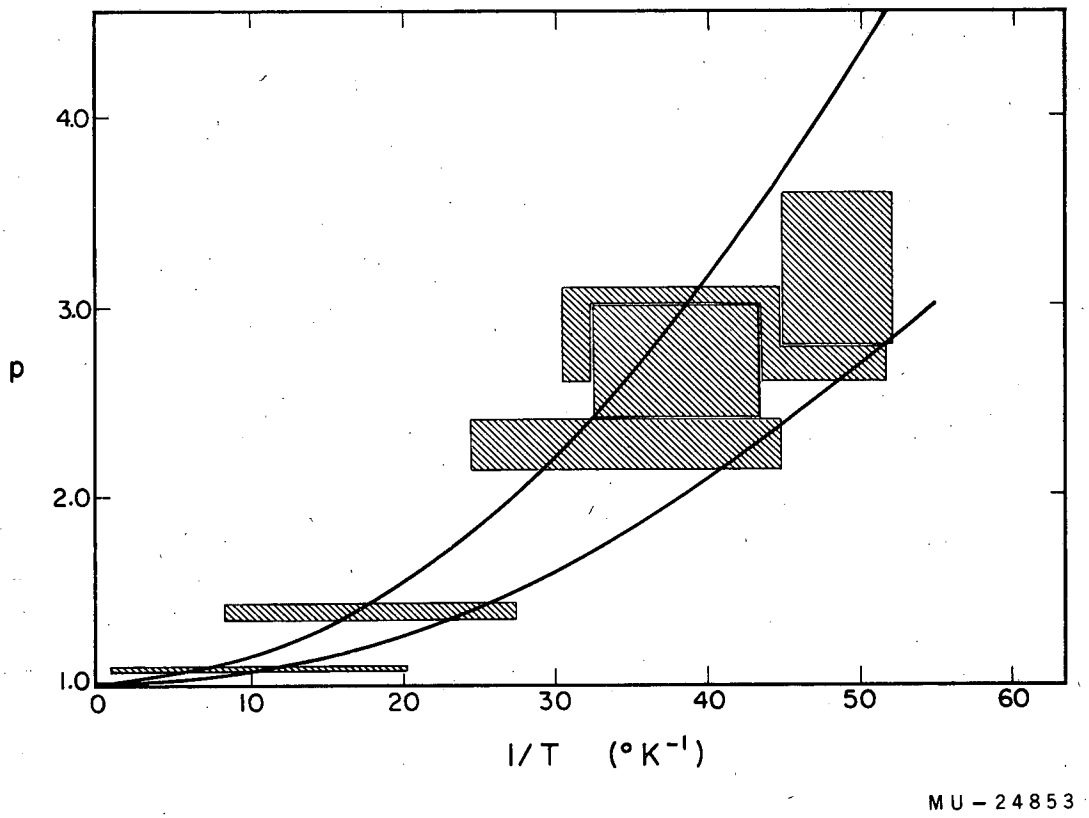

Fig. 32. Experimental values of p and the corresponding theoretical fits for $\delta = 0.066 \pm .022$ and $1.50 > |\mu_N| > 1.10$.

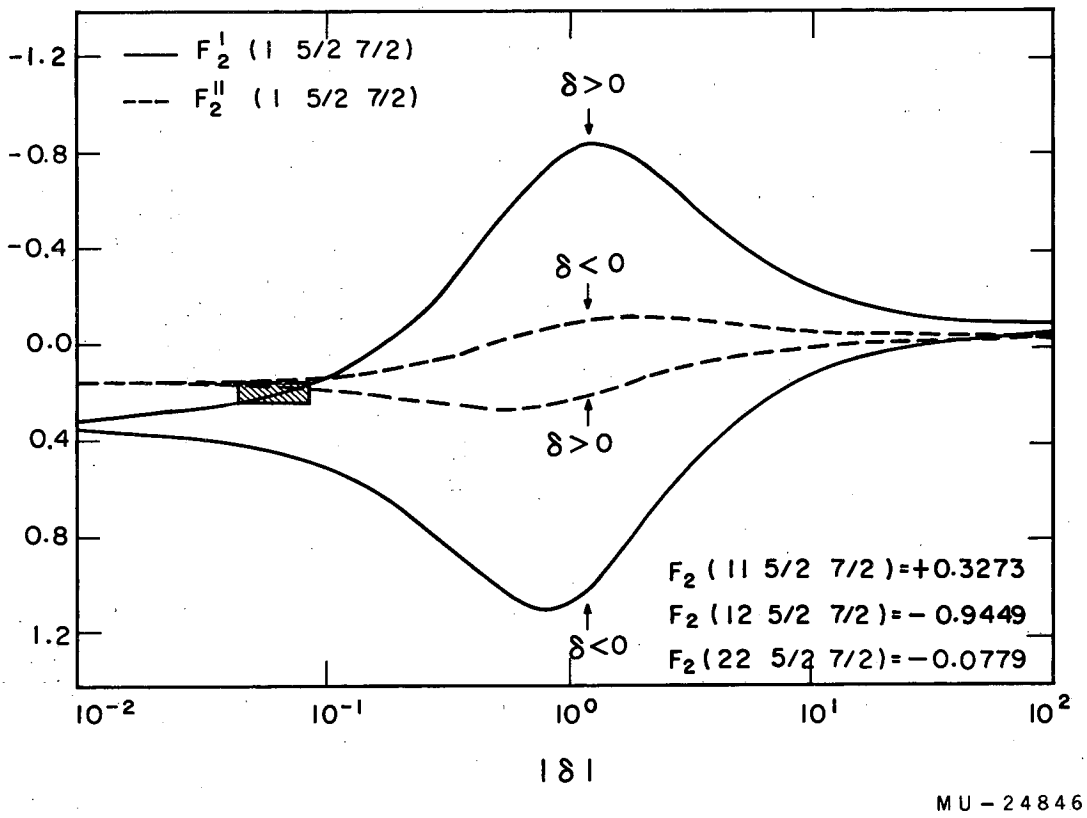

Fig. 33. Calculated F_2^I-vs-δ curves (solid lines) and F_2^{II}-δ curves (dashed lines), with the corresponding experimental fit for $0.088 > \delta > 0.044$.

Equation (VI-10), the experimental angular distribution, agrees well with these values. No $P_4(\cos\theta)$ term was seen experimentally, because of the small $F'_4 = \frac{\delta^2}{1+\delta^2} F_4(2, 2, 5/2, 7/2) = 0.002$.

The previous results are based on the assumption that the beta transition is pure $i_\beta = 0$. For a pure $i_\beta = 1$ transition, Eq. (VI-11) becomes

$$I(\theta) = 1 + 0.8096\, F'_2 B_2 P_2(\cos\theta) + 0.365\, F'_4 B_4 P_4(\cos\theta),$$

and Eq. (VI-12) undergoes a corresponding change. The solution in this case is

$$|\mu_N| = 1.60 \pm .20, \qquad \delta = 0.066 \pm .022.$$

These values could not be used to reproduce the experimental $I(0^\circ)$ and p curves as well as in the case of the $i_\beta = 0$ solution. This large a moment introduces a curvature in B_2 as a function of $1/T$ that lies outside the statistical error of the measurements. This leads one to feel that the beta transition is predominantly $i_\beta = 0$. A more concrete indication is the measurement by Kedzie et al.[3] of the magnetic hyperfine coupling constant of Ce^{141} by parmagnetic resonance to give (when corrected to Judd and Lindgren's value for $\langle r^{-3} \rangle$)

$$|\mu_N| = 1.2 \pm .1.$$

This value of Kedzie's for $|\mu_N|$ is in remarkably good agreement with the value for $|\mu_N|$ found in our experiments for $i_\beta = 0$. Kedzie's value is independent of the beta transition involved in the decay of Ce^{141}. Therefore it can be concluded that the $7/2 \xrightarrow{i_\beta} 7/2$ transition is predominantly a $i_\beta = 0$ beta transition.

Further conclusions may be drawn from the ratio of Kedzie's $|\mu_N|_K$ value to our $|\mu_N|_H$ value for $i_\beta = 0$, which is

$$\frac{|\mu_N|_K}{|\mu_N|_H} = \frac{0.074 \langle + |N_x| - \rangle_{CeMgNO_3}}{0.0496 \langle + |N_z| + \rangle_{CeEtSO_4}} \approx 1,$$

where $\langle + |N_x| - \rangle$ is the matrix element for the vector

$$\vec{N} = \vec{l} = \vec{s} + 3(\vec{r} \cdot \vec{s})\vec{r}/r^2$$

evaluated by Judd and Pryce[67] for a Ce^{+3} ion in a cerium magnesium nitrate lattice, and $\langle + |N_z| + \rangle$ was evaluated by Elliott and Stevens[24] for a Ce^{+3} ion in a cerium ethylsulfate lattice. (See Part II.C.) This ratio is independent of the value of $\langle r^{-3} \rangle$ for the Ce^{+3} ion. Thus, this ratio theoretically should equal unity if the two matrix elements have been evaluated exactly. Within the limits of Kedzie's and our experiments, the ratio does equal unity. Furthermore, this result indicates the validity of our usage of Elliott and Steven's ground-state wave function (see Part II. D) for a Ce^{+3} ion in a cerium ethylsulfate lattice as a good approximation for a Ce^{+3} ion in a neodymium ethylsulfate lattice. This result is expected, as the unpaired 4f electron of Ce^{+3} is shielded by $n = 5$ electrons, and Coulomb interactions with surrounding ions are ordinarily minimized in other X^{+3} lattice sites.

Cacho et al.[28] have obtained nuclear alignment results for Ce^{141} in a neodymium ethylsulfate lattice. Their findings (corrected to Judd and Lindgren's values[25] for $\langle r^{-3} \rangle$) are

$$|\mu_N| = 0.99 \pm .26 \text{ for } i_\beta = 1,$$

$$|\mu_N| = 0.87 \pm .21 \text{ for } i_\beta = 0,$$

$$\delta = 0.08 \pm .02.$$

These results for $|\mu_N|$ are slightly outside our limits of error. This could be explained by several factors. The polarimeter used

by Cacho had been only approximately calibrated. The $T\text{-}T^*$ relationship for neodymium ethylsulfate had not then been measured and therefore was estimated. In view of this, the discrepancy in the results is understandable.

Spin sequences other than the $7/2 \xrightarrow{i_\beta} 7/2 \xrightarrow{M1, E2} 5/2$ sequence used in obtaining our results seem highly improbable. The only spin involved in the decay that has not been measured is that of the 142-kev level of Pr^{141}. This cannot, on the basis of the anisotropy of the 142-kev γ ray, be spin 1/2. The experimental log ft values indicate a first-forbidden, $\Delta I = 0$ or 1, yes transition. Thus the spin is unlikely to be 3/2 or 11/2. The sign of the measured anisotropy definitely excludes a spin of 9/2, for this gives $U_2 > 0$, $U_4 > 0$ and $F_2(2, 2, 5/2, 9/2) = -0.4325$, $F_4(2, 2, 5/2, 9/2) = -0.2684$. The remaining possibility is a spin 5/2 for the 142-kev level. Evaluating the resulting boundary conditions for δ gives $F_2' > 0$ and $F_2'' > 0$. Two ranges in δ result from this. For the first range, $\infty > \delta > 5.6$ (thus predominantly an E2 transition), there is no solution for $|\mu_N| \leq 1.91$, the Schmidt limit, as an $F_2' \geq 0.24$ is required to reproduce the experimental $I(0^\circ)$ and p curves. However, the theoretical maximum for F_2' is 0.19. For the second range $-2.5 > \delta > -\infty$ (again predominantly an E2 transition), there also is no solution for $|\mu_N| \leq 1.91$. The experimental curve of $I(0^\circ)$ can be reproduced, but the p-vs-1/T curve cannot. The highest possible p value calculated from this range of δ is $p = 1.61$ at $1/T = 50$. Figure 32 shows that this value is completely outside our experimental values. This failure to find a solution giving an E2 character to the 142-kev γ ray is consistent with the experimental angular distribution of Fig. 31, and with the experimental results of all workers quoted previously.

Thus, we can uniquely assign a spin of 7/2 to the 142-kev level of Pr^{141}. The shell model is in agreement with this result.

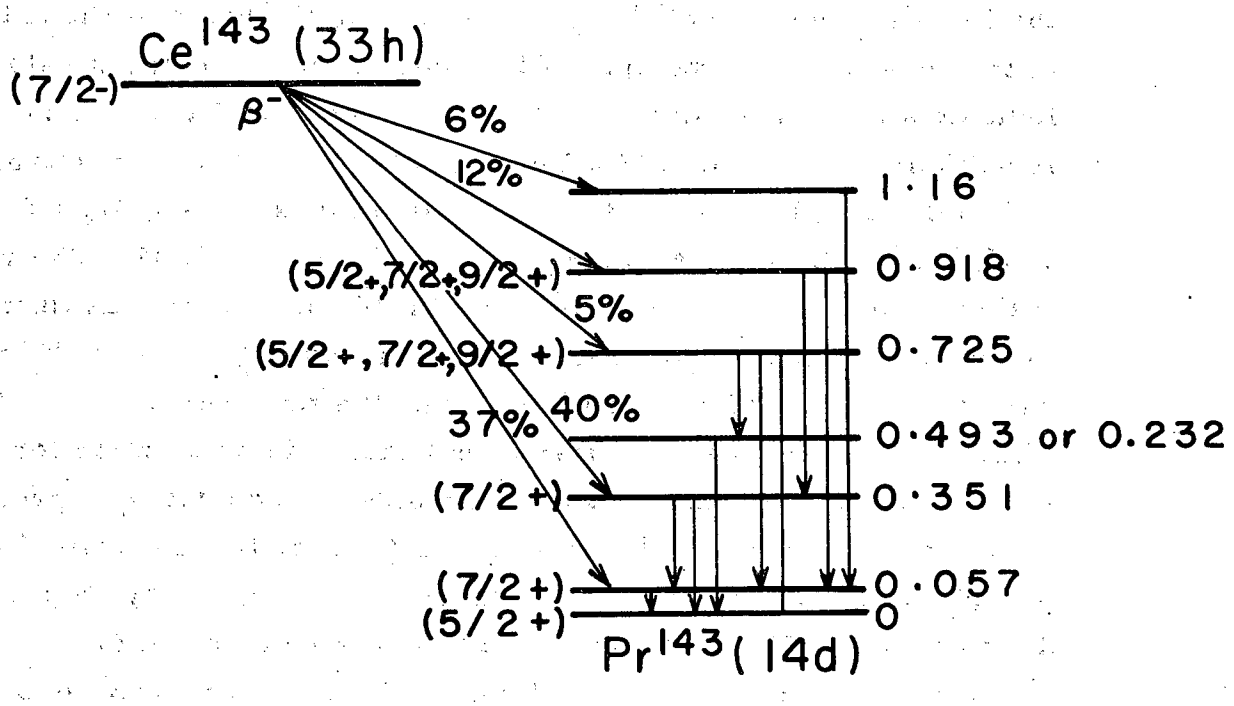

Fig. 34. Energy-level scheme.

F. Ce^{143}

The decay scheme of Ce^{143} has been studied by Martin et al.[68] utilizing γ-ray, coincidence, and conversion-electron spectroscopic techniques. Their results indicate the energy-level scheme in Fig. 34. The relative order of the 232- and 493-kev γ rays was not determined.

A $d_{5/2}$ orbital was assigned to the ground state of Pr^{143} on the basis of its first-forbidden β decay to Nd^{143}, which has a measured spin of 7/2. The measurements by Postma and Huiskamp[69] on β emission from polarized Pr^{143} gives evidence that the spin of Pr^{143} is indeed 5/2. The M1 character of the γ ray from the 57-kev level of Pr^{143} led to the assignment of a $g_{7/2}$ orbital to this level. Since Martin did not observe a β decay from Ce^{143} ground state to Pr^{143} ground state, he assigned an $h_{9/2}$ orbital to Ce^{143}. Nevertheless, the absence of this beta transition does not rule out an $f_{7/2}$ orbital for Ce^{143}. Nd^{147} has a measured spin of 5/2 and yet no beta decay to the 7/2 ground state of Pm^{147} has been observed. Both on the basis of this fact, and on the basis that the shell-model ground-state spin prediction was valid for the ground state of Ce^{141} (spin 7/2), an $f_{7/2}$ orbital was assigned to the ground state of Ce^{143}.

The γ-ray pulse-height spectrum obtained for Ce^{143} is shown in Fig. 35. The 142-kev peak is due to the decay of Ce^{141}, present as an impurity in our source. The resolved γ-ray peaks due to the decay of Ce^{143} have energies of 232, 294, 351, 493, 668, 725, 861, and 1100-kev. This spectrum agrees with that obtained by Martin. Our spectrum was plotted on a linear scale in order to indicate the difficulty in obtaining experimental intensity results on any but the high-intensity 294-kev γ ray of Pr^{143}.

The intensity $I(0^\circ)$ of the 294-kev γ ray of Pr^{143} as a function of 1/T is shown in Fig. 36. The intensity $I(\theta)$ as a function of $P_2(\cos\theta)$ is shown in Fig. 37. This angular distribution was found to be

$$I(\theta) = 1 + (0.045 \pm .010)\, P_2(\cos\theta)\,. \qquad \text{(VI-13)}$$

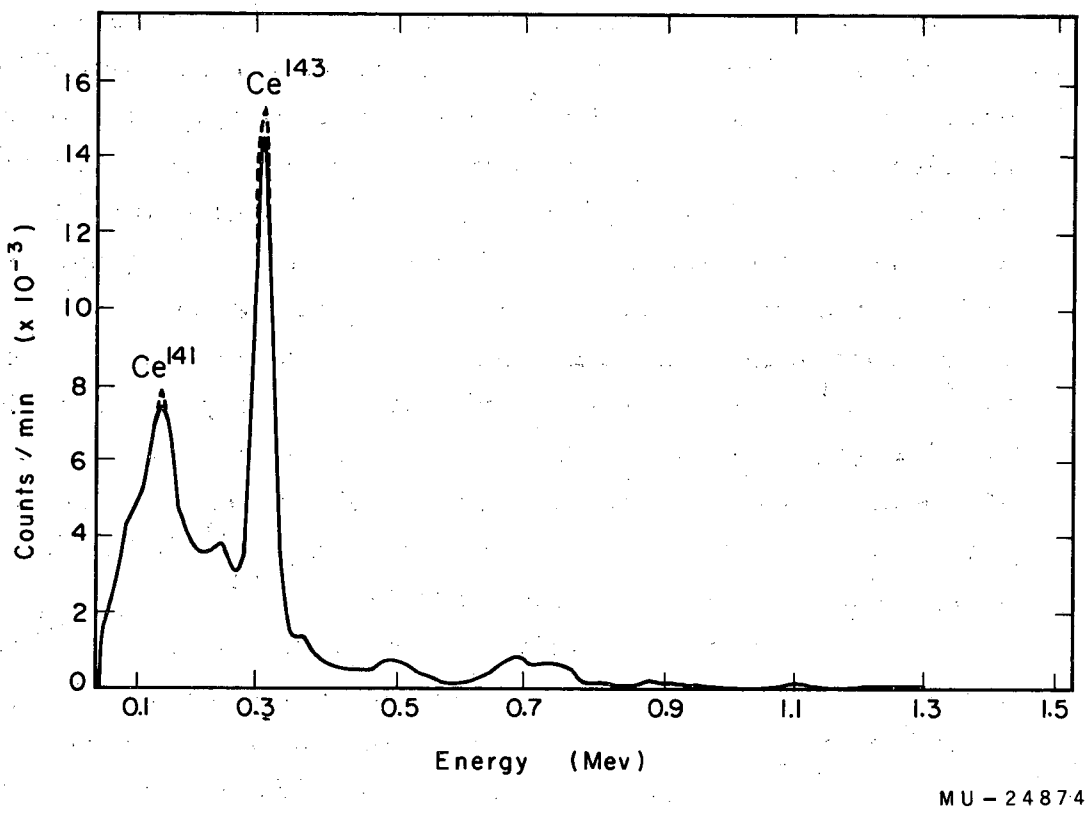

Fig. 35. Gamma-ray pulse-height spectrum at 1.2°K (solid line) and at 0.02°K (dashed line). Measurement made at $\theta = 0^{o}$.

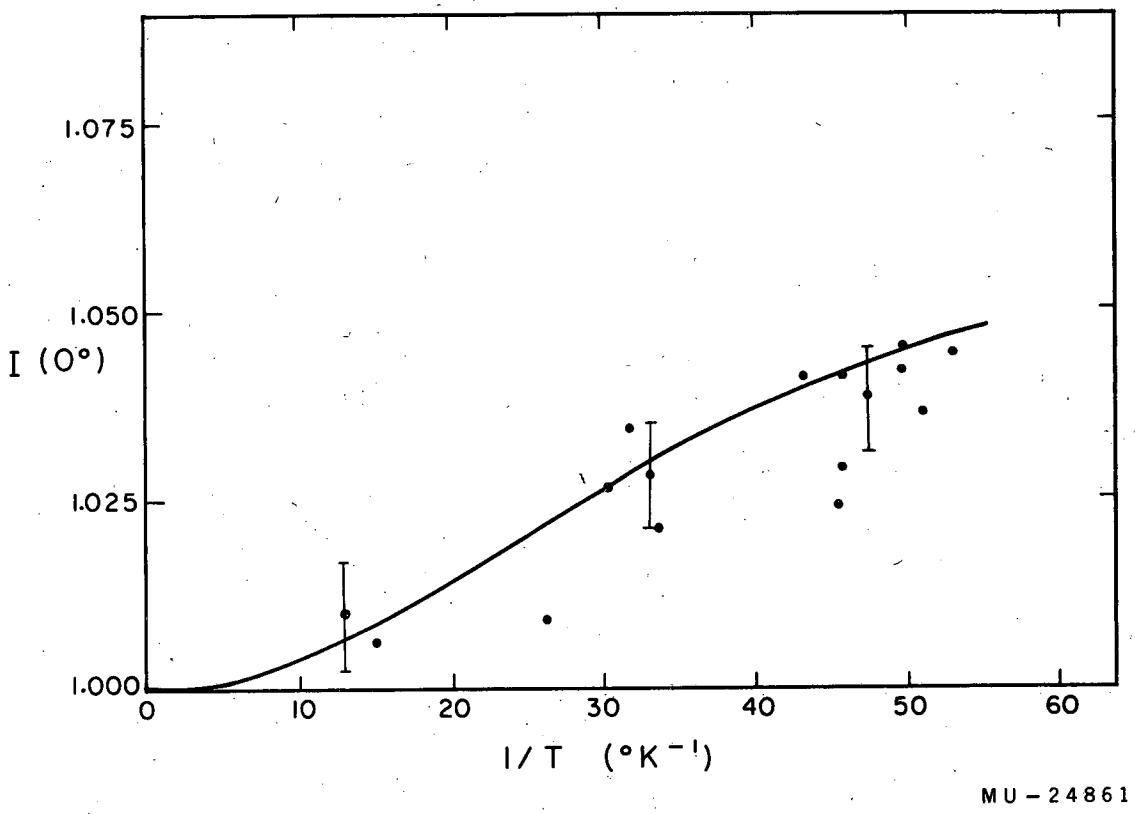

Fig. 36. Experimental values of $I(0^{\circ})$ and the corresponding theoretical fit for $|\mu_N| = 1.00\,\text{nm}$.

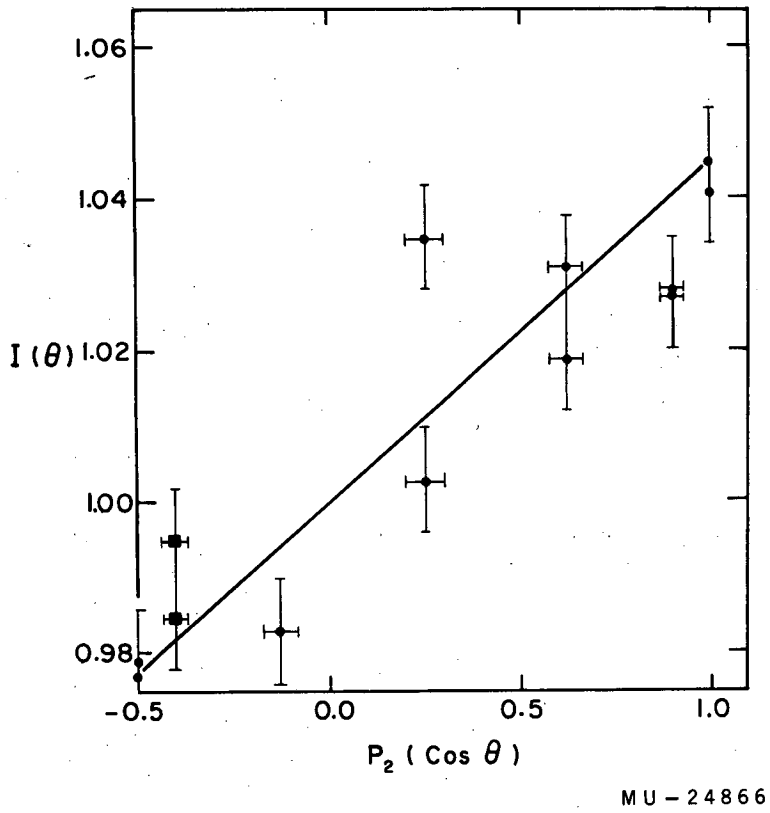

Fig. 37. Angular distribution of the 294-kev γ ray at 0.02°K. The line corresponds to $I(\theta) = 1 + 0.045 P_2(\cos \theta)$.

The value of p as a function of 1/T is shown in Fig. 38. Eight measurements were made of N and used to calculate the three plotted values of p for the 294-kev γ ray. No correction was felt necessary for these p values on the 294-kev γ ray as regards the small contribution of higher-energy γ rays of Pr^{143} to the polarimeter coincidence events. The statistical limits of error were larger than any error due to these contributions.

For the 294-kev transition of Pr^{143}, an attempt was made to assign to the 351-kev and 57-kev levels such spins that a magnetic moment of 1.3 nm could be found for Ce^{143}. Nuclear moment systematics indicate that Ce^{141} and Ce^{143} should have approximately the same magnetic moment. (As was experimentally found for Ce^{137} and Ce^{139}.) Since the log ft values found by Martin indicate first-forbidden beta transitions to the 351-kev and 57-kev levels, a spin of 5/2, 7/2, or 9/2 is indicated for the 351-kev level, and a spin of 5/2 or 7/2 is indicated for the 57-kev level. (A spin of 9/2 is unlikely owing to the M1 character of the 57-kev γ ray.) By utilizing each combination of spins possible for the two levels, it was found that no solution existed that gave a magnetic moment larger than 1.0 nm. In view of this, a $g_{7/2}$ orbital was assigned to both the 351-kev and 57-kev levels. As previously stated, this assignment is reasonable for the 57-kev level because of the M1 character of its γ ray. In addition, this spin of 7/2 has been verified for the first excited state (142-kev) of Ce^{141}. The fact that 40% of the β transitions are to the 351-kev level of Pr^{143} and that 37% of the β transitions are to the 57-kev level of Pr^{143} indicates that the assignment of a $g_{7/2}$ orbital to both levels is not unreasonable.

Consequently, for the 294-kev transition in Pr^{143}, the unobserved β transition for the sequence $7/2 \xrightarrow{i_\beta} 7/2$ gives $U_2 = U_4 = 1$ for a pure $i_\beta = 0$ transition and $U_2 = 0.8096$ and $U_4 = 0.365$ for a pure $i_\beta = 1$ transition. Upon assumption for the moment that $i_\beta = 0$, Eq. (II-3) becomes, for the spin sequence $7/2 \xrightarrow{0} 7/2 \xrightarrow{M1, E2} 7/2$,

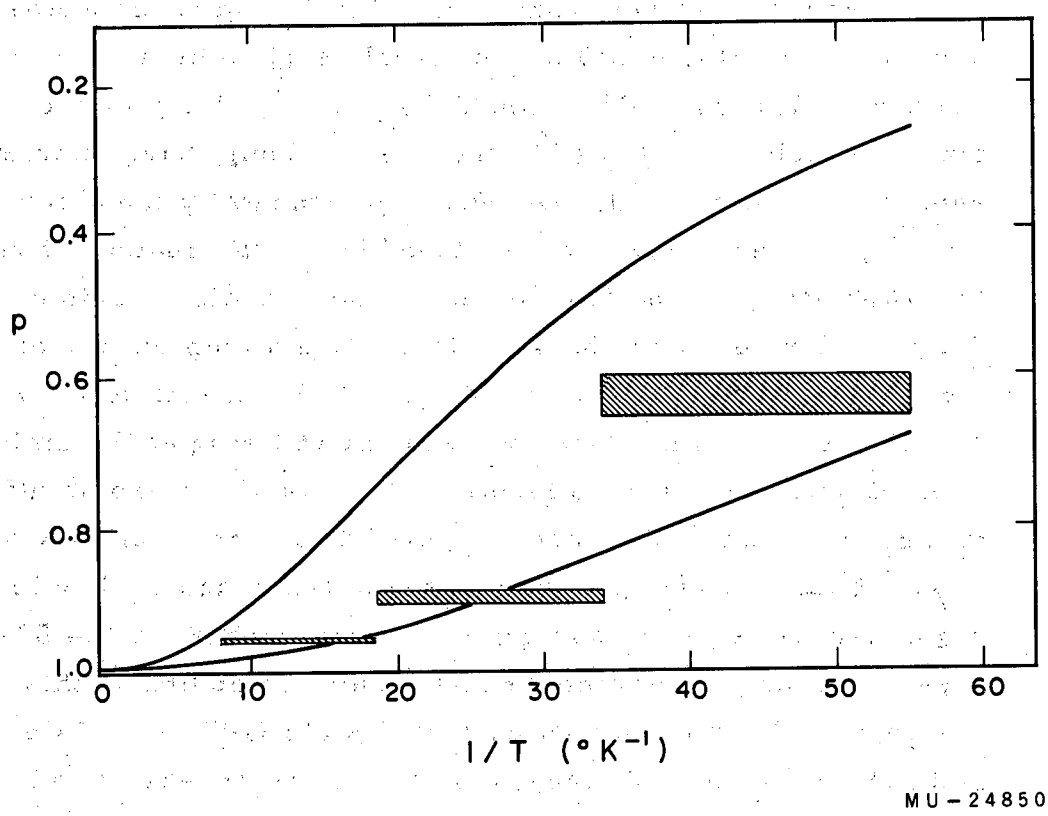

Fig. 38. Experimental values of p and the corresponding theoretical fits for $\delta = -0.80 \pm .20$ and $1.30 > |\mu_N| > 0.70$.

$$I(\theta) = 1 + F_2'(1, 7/2, 7/2)B_2P_2(\cos\theta) + F_4'(1, 7/2, 7/2)B_4P_4(\cos\theta), \quad \text{(VI-14)}$$

and Eq. (II-4) becomes

$$p = \frac{1 + B_2\left[(-1/2)F_2' + 3F_2''\right] + B_4\left[(3/8)F_4' - (15/2)F_4''\right]}{1 + B_2\left[(-1/2)F_2' - 3F_2''\right] + B_4\left[(3/8)F_4' + (15/2)F_4''\right]}. \quad \text{(VI-15)}$$

The boundary conditions on δ were found, by utilizing Part II. D, to be

$$F_2' > 0 \qquad \text{and} \qquad F_2'' < 0$$

for $|\mu_N| \leq 1.91$, the Schmidt limit. Figure 39 thus gives one range for δ: $-2.0 < \delta < -0.5$. With Eqs. (VI-14) and (VI-15), the values of δ that satisfied both the experimental $I(0^\circ)$ and p curves give

$$|\mu_N| = 1.00 \pm .30, \qquad \delta = -0.80 \pm .20.$$

These results give an angular distribution

$$I(\theta) = 1 + 0.056\ P_2(\cos\theta) - 0.011\ P_4(\cos\theta),$$

which is in agreement with the angular distribution of Fig. 37, since the $P_4(\cos\theta)$ term above is small compared with the $P_2(\cos\theta)$ term.

For a pure $i_\beta = 1$ beta transition, Eq. (VI-14) becomes

$$I(\theta) = 1 + 0.8096\ F_2'B_2P_2(\cos\theta) + 0.365\ F_4'B_4P_4(\cos\theta),$$

and Eq. (VI-15) is also correspondingly changed. The solution in this case gives

$$|\mu_N| = 1.20 \pm .30, \qquad \delta = -0.80 \pm .20.$$

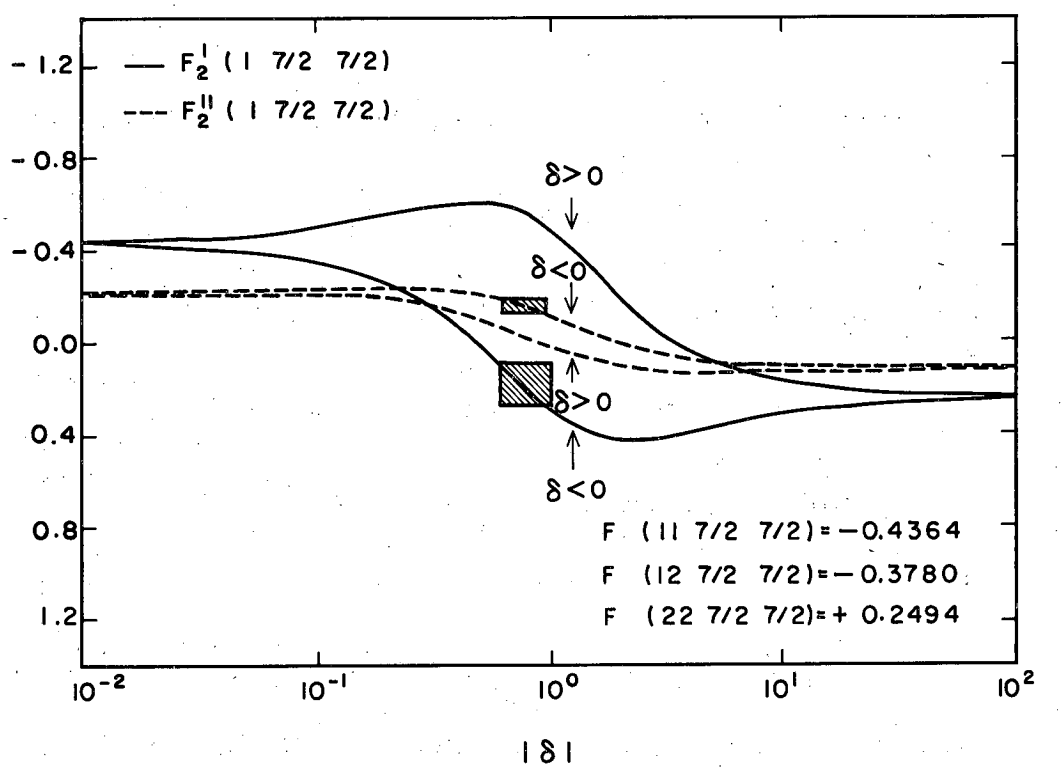

Fig. 39. Calculated F_2^I versus δ curves (solid lines) and F_2^{II} versus δ curves (dashed lines), with the corresponding experimental fit for $-1.00 > \delta > -0.60$.

The experimentally measured effects are so small that the predominance of one beta transition over the other cannot be detected.

Table VI gives experimental results for $I(\theta)$ at $1/T = 50$ for four other γ rays of Pr^{143}. As noted previously, the low intensity of all γ rays other than the 294-kev γ ray prevented the making of very accurate measurements. No meaningful results were obtained for the 232-, 351-, and 1100-kev γ rays because of this.

Table VI. Experimental $I(\theta)$ versus θ for Pr^{143} γ rays

Number of measurements	θ (degrees)	$I(\theta)$ 493 kev	668 kev	725 kev	861 kev
6	0	1.03±.05	1.07±.03	1.02±.03	1.14±.08
2	15	0.98±.05	1.05±.03	1.00±.03	1.07±.08
2	30	0.98±.05	1.04±.03	1.01±.03	1.08±.08
2	45	1.01±.05	1.04±.03	0.97±.03	1.28±.08
2	60	1.06±.05	0.98±.03	1.00±.03	1.13±.08
3	75	1.03±.05	0.98±.03	1.03±.03	1.11±.08
7	90	1.06±.05	0.99±.03	1.03±.03	0.99±.08

The limits of error in Table VI refer only to the results at $\theta = 0$ deg and $\theta = 90$ deg. The limits are based both on counting statistics and on the correction made for the background due to Compton scattering from higher-energy γ rays. The limits of error at other angles are larger than indicated, as fewer measurements were made at these angles, and thus the statistical counting errors were larger.

The results in Table VI show $I(0^{\circ}) > 1$ for both the 668-and the 861-kev γ rays. The results at $\theta = 90$ deg are consistent with this. Both these γ rays terminate at the 57-kev level, which was previously assigned a spin of 7/2. Therefore a $3/2 \xrightarrow{E2} 7/2$ or $11/2 \xrightarrow{E2} 7/2$ transition for either the 918- or 725-kev level of Pr^{143} is ruled out, as these give $I(0^{\circ}) < 1$. A spin of 1/2 for either of these levels is eliminated, as the experimental $I(0^{\circ}) \neq 0$. It can be concluded that the spins of the 918- and 725-kev levels, if the spin of the 57-kev level is 7/2, are 5/2, 7/2, or 9/2. This is reasonable in view of the first-forbidden beta transitions of Ce^{143} to each of these levels. The shell model is in good agreement with these assignments.

VII. CONCLUSIONS

On the basis of the foregoing experimental results, the following conclusions were reached:

(a) No attenuation effects were detected in the experimental results on the γ-ray anisotropy and plane polarization for the five cerium isotopes studied. These effects, due to fluctuations in the electromagnetic environment of the nucleus between the time of primary decay of the oriented nucleus and the time of emission of the observed γ ray, are generally most evident by a reduction of the experimental results from their theoretical value at lower temperatures. If present, these attenuation effects should have been most evident in the electron-capture decay of Ce^{139} to the relatively long-lived (1.5×10^{-9}-sec) 166-kev level of La^{139}. However, at temperatures down to $0.02^{\circ}K$, no such reductions were detected. Partially responsible for this is the fact that axial, as opposed to planar, nuclear alignment was utilized in these measurements.

(b) The magnetic moment obtained for Ce^{141} by the nuclear alignment method was found in agreement with that obtained by a previous paramagnetic resonance measurement. This agreement was a measure of the validity of the spin Hamiltonian used in interpreting the nuclear alignment results.

(c) In Ce^{141}, for which the first-forbidden beta transition is between two nuclear states with an identical spin, the $i_\beta = 0$ beta transition is favored over the $i_\beta = 1$ beta transition. Furthermore, the experimental results on Ce^{137} indicate that here also the $i_\beta = 0$ beta transition is favored over the $i_\beta = 1$ transition for a first-forbidden beta transition between two nuclear states of identical spin.

(d) In the two cases in which definite spin assignments were made ($I = 11/2$ for Ce^{137m} and $I = 5/2$ for the 142-kev level of Pr^{141}), the shell model was completely in agreement. In all other cases, the assignment of a most probable spin consistent with the shell model was in agreement with the nuclear alignment results.

(e) The E2/M1 mixing ratios found for the γ rays of Ce^{137}, Ce^{139}, and Ce^{141} were consistent with published conversion-electron, Coulomb excitation, and intermediate-level lifetime measurements.

(f) Theoretical calculations have been carried out for the magnetic dipole moments of nuclei on the basis of several models: the jj-coupling shell model[70], the individual-particle model,[71] the collective model,[72] the single-configuration model,[73] and the configuration-mixing model.[74] The configuration-mixing model of Noya, Arima, and Horie[74] was selected as the most appropriate for cerium nuclei. Using first-order perturbation theory and estimates of two-body interaction strengths determined from empirical data on pairing energies, these authors have calculated the departure of magnetic dipole moments from the Schmidt limit due to configuration mixing between $j = l + 1/2$ and $j_1 = l - 1/2$ orbitals. On the basis of this model, Noya et al. have calculated magnetic moments for about 100 near-closed-shell nuclei. Their calculated results generally agree with experimental magnetic moments to within 0.3 nm Table VII shows the agreement between the $|\mu_N|$ (exp) from the nuclear alignment results and the μ_N (calc) for both the Schmidt limit and the configuration-mixing model.

The proton configurations given in this table represent those protons outside the $Z = 50$ closed shell. The zeroth-order neutron configurations given for Ce^{137m}, Ce^{137}, and Ce^{139} represent those neutrons outside the $N = 50$ closed shell and outside the $1g_{7/2}$ closed subshell. The neutron configurations given for Ce^{139} and Ce^{141} represent those neutrons in the $1h_{11/2}$ subshell and those outside the $N = 82$ closed shell. The excitation mode of the neutron given in this table illustrates the configuration mixing between $j = l + 1/2$ and $j_1 = l - 1/2$ orbitals. The protons cannot be excited within the framework of this model because both the $1g_{9/2}$ and $1g_{7/2}$ subshells are filled. With the exception of Ce^{143}, only one mode of excitation is possible for the neutron configuration of each isotope. In Ce^{143}, two excitation modes are simultaneously possible: the $1h_{11/2} \longrightarrow 1h_{9/2}$ and

Table VII. Comparison between theoretical and experimental μ_N

Nucleus	Proton configuration	Neutron configuration (zeroth order)	Excitation mode of neutron	μ_N(calc)(nm) Schmidt limit	C=30 Mev	C=40 Mev	$\lvert\mu_N\rvert$ (expt) (nm)
Ce^{137m}	$(1g_{7/2})^8$	$(2d_{5/2})^6(2d_{3/2})^4(1h_{11/2})^{11}$	$(1h_{11/2})^{11} \longrightarrow (1h_{11/2})^{10}(1h_{9/2})^1$	-1.91	-1.14	-1.01	0.96 ± 0.09
Ce^{137m}	$(1g_{7/2})^8$	$(2d_{5/2})^6(2d_{3/2})^4(3s_{1/2})^2(1h_{11/2})^9$	$(1h_{11/2})^9 \longrightarrow (1h_{11/2})^8(1h_{9/2})^1$	-1.91	-1.29	-1.19	
Ce^{137}	$(1g_{7/2})^8$	$(2d_{5/2})^6(2d_{3/2})^3(1h_{11/2})^{12}$	$(1h_{11/2})^{12} \longrightarrow (1h_{11/2})^{11}(1h_{9/2})^1$	+1.15	+0.97	+0.94	0.95 ± .20
Ce^{137}	$(1g_{7/2})^8$	$(2d_{5/2})^6(2d_{3/2})^1(3s_{1/2})^2(1h_{11/2})^{12}$	$(2d_{5/2})^6(2d_{3/2})^1 \longrightarrow (2d_{5/2})^5(2d_{3/2})^2$	+1.15	+0.82	+0.78	
Ce^{139}	$(1g_{7/2})^8$	$(2d_{5/2})^6(2d_{3/2})^3(3s_{1/2})^2(1h_{11/2})^{12}$	$(1h_{11/2})^{12} \longrightarrow (1h_{11/2})^{11}(1h_{9/2})^1$	+1.15	+0.97	+0.94	0.95 ± .20
Ce^{141}	$(1g_{7/2})^8$	$(1h_{11/2})^{12}(2f_{7/2})^1$	$(1h_{11/2})^{12} \longrightarrow (1h_{11/2})^{11}(1h_{9/2})^1$	-1.91	-1.48	-1.41	1.30 ± .20
Ce^{143}	$(1g_{7/2})^8$	$(1h_{11/2})^{12}(2f_{7/2})^3$	$(1h_{11/2})^{12}(2f_{7/2})^3 \longrightarrow (1h_{11/2})^{11}(1h_{9/2})^1(2f_{7/2})^2(2f_{5/2})^1$	-1.91	-1.21	-1.10	1.00 ± .30
Ce^{143}	$(1g_{7/2})^8$	$(1h_{11/2})^{12}(1h_{9/2})^2(2f_{7/2})^1$	$(1h_{11/2})^{12}(1h_{9/2})^2 \longrightarrow (1h_{11/2})^{11}(1h_{9/2})^3$	-1.91	-1.58	-1.51	

$2f_{7/2} \longrightarrow 2f_{5/2}$ modes. The Schmidt limits, μ_N (calc), were calculated on the basis of the zeroth-order neutron configurations. The configuration-mixing model magnetic moments, μ_N (calc), were calculated on the basis of the excitation modes of the neutron for two value of C, where C is the ratio of an experimental neutron pairing energy to the product of (j + 1/2) times $A^{-1/2}$ times a harmonic oscillator radial integral, where A = Z + N. For nuclei between Z = 8 and Z = 84, C ranges from about 30 to 40 Mev.

A comparison between the experimental values of μ_N and the theoretical values gives an agreement to within 0.21 nm for C = 30 Mev and to within 0.11 for C = 40 Mev, if the first neutron configuration assigned to each nucleus is considered. The alternative neutron configurations given for Ce^{137m} and Ce^{143} may be excluded on the basis of this model as the resulting μ_N (calc) lies outside the experimental error of the nuclear alignment result. The alternative neutron configuration given for Ce^{137} gives a much poorer agreement with the experimental $|\mu_N|$ than the first neutron configuration. Consequently, on the basis of the configuration-mixing model, it appears that for Z = 58, the $3s_{1/2}$ subshell is not occupied until N = 81, and that three neutrons occupy the $2f_{7/2}$ subshell rather than having two neutrons paired in the $1h_{9/2}$ subshell. Finally, in each of these five cerium isotopes, the reduction of the magnetic moment from the Schmidt limit can be associated with the configuration mixing between $1h_{11/2}$ and $1h_{9/2}$ orbitals. The reduction is augmented in the case of Ce^{143} by configuration mixing between $2f_{7/2}$ and $2f_{5/2}$ orbitals.

ACKNOWLEDGMENTS

I wish to thank:

Professor David H. Templeton for his guidance as my research director and for his suggestions on the presentation of this thesis.

Professor David A. Shirley for his aid in carrying out and interpreting these experiments and for his responses to 99.44% of my questions.

Professor Glenn T. Seaborg for suggesting the field of nuclear orientation to me.

Professor John O. Rasmussen for his interest in my work and for his friendship.

Dr. Charles E. Johnson for introducing me to the techniques of nuclear orientation.

Dr. Brian R. Judd for his advice and clarification for me of crystal field theory.

Mr. Michiyuki Nakamura for his aptitude in explaining electronic systems to me and for his interest and assistance in designing the gamma-ray polarimeter.

Mrs. Mab I. Tocher for her aesthetic dediction to growing single crystals.

Mr. Gardner G. Young for his skill and ingenuity as a machinist.

Mr. Harry S. Powell for his achievements in the old-world art of glass-blowing.

Mr. Robert E. McCracken for his help in arranging neutron bombardments, and Mr. Deck Yoes, Mr. Homer Adams, and Mr. Ray Aune for their competence as health chemists.

Miss Carolyn Lovejoy and Mr. Quirino Navarro, Mr. Gene Westenbarger, Mr. Ron Grant, Mr. Dick Levy, and Mr. Jim Schooley, my associates, for their responses to 0.56% of my questions and for sharing with me the ups-and-downs of experimental work.

Dr. Jacques Valentin, and Dr. Morton Kaplan, Mr. Dick Chanda, Mr. Paul Reeder, Mr. Dave Whitney, Mr. Bruce Wilkins, Mr. Lee Hyder, Mr. Paul Croft, Mr. Ken Poggenburg, Mr. Ralph Korteling,

and Mr. John Olmsted for patiently explaining to me the solutions for the world's great problems.

Miss Claire J. Haley, my fiancée, for both inspiring me and for patiently awaiting the completion of this thesis.

The University of California for providing me with fellowships during the past four years.

This work was performed under the auspices of the U. S. Atomic Energy Commission.

REFERENCES

1. H. Noya, A. Arima, and H. Horie, Progr. Theoret. Phys. (Kyoto) 12, 623 (1955).
2. Amado Y. Cabezas, Electronic and Nuclear Properties of Some Radioactive Rare-Earth Elements (Thesis), Lawrence Radiation Laboratory, Report UCRL-9346, 1960.
3. R. W. Kedzie, M. Abraham, and C. D. Jeffries, Phys. Rev. 108, 54 (1957).
4. A. W. Overhauser, Phys. Rev. 92, 411 (1953).
5. A. Kastler, Proc. Phys. Soc. (London) A67, 853 (1954).
6. J. Brossel, B. Cagnac, and A. Kastler, J. Phys. Radium 15, 6 (1954).
7. F. Bloch, Phys. Rev. 93, 944 (1954).
8. C. D. Jeffries, Phys. Rev. 106, 164 (1957); 122, 1781 (1961).
9. N. Kurti, Phys. Today 2, 20 (1958).
10. N. Kurti and others in Proceedings of the Seventh International Conference in Low-Temperature Physics (University of Toronto Press, Toronto, 1961) p. 156.
11. R. J. Blin-Stoyle and M. A. Grace, Handbuch der Physik 42, 555 (1957).
12. W. J. Huiskamp and H. A. Tolhoek, Progr. in Low Temp. Phys. 3, 333 (1961).
13. M. Ferentz and N. Rosenzweig, Table of F Coefficients, Argonne National Laboratory Report ANL-5324 [1955].
14. R. M. Steffen, Advances in Phys. 4, 293 (1955).
15. H. Frauenfelder, in Beta- and Gamma-Ray Spectroscopy, K. Siegbahn, Ed. (Interscience, Publishers, Inc., New York, 1955) p. 531.
16. A. Simon, M. E. Rose, and J. M. Jauch, Phys. Rev. 84, 1155 (1951).
17. N. R. Steenburg, Phys. Rev. 95, 982 (1954).
18. E. Ambler, R. P. Hudson, and G. M. Temmer, Phys. Rev. 101, 196 (1956).

19. A. Abragam and M. H. L. Pryce, Proc. Roy. Soc. (London) A205, 135 (1951).
20. J. A. M. Cox and S. R. deGrott, Physica 19, 683 (1953).
21. J. M. Daniels, Can. J. Phys. 35, 1133 (1957).
22. C. A. Lovejoy and D. A. Shirley, in Proceedings of the Seventh International Conference on Low Temperature Physics (University of Toronto, Toronto, 1961) p. 164.
23. K. W. H. Stevens, Proc. Phys. Soc. (London) A65, 209 (1952).
24. R. J. Elliott and K. W. H. Stevens, Proc. Roy. Soc. (London) A215, 437 (1952); 218, 553 (1953); 219,387 (1953).
25. B. R. Judd and I. Lindgren, Phys. Rev. 122, 1802 (1961).
26. E. C. Ridley, Proc. Cambridge Phil. Soc. 56, 41 (1960).
27. B. Bleaney, Proc. Phys. Soc. (London) A68, 938 (1955).
28. C. F. M. Cacho, M. A. Grace, C. E. Johnson, A. C. Knipper, R. G. Scurlock, and R. T. Taylor, Phil. Mag. 46, 1287 (1955).
29. R. P. Hudson, Progr. in Cryogenics 3, 97 (1961).
30. H. Kopfermann, Nuclear Moments (Academic Press, Inc., New York, 1958) p. 398.
31. R. J. Blin-Stoyle and M. A. Grace, Handbuch der Physik 42, 608 (1957).
32. H. Meyer, Phil. Mag. 2, 521 (1957).
33. M. E. Rose, Phys. Rev. 91, 610 (1953).
34. L. W. Fagg and S. S. Hanna, Revs. Modern Phys. 31, 711 (1959).
35. F. Metzger and M. Deutsch, Phys. Rev. 78, 551 (1950).
36. O. Klein and Y. Nishina, Z. Physik 52, 853 (1929).
37. K. H. Spring, Photons and Electrons (John Wiley and Sons, Inc., New York, 1950).
38. G. R. Bishop and J. Perez y Jorba, Phys. Rev. 98, 89 (1955).
39. T. Schmidt, Z. Physik 106, 358 (1937).
40. R. A. Erickson, J. W. T. Dabbs, and L. D. Roberts, Rev. Sci. Instr. 25, 1178 (1954).

41. R. J. Omohundro, Rev. Sci. Instr. 29, 893 (1958).
42. R. E. Bell and H. E. Petch, Phys. Rev. 76, 1409 (1949).
43. R. E. Bell, in Beta- and Gamma-Ray Spectroscopy, K. Siegbahn, Ed. (Interscience Publishers, Inc., New York, 1955) p. 494.
44. William A. Wenzel, Millimicrosecond Coincidence Circuits for High-Speed Counting, University of California Radiation Laboratory UCRL-8000, Oct. 1957.
45. L. E. Glendenin, Anal. Chem. 27, 50 (1955).
46. F. G. Brickwedde, H. van Dijk, M. Durieux, J. R. Clement, and J. K. Logan, J. Research Nat'l. Bur. Standard 64A, 1 (1960).
47. D. Strominger, J. M. Hollander, and G. T. Seaborg, Revs. Modern Phys. 30, 585 (1958).
48. A. R. Brosi and B. H. Ketelle, Phys. Rev. 100, 169 (1955); 103, 917 (1956).
49. B. S. Dzhelepov, B. K. Preobrazhenskii, I. M. Ragachev, and P. A. Tishken, Bull. Acad. Sci. USSR 22, 923 (1958).
50. J. N. Haag, C. E. Johnson, D. A. Shirley, and D. H. Templeton, Phys. Rev. 121, 591 (1961).
51. S. A. Moszkowski, in Beta- and Gamma-Ray Spectroscopy, K. Siegbahn, Ed. (Interscience Publishers, Inc., New York, 1955) p. 373.
52. B. H. Ketelle, H. Thomas, and A. R. Brosi, Phys. Rev. 103, 190 (1956).
53. M. Goldhaber and A. W. Sunyan, in Beta- and Gamma-Ray Spectroscopy, K. Siegbahn, Ed. (Interscience Publishers, Inc., New York, 1955) p. 453.
54. J. E. Mack, Revs. Modern Phys., 22, 64 (1950).
55. T. R. Gerholm and H. deWaard, Physica 21, 601 (1955).
56. K. Kotajima and H. Morinaga, Nuclear Phys. 16, 231 (1960).
57. W. H. Kelly, G. B. Beard, W. B. Chaffee, and J. M. Gonser, Nuclear Phys. 19, 79 (1960).

58. K. Murakawa, Phys. Rev. 110, 393 (1958).

59. N. P. Heydenberg and G. M. Temmer, Phys. Rev. 100, 150 (1955).

60. M. A. Grace, C. E. Johnson, R. G. Scurlock, and R. T. Taylor, Phil. Mag., (to be published, 1961).

61. H. L. Polak, W. Schoo, B. L. Schram, R. K. Girgis, and R. van Lieshout, Nuclear Phys. 5, 271 (1958).

62. M. C. Joshi, B. N. Subba Rao, and B. V. Thosar, Nuovo cimento 9, 600 (1958).

63. H. deWaard and T. R. Gerholm, Physica 21, 599 (1955); Nuclear Phys. 1, 281 (1956).

64. J. R. Cook, Proc. Phys. Soc. (London) 77, 346 (1961).

65. L. A. Sliv and I. M. Band, University of Illinois Trans. Report 57ICCK1 Physics Dept. Urbana 1956).

66. S. H. Vegors, R. L. Heath, and W. Hammer, Graphs of the K-Conversion Coefficients as Calculated by Sliv and Band, Aug. 1959 (privately distributed).

67. B. R. Judd, quoted in E. Ambler, R. P. Hudson, and G. M. Temmer, Phys. Rev. 97, 1212 (1955).

68. D. W. Martin, M. K. Brice, J. M. Cork, and S. B. Burson, Phys. Rev. 101, 182 (1956).

69. H. Postma and W. J. Huiskamp, in Proceedings of the Seventh International Conference on Low Temperature Physics (University of Toronto, Toronto, 1961) p. 183.

70. M. G. Mayer and J. H. D. Jensen, Elementary Theory of Nuclear Shell Structure (John Wiley and Sons, Inc., New York, 1955).

71. B. H. Flowers, Proc. Roy. Soc. (London) A212, 248 (1952); with A. R. Edmonds, Proc. Roy. Soc. (London) A214, 515 (1952); 215A, 120 (1952).

72. A. Bohr and B. R. Mottelson, Kgl. Danske Videnskab. Selskab Mat.-fys. Medd. 27, No. 16 (1953).

73. H. Narumi and H. Nagai, Nuclear Phys. 16, 193 (1960).

74. H. Noya, A. Arima, and H. Horie, Progr. Theoret. Phys. (Kyoto) (Supplement) 8, 33 (1958).